Masteroppgave

NTNU
Norges teknisk-naturvitenskapelige universitet
Fakultet for ingeniørvitenskap

Elisa Solheim Høstmark

Experimental and numerical investigations on wave profiles and ventilation on a surface-piercing hydrofoil

Masteroppgave i Marin teknikk
Veileder: Luca Savio
Medveileder: Fengjian Jiang
Juni 2021

NTNU
Kunnskap for en bedre verden

Elisa Solheim Høstmark

Experimental and numerical investigations on wave profiles and ventilation on a surface-piercing hydrofoil

Masteroppgave i Marin teknikk
Veileder: Luca Savio
Medveileder: Fengjian Jiang
Juni 2021

Norges teknisk-naturvitenskapelige universitet
Fakultet for ingeniørvitenskap
Institutt for marin teknikk

NTNU
Kunnskap for en bedre verden

Experimental and Numerical Investigations of Wave profiles and Ventilation on a Surface-Piercing Hydrofoil

MASTER THESIS

Written By

Elisa Solheim Høstmark

&

Supervisor: Luca Savio

Co-supervisor: Fengjian Jiang

The Norwegian University of Science and Technology

NTNU | Department of Marine Technology

10.06.2021

NTNU | Department of Marine Technology

MASTER THESIS IN MARINE TECHNOLOGY
SPRING 2021

FOR

Elisa Solheim Høstmark

Experimental and Numerical Investigation of Wave Profiles and Ventilation on a Surface-Piercing Hydrofoil

The interest in free surface flows goes beyond their appearance in many practical applications. Associated with the interface between the two fluids many interesting flow conditions can be encountered. The wave pattern generated by a vertical foil that pierces the surface can suddenly result in breaking waves or in air to be drawn along the span, leading to multiphase flows. These flows are difficult to study both experimentally and numerically because of the strong non-linearity inherent to them.

The present thesis aims at providing high quality validation data for numerical investigation of free surface flows. Within the scope of the thesis two foils are tested experimentally. The first foil was designed to be used for studying free wave generation at a combination of Froude numbers and angles of attack. The second one was meant to be run to provide a test case for the inception of ventilation and its sensitivity to transients together with extension of ventilation. A selection of the conditions are to be tested numerically to draw conclusions on the accuracy of CFD in predicting wave profiles.

In the thesis the candidate shall present her personal contribution to the resolution of problem within the scope of the thesis work. Theories and conclusions shall be based on mathematical derivations and/or logic reasoning identifying the various steps in the deduction.

The thesis work shall be based on the current state of knowledge in the field of study. The current state of knowledge shall be established through a thorough literature study, the results of this study shall be written into the thesis. The candidate should utilize the existing possibilities for obtaining relevant literature.

The thesis should be organized in a rational manner to give a clear exposition of results, assessments, and conclusions. The text should be brief and to the point, with a clear language. Telegraphic language should be avoided.

The thesis shall contain the following elements: A text defining the scope, preface, list of contents, summary, main body of thesis, conclusions with recommendations for further work, list of symbols and acronyms, reference and (optional) appendices. All figures, tables and equations shall be numerated.

The original contribution of the candidate and material taken from other sources shall be clearly defined. Work from other sources shall be properly referenced using an acknowledged referencing system.

NTNU | Department of Marine Technology

The thesis shall be submitted electronically (pdf) in Inspera:

- Signed by the candidate
- The text defining the scope (this text) (signed by the supervisor included

Supervisor: Luca Savio

Co-Supervisor: Fengjian Jiang

Start: 15.01.2021

Deadline: 10.06.2021

Trondheim 02.06.2021

Luca Savio

Luca Savio (Jun 2, 2021 23:12 GMT+2)

Preface

This Master thesis was written during the spring of 2021, and it is the result of my final semester of a 5-year integrated study in Marine technology at the Norwegian University of Science and Technology (NTNU), in Trondheim. It was written in collaboration with Sintef and the experiments were conducted in the towing tank *Slepetanken* at the centre of Marine technology at Tyholt.

I would like to express my gratitude to my supervisor Luca Savio, for continuous guidance and support during the semester and for sharing ideas and giving feedback on my work. I am also very thankful for my co-supervisor Fengjian Jiang as well, for invaluable help with anything CFD-related and for always being ready to answer my questions. Although there were few opportunities to meet in person they have always been available for help and guidance and I have really appreciated working with them.

I would also like to thank Trond Innset and Ole Eirik Vinje for making the foils and to Terje Rosten for driving the towing rig and for helping out during the experiments and for being great company on the rig. Finally, a big thank you to my friends and family for supporting and encouraging me throughout my studies.

Trondheim, 10th of June, 2021

Elisa Solheim Høstmark

Abstract

A series of experiments were carried out on two separate surface-piercing hydrofoils in a towing tank with the Froude numbers and angles of attack as the main parameters. One blunt foil with a maximum thickness, t = 120 mm, which was used to observe the free wave generation and one slender, t = 40 mm, where ventilated flows where studied. An uncertainty analysis on the experimental results gave an uncertainty of e_X = 7.5% for the lift forces and e_X = 2.7% for the drag force. Additionally, a subset of the same conditions used on the blunt foil were simulated in the CFD software Fine/Marine. This was done to draw conclusions on the accuracy of CFD in predicting wave profiles.

Ventilated flows and its sensitivity to transients were studied by testing different methods of velocity development, either using a quasi steady state or a step wise acceleration. Yaw angles were adjusted both statically and dynamically. Its effect on the rigid forces, inception, washout and size of the cavitation are reported in this work.

The results of the step wise acceleration and the quasi steady state at low accelerations confirmed previous research conducted on the topic of ventilation in terms of flow behaviour. Increasing the acceleration had a noticeable effect on the results and inception occurred at much lower Froude numbers and washout at higher Froude numbers. Reversing the hysterectic effect that previously had been prominent. Testing with dynamically varying angles resulted in less consistent data. Higher Froude numbers and yaw angles were necessary for any kind of ventilation to develop and flow behaviour was less predictable when the same conditions were repeated.

The free wave generation were simulated numerically by recreating a sub set of the conditions used on the blunt foil. The simulations were capable of predicting the wave profiles with a fair accuracy, but it vastly underestimated the lift force. The issue was assumed to stem from the critical Reynolds regime that the foil were in. To solve it the simulations should be run again using a DES turbulence model instead of a the $k-\omega$ turbulence model. Due to a lack of time, this could not be achieved withing the scope of this thesis.

Sammendrag

En serie eksperimenter ble gjennomført på to separate overflate-brytende hydrofoiler med Froude tall og angrepsvinkler som hovedparametrene. En bred foil med maksimum tykkelse, t = 120mm, der bølgeprofilene ble undersøkt og en smal foil med maksimum tykkelse, t = 40mm, som ble brukt til å studere ventilasjon. En usikkerhetsanalyse ble gjennomført på de eksperimentelle resultatene, dette ga en usikkerhet på e_X = 7.5% for løftkreftene og e_x = 2.7% på dragkreftene. I tillegg ble et utvalgt sett av kondisjonene til den vide foilen simulert ved hjelp av numerisk fluiddynamikk i programmet Fine/Marine. På denne måten kunne det trekkes konklusjoner ved hvor presis numeriske metoder er til å estimere bølgeprofiler.

Ventilerte strømninger og deres sensitivitet i henhold til ulike parametere ble studert ved å teste ulike metoder for å utvikle foilens hastighet. Enten ved å bruke en kvasi - statisk hastighetstilstand, eller ved akselerere hastigheten stegvis. Foilens angrepsvinkel ble justert både statisk og dynamisk. Effekten som disse faktorene hadde på ventilasjonens oppstart, utvaskelse og kavitasjonsstørrelse er rapport i dette arbeidet.

Resultatene fra den stegvise akselereringen og den kvasi-statiske tilstande ved lave akselerasjoner bekreftet tidligere undersøkelser gjennomført innenfor feltet når det gjelder strømningsoppførsel. Å øke akselerasjonen hadde en merkbar effekt på resultatene og oppstart av ventilasjon skjedde på mye lavere Froude tall, mens utvaskelse skjedde på høyere Froude tall. En reversering av de tidligere prominente hysterektiske effektene. Testene som inkluderte dynamiske vinkler, ga mindre konsekvente resultater og høyere Froude tall og angrepsvinkler var nødvendig for at ventilasjon skulle kunne utvikle seg.

Den frie bølgedannelsen ble numerisk simulert ved å gjenskape et utvalg av de samme kondisjonene som ble brukt på den vide foilen. Simuleringene var i stand til å estimere vannlinjen rundt foilen med ganske god nøyaktighet, men den undervurdert sterkt løftkreftene. Problemet er antatt å stamme fra det kritiske Reynoldsregimet som foilen befant seg i, noe som førte til at simuleringene ikke klarte å forutsi strømningene og da spesielt separasjonspunktet korrekt. For å løse dette problemet burde simuleringene bli repetert med en DES turbulensmodell i stedet for en $k-\omega$ turbulensmodell. Grunnet tidsbegrensinger kunne ikke dette oppnås innen rammeverket til denne masteroppgaven.

Nomenclature

Abbreviations

CAD Computer aided design

CFD Computational fluid dynamics

DDES Delayed Detached Eddy-Simulation

DES Detached Eddy-Simulation

DNS Direct numerical simulation

FV Fully ventilated

FVM Finite volume method

FW Fully wetted

IDDES Improved Delayed Detached Eddy-Simulation

LES Large scale eddy simulation

PV Partially ventilated

RANS Reynolds Averaged Navier Stokes

VOF Volume of fluid

Greek Letters

α Angle of attack (yaw angle)

α_b Bifurcation angle

α_E Waterline entrance angle

α_E^B Critical waterline entrance angle

$\Delta\sigma$ Cavitation number

γ Surface tension

κ Length from free surface to L_c

μ Viscosity

ν Kinematic viscosity

ν_t Kinematic eddy viscosity

ω Turbulent dissipation

Φ Angle of cavitational closure line

ρ Fluid density

ζ Wave elevation

Roman Letters

$\bar{e_x}$ Uncertainty of the mean

$\bar{P_x}$ Mean precision limit

$\bar{S_x}$ Mean standard deviation

$\bar{X}$ Mean value

A Wave amplitude

a acceleration

AR Aspect ratio

ARh Immersed aspect ratio

B Fractional function for tracking free surface interface

C Courant number

c Chord length

C_R Residual resistance coefficient

C_T Total resistance coefficient

C_v Viscous resistance coefficient

C_w Wave resistance coefficient

C_D Drag coefficient

C_{L_w} Critical lift coefficient for stable ventilation

C_L Lift coefficient

C_M Moment coefficient

D Two dimensional drag force

$D_{unsteady}$ Unsteady drag component

e Energy

e_x Uncertainty of a single measurement

e_{rel} Relative error

F_{nh} Immersed Froude number

F_n Froude number

F_{Tot} Total force

F_X Force in x-direction (Drag)

F_Y Force in y-direction (Lift)

g Gravitational acceleration

H	Cavitational depth
h	Immersed Depth of foil
k	Turbulent kinetic energy
L	Two dimensional lift force
l	Characteristic length
L_c	Cavity length
l_m	Model length
l_s	Full size length
L_x, L_y, L_z	Domain length in x-, y- and z-direction
$L_{unsteady}$	Unsteady lift component
M	Yaw moment
m_{ij}	Added mass tensor
Ma	Mach Number
N	Number of samples
p	Pressure
P_x	Precision limit
p_∞	Absolute free-stream pressure
p_{atm}	Atmospheric pressure
p_c	Pressure within the cavity closure
R	Ratio
R_w	Wave resistance
Rn	Reynolds number
s	Span
S_x	Standard deviation
t	Thickness
t_s	Estimation weight using student's t-distribution
t_c	Chauvenets criteria for rejecting outliers
u, v, w	Velocity components in x-, y-, and z-direction
V	Velocity
We	Webers number
Y_B	Width of bounding box
z‘	Depth of cross sectionl

Contents

List of Tables

List of Figures

Chapter 1

Introduction

The free surface flows generated by a vertical foil in a fluid can lead to interesting flow phenomenons related to the interface between air and water. For a blunt foil, breaking waves can be generated from the leading edge. A flow separation can lead to air getting drawn down to the suction side of the foil, leading to a multi-phase flow. These are both complex flow behaviours associated with inherent non-linearities, making them difficult to study both experimentally and numerically. In this thesis the surface-piercing foil was chosen as the subject, as it provides a simple and general case which can be transferred to other applications. Examples of such application are rudders, which are often prone to ventilation or to look at the wave generation on a ship.

Lifting devices operating near or at the free surface are at risk of drawing in air from the free surface and developing multi-phase flows. The consequences of this can be a dramatic loss of lift force, as well as loss in efficiency, speed, maneuverability and stability. This thesis looks to understand how transients affects the ventilated flow, particularly in terms of inception, washout and size.

For many vessels, the wave resistance makes up an important component of the total resistance. The wave profiles generated by a surface-piercing hydrofoil functions as a proxy for its generated wave resistance. Accurately predicting the resistance due to wave generation is therefore an important tool in reducing the over all resistance and to improve the fuel efficiency of ships.

Computational fluid dynamics have over the last few years become widely adopted within the marine industry, and although it has been successfully validated for a broad variety of flow aspects, the wave elevation along the hull is one of the lesser validated flow features related to ship hydrodynamics. Ventilated flows have even less validation in numerical predictions due to the complex physical process related to it. Although it was not possible to include within the scope of this work, it can hopefully provide a base for further work on the topic.

Within the scope of this thesis two foils were tested experimentally using the immersed Froude number and angle of attack as the main parameters. Additionally the effect of acceleration and yaw movements were investigated. The first foil was made with the intention of studying free surface wave profiles, and was designed for larger wave generation. The second foil was designed to be more susceptible to the inception of ventilation, such that its sensitivity to transients in relation to the multi-phase flows could be tested. A selection of the conditions tested on the first foil are to be simulated numerically, to draw conclusions on the accuracy of CFD in predicting free wave generation.

1.1 Background

Experimental studies on the subject of ventilation was studied extensively during the mid-to late 20th century. Two types of ventilation was identified by Wetzel (1957), by performing experiments on vertically placed rods. These were named creeping and flash ventilation. It

was also determined that the type of ventilation depended on the Froude number and yaw angle. The flash ventilation was determined to occur suddenly at yaw angles above the stall angle and resulted in a hysterectic effect on the flow. Creeping ventilation on the other hand, developed gradually at low angles. Breslin and Skalak (1959) performed a series experiments on surface-piercing hydrofoils of various cross-sections, a drastic reduction in lift, as well as a smaller reduction in drag was reported during ventilated flow. The terms inception and closure were used for the generation and disappearance of ventilation. Two Froude based criteria for a stable ventilated flow were cited as $C_{L,w} \geq 5Fn_h^{-2}$ and $Fn_h \geq 3$. Rothblum et al. (1969) experimented on submerged hydrofoils and observed the same two types of ventilations as Breslin and Skalak (1959). They also found that hysteresis caused the ventilated flow to persist down to, and even beyond a zero-degree angle of attack. Swales et al. (1974) reported that two requirements must be fulfilled for ventilation to be sustained: (1) Pressure below atmospheric pressure at the suction side of the foil. (2) Flow separation around the foil.

More recent studies on multi-phase flows has broadened the understanding of the underlying physics and has also begun to include numerical investigations. Young and Brizzolara (2013) conducted experimental tests on a surface-piercing hydrofoil, which were combined with numerical modelling using a 3D boundary element method. Here, the major flow regimes that defined the flow around the foil were identified and referred to as fully attached, transitional or fully ventilated, depending on the separation and amount of aeration present on the suction side. Harwood et al. (2014) and Harwood et al. (2016) developed further on the flow regimes and defined criteria for each flow based on the depth of the ventilated cavity and angle of the cavity closure. Here, the generation of ventilation was referred to as inception and the closure as wash-out. A mapping of the flow regimes as a function of yaw angle and depth based Froude number, which included transition flows, or bi-stable flows was plotted. A review of the scaling relations on ventilated bodies related to the hydrodynamic and hydroelastic response were presented by Young et al. (2017).

Numerically predicting ventilation is a complex issue and the transitions between flows can be particularly challenging. Charlou et al. (2020), used a RANS solver to achieve perturbation-induced ventilation. They achieved good results for simulations at high yaw angles, but it was difficult to predict correct behaviour in bi-stable regimes. Andrun et al. (2020) performed similar RANS simulation on various Froude numbers and obtained good results for the predicted lift, drag forces on the other hand were overestimated.

For investigating the wave profiles formed along the hydrofoil, the intent was to use a method for detecting and reconstructing waterlines along a hull, using computer vision technique, as presented by Nataletti et al. (2019). Unfortunately, due to the high Froude numbers used during the numerical simulation and the poor contrast between the fluid surface and solid surface of the hull, it could not be achieved within the time limitations.

Two articles by Noblesse et al. (2008) and Noblesse et al. (2013) presented a simple criteria based on the Froude number and waterline entrance angle for predicting when a hull would generate a breaking or non-breaking bow wave. This criterion was used in the design of the blunt foil, and in the observations of the wave generation.

1.2 Objectives

The objectives of this thesis can be divided into two main goals: first, to investigate ventilated flows on a surface-piercing hydrofoil and how varying specific parameters would affect the flow

around the foil. Second, to compare numerically simulated wave profiles to the ones documented during the experiments. The objectives can be further divided into the following points:

- Conduct experiments in the towing tank to investigate wave profiles and ventilated flows on two separate foils. Foil 1 is used to measure wave profiles, while foil 2 is used to induce ventilated flows. Measure rigid forces in x- and y-direction and the wave elevation for both foils.
- Analyse the data obtained from the experiments to investigate the free surface behaviour and the effects of different parameters on the behaviour of the flow.
- Simulate a sub set of the same conditions used in the experiments on foil 1 using the CFD software Fine/Marine.
- Compare numerical models to results from the experiments conducted on foil 1 to draw conclusions on the accuracy the results obtained from CFD.

1.3 Approach

The theory and literature study, as well as the planning process of the foil design, was based on the project thesis written by the author during the autumn of 2020. A series of experiments were then carried out in a towing tank on two hydrofoils in early February. The data collected from these experiments were analysed and visualized in Matlab, ShipY and Excel. The plots were generated in Matlab. All figures were created in Inkscape, while the CAD drawings of the foil were made in Rhinocerus. Videography from the high speed cameras were visualized in PFV4, and the underwater cameras in VLC media player. The numerical simulations were modelled in Fine/Marine, by using the two-equation RANS solver $k-\omega$ (SST) turbulence model.

1.4 Limitations

The limitations of the thesis were as follows:

- Time spent in the towing tank conducting experiments
- A maximum force on the towing rig, set limitations conditions using both high angles and high velocities simultaneously.
- The numerical simulations were time consuming and only a limited amount of simulations were possible to run within the time limitations.
- Only a qualitative comparison of the waterline could be done due to a poor videography at the simulated Froude number and insufficient time
- Limited vision, only one angle visible from the camera perspective. The waterline was not completely visible at all runs and only one of the foils side could be visualized during the run.

1.5 Recommendations for Future Work

For future work, the following topics are recommended for further investigation:

- Simulate the conditions of the foil using a direct solution, or a combination direct and RANS solution, for better predictions of flow separation and force estimations, the detached eddy-simulation model is recommended.

- Extend the simulations to include the second, slender foil to provide quality data on numerical ventilation predictions.
- Compare experimental and numerical waterlines using a computer vision technique, this can be achieved more easily by running the simulations at lower Froude numbers.
- More extensive testing of the influence of dynamically changing angles on the ventilated flows.

1.6 Structure

The structure of the thesis involves a presentation of relevant theory in chapter 2 - 4, where theory related to foil, resistance and CFD are presented. A literature study in chapter 5-7, looks into previous research conducted on the subject of the thesis. Afterwards in chapter 8 -9 a description of the method used for the numerical and experimental work conducted, then the results of this work is presented, discussed and concluded in chapter 11 - 12 The structure of the chapters is as follows:

1. Theory
    - Chapter 2 - Foil theory
    - Chapter 3 - Ship Resistance
    - Chapter 4 - Computational Fluid Dynamics
2. Literature study
    - Chapter 5 - Characteristics of the Bow Wave
    - Chapter 6 - Waterline Measurements
    - Chapter 7 - Ventilation
3. Method
    - Chapter 8 - Experimental Method
    - Chapter 9 - Uncertainty analysis
    - Chapter 10 - Numerical Set up
4. Results and concluding chapters
    - Chapter 11 - Results and discussion
    - Chapter 12 - Conclusion and further work

Chapter 2

Foil theory

This chapter describes foil theory, focusing on the physical aspects as well as theory relevant to the work in this thesis.

A foil is defined as a body generating a lifting force perpendicular to the surrounding fluid flow. When said fluid is water, the term hydrofoil is used. The lift is caused by the pressure distribution around the foil, as the changes in velocity creates one high-pressure and one low pressure side. Three characteristics influences the lift: camber, thickness and angle of attack.

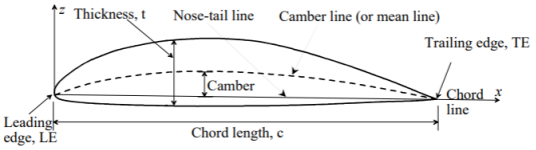

Figure 2.1: The geometry of a 2D foil defined. Reprinted from Steen and Minsaas (2014, p. 23)

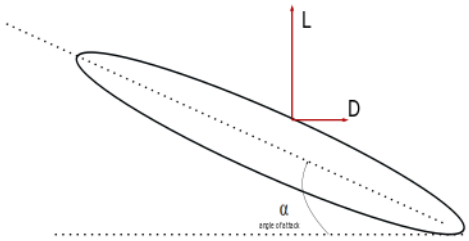

Figure 2.2: 2D foil with angle of attack

The two-dimensional hydrodynamic forces, lift (L) and drag (D), can be made non-dimensional using the force components C_L and C_D (Cengel & Cimbala, 2010).:

$$C_{L_{2D}} = \frac{L}{0.5\rho V^2 c} \tag{2.0.1a}$$

$$C_{D_{2D}} = \frac{D}{0.5\rho V^2 c} \tag{2.0.1b}$$

2.1 Linear foil theory

Linear foil theory is a simplified way of modelling the flows around a foil and is based upon three assumptions (Faltinsen, 2005):

- Maximum thickness is much smaller than chord length ($t << c$)

- Camber is much smaller than chord length ($z_{max} << c$)
- Angle of attack is small ($\alpha \lesssim 10°$)

Using these assumptions, the flow around the foil can be modelled by considering the lifting components separately and superimposing them. Hence, the flow around the foil can be solved using the following equation, where the lifting problem includes both the effect of camber and angle of attack.

Lifting problem + Thickness problem

Note that the theory is limited as it assumes a linear relation between lift and angle and that the boundary layers are thin. Flow separation is therefore not accounted for either.

Effect of thickness and camber The lift generated by the angle of attack comes from an induced velocity (w_i). The incoming velocity (V) is forced to change direction as it passes the foil and this creates the new velocity component. The relation between the incoming velocity, induced velocity and angle of attack is shown in figure 2.3. This gives the following expression for the non-dimensional lift coefficient (Faltinsen, 2005):

$$C_{L_\alpha} = 2\pi\alpha \tag{2.1.1}$$

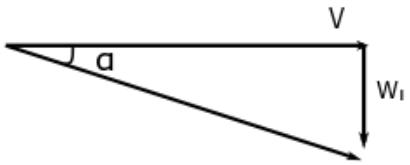

Figure 2.3: V, w_i, α relation

The total lift coefficient (C_L) is the sum of the effect of camber and the attack angle. The zero lift angle (α_0), defines the point where the foil lifts purely by camber. This gives the following equations: (Steen & Minsaas, 2014)

$$C_{L_{2D}} = C_{L_{camber}} + C_{L_\alpha} \tag{2.1.2}$$

$$C_{L_{2D}} = 2\pi(\alpha - \alpha_0) \tag{2.1.3}$$

Thickness effect Generally, a foil might need a certain thickness for two reasons: (1) strength and stiffness, or (2) to avoid flow separation at the leading edge. A sharper leading edge induces flow separation at lower velocities and angles. Such a separation may place the foil in risk of developing ventilation. On the other hand, a blunt leading edge can cause an increase in the drag force and an increased chance of cavitation. (Steen & Minsaas, 2014)

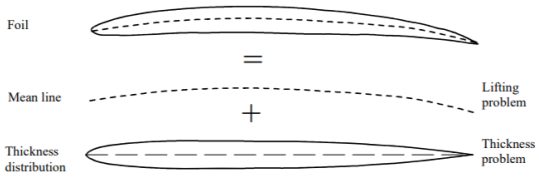

Figure 2.4: .
The lifting problem on a foil. Reprinted from (Steen & Minsaas, 2014, p. 51)

As mentioned previously, the thickness effect can be viewed separately and then be superimposed on the lifting problem. This only applies as long as the thickness is small compared to the chord length ($t << c$), but it does makes the modelling of the flow easier. Sarraf et al. (2010) showed that the lift force on a foil would increase with the thickness until it reached approximately 10% of the chord length, after this the lift coefficient would start to decrease. Hence, the thickness requirement for linear theory. It was also noted that a thicker foil would lead to greater oscillation amplitudes of the separation point and increase the noise and vibrations on the foil.

2.2 Lift distribution on three-dimensional foils

Prandtl's lifting line theory can be used to predict the lift distribution on a span-wise expanded foil, based on the geometry. The theory states that the lift distribution is proportional to the circulation distribution, as illustrated in figure 2.5, By using the lifting line theory and assuming an elliptical circulation distribution can be approximated by the following equations (Faltinsen, 2005):

$$C_{L,3D} = \frac{C_{L_{2D}}}{1 + \frac{2}{AR}} \tag{2.2.1a}$$

$$C_{D,3D} = \frac{C_L^2}{\pi AR} \tag{2.2.1b}$$

Where $AR = s/c$ is the aspect ratio, is the total span of the foil, for a surface piercing hydrofoil this gives $AR = h/c$.

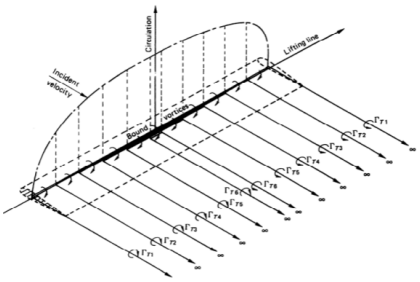

Figure 2.5: Three dimensional circulation distribution on a foil using lifting line method. Reprinted from Steen and Minsaas (2014, p. 69)

Chapter 3

Ship resistance

In this section, the theory behind ship resistance is looked into, with a heavier focus on wave resistance for both breaking and non-breaking waves. Although this section refers to ships and the resistance on ship hulls, the same theory can be applied to a surface-piercing hydrofoil. This can be done as the geometry is closely related and the governing physics are equivalent. The resistance components are also the same, with a few exceptions which are not present on a hydrofoil, such as the appendage resistance.

The resistance on a hull can be divided into two main components: frictional resistance, which is caused by the viscous effect on the ship, and the residual resistance. Residual resistance includes all remaining components, where amongst these, the pressure resistance is the most dominating. The pressure resistance mostly derives from wave generation, but it also includes a pressure resistance generated by viscous effects in the flow. The frictional component works as a tangential shear force on the surface, while the pressure works normal to the surface, as can be seen in figure 3.1. (Molland et al., 2011). The components can then be further divided as:

Figure 3.1: Directions of the frictional and pressure forces. (Molland et al., 2011, p. 13)

- Frictional resistance
- Viscous resistance
- Hull roughness resistance
- Transom stern resistance
- Wave resistance
- Wave breaking resistance
- Air resistance

3.1 Wave resistance

Wave resistance is caused by the wave pattern generated by a vessel moving straight ahead in constant speed in calm water conditions (Faltinsen, 2005). As the waves are generated, energy is transferred away from the vessel and creates a resistance force. The waves themselves develops from the change of volume along the hull. When the fullness of the hull increases, the flow will be forced out towards the sides and when the fullness decreases towards the aft body the flow will move back towards the center line. The change in flow will result in a change of the pressure and velocity distribution which can be explained by the Bernoulli equation (Cengel & Cimbala, 2010):

$$\frac{1}{2}\rho V^2 + \rho g\zeta + p = constant \tag{3.1.1}$$

Where V is the fluid velocity at the free surface, p is the pressure, ρ the fluid density, g = $9.81 m/s^2$, the gravitational acceleration and ζ is the wave elevation. The pressure distribution is limited by the atmospheric pressure at the free surface. Therefore, the pressure distribution will also cause a change of wave elevation around the hull, with wave peaks in areas where the pressure is high and troughs in low pressure areas. The waves generated by the body can further be divided into two different types, (1) The inner wave system or Bernoulli waves, these are caused by local disturbances and will decrease rapidly as they move away from the ship. They are not oscillating and are a direct result of the pressure-velocity distribution. (2) The Kelvin wave system are oscillatory waves that forms behind the ships rear and consists of transverse and diverging waves (see fig. 3.3).

The waves generated by the pressure/velocity distribution can be divided into four different wave systems that interferes and creates a resulting wave system (Molland et al., 2011). The wave system are visualised in figure 3.2. The systems are as following:

- Bow wave
- Forward shoulder wave
- After shoulder wave
- Stern wave

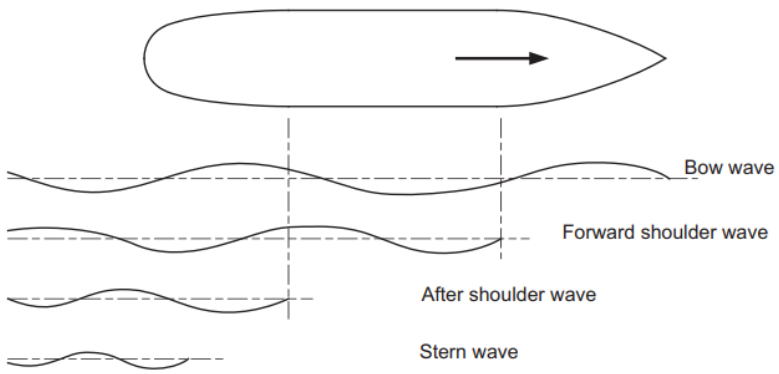

Figure 3.2: The wave systems generated by a ship (Molland et al., 2011, p. 30)

For ships with smooth shoulders, the shoulder waves will not affect the wave resistance to any large extent, leaving the stern and bow wave to have the most impact. The wave systems interfere with each other, which can be both favorable and unfavorable for the resistance. The bow wave system is usually the most dominating wave system, while the stern wave will have a lesser effect on the resistance (Molland et al., 2011). Meaning that in most cases, the shape of the bow will have a much larger impact on the resistance than the stern.

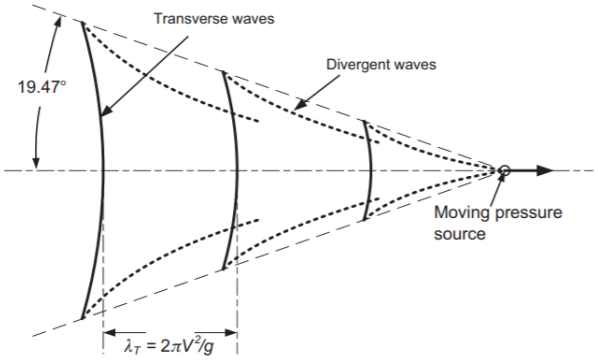

Figure 3.3: The Kelvin wave system. Reprinted from Molland et al. (2011, p.30)

Wave resistance can be further divided into breaking and non-breaking wave resistance. The breaking resistance is caused by high local pressure in front of a blunt bow. The blunt bow then generates wave breaking. (Faltinsen, 2005) Wave breaking causes energy loss and increased resistance. Usually, this makes up a very small portion of the total resistance, but for non-slender ships, it can be significant.

3.2 Resistance prediction

There are three main methods of resistance prediction on a vessel (Molland et al., 2011). They can be used individually or as a combination of two or all. The methods are the following:

- Empirical
- Model testing
- Numerical solutions

Empirical methods bases the residual resistance coefficient (C_R) on data from similar vessels. Numerical calculations are used to determine the resistance components by using CFD or potential methods. Experimental methods are mostly performed in a towing tank where a model is towed with a rudder, but no propeller. (Molland et al., 2011)

For scaling purposes three kinds of similarities must be present on the model during experimental testings:

1. *Geometric similarity*: the geometry must be equivalent and the ratio between the dimensions must be the same in model and full size.
2. *Kinematic similarity*: the relation between the velocities in full scale and model scale must be the same.

3. *Dynamic similarity*: there must be similarity in the force ratios.

The dynamic similarity can be expressed in a multitude of ways, for the different forces that affect the vessel in question. The most relevant dynamic scaling ratios are the Reynolds number, R_n, the Froude number, F_n. Where the Reynolds number gives the ratio of inertia and viscous forces, and thereby indicates how laminar or turbulent the flow is. The Froude number gives the ratio between inertia forces and gravitational forces. The relation is given in equation 3.2.1 and 3.2.2. Some other relevant scaling factors are the Mach number, Ma, and the Weber number, We. The Weber number expresses the ratio of inertia over surface tension, and the Mach number is the ratio between inertia and elasticity. (Cengel & Cimbala, 2010)

$$Rn = \frac{Vl}{\nu} \tag{3.2.1}$$

$$Fn = \frac{V}{\sqrt{gl}} \tag{3.2.2}$$

Where l is the characteristic length and ν is the kinematic viscosity. As using both Reynolds scaling and Froude scaling is not feasible unless $l_s/l_m = 1$, where l_s and l_m is the characteristic length in full size and model size, respectively. Which only occurs in full scale. Choosing scaling method, therefore depends on what the objective of the experiments are.

According to Froude‘s method, the total resistance of a vessel can be divided into to main components: viscous resistance and residuary resistance. Where the latter mainly consists of wave resistance and wave breaking resistance (Molland et al., 2011). This divides the total resistance in two components: The Reynolds dependent part, which includes the viscous resistance. The Froude dependent resistance, which pertains the wave resistance. By using this assumption the following resistance sum is given:

$$C_T(Rn, Fn) = C_v(Rn) + C_R(Fn) \tag{3.2.3}$$

For the non dimensional coefficients for total resistance (C_T), viscous resistance (C_v) and residuary resistance (C_R), respectively.

The wave resistance is considered Froude dependent as the free surface flows are dominated by gravitational forces. When conducting experiments where free surface effects are the main focus, using Froude scaling is therefore typically used as it ensures correct scaling of wave resistance. (Steen, 2014) The Reynolds number should still be taken into consideration and kept sufficiently high to have similar flow conditions in terms on turbulent or laminar flow.

Chapter 4

Computational fluid dynamics

Computational fluid dynamics (CFD) is widely used in the engineering and research industry in areas such as aerodynamics, fluid dynamics, weather simulations and much more. It uses discretization to numerically analyse fluid flow problems and is capable of solving complex and large scale simulations. The objective of this chapter is to provide an overview of the theory behind CFD, and to give a brief description of how it can be used for areas such as turbulence modelling and free surface modelling. A larger focus has been put on theories and methods used by Fine/Marine for the numerical simulations in this thesis. Additionally, an introduction to the CFD software Fine/Marine is given.

4.1 Governing equations

The fundamentals of CFD are the governing equations that conserves the physical laws of the fluid. Collectively, these equations are referred to as the Navier Stokes equations. The physical principles that the equations are based upon are the following (Wendt et al., 2009):

1. Conservation of mass
2. Conservation of momentum
3. Conservation of energy

For hydrodynamic cases at low Mach numbers, it is reasonable to assume that the flow is incompressible. An unsteady, three-dimensional, incompressible flow gives the two relevant governing equations (Tannehill et al., 1997):

The continuity equation:

$$\nabla \cdot V = 0 \tag{4.1.1}$$

The momentum equations:

x-component:

$$\rho \frac{Du}{Dt} = \frac{\delta p}{\delta x} + \mu \nabla^2 u + \rho f_x \tag{4.1.2}$$

y-component:

$$\rho \frac{Dv}{Dt} = \frac{\delta p}{\delta y} + \mu \nabla^2 v + \rho f_y \tag{4.1.3}$$

z-component:

$$\rho \frac{Dw}{Dt} = \frac{\delta p}{\delta z} + \mu \nabla^2 w + \rho f_z \tag{4.1.4}$$

Where $\nabla = (\frac{\delta}{\delta x}, \frac{\delta}{\delta y}, \frac{\delta}{\delta z})$ and the velocity, V = (u,v,w), which are the velocity components in x,y,z - direction. The substantial derivative $\frac{D()}{Dt} = \frac{\delta()}{\delta t} + V \cdot \nabla()$. The component ρf_i is the body force

per unit, which in z-direction equals the gravitational force.

4.2 Mesh generation

As mentioned previously, CFD uses discretization to solve fluid problems. For this, a good grid generation is vital. In general, there are two ways of creating a grid:

1. unstructured grid
2. structured grid

The difference can be seen in figure 4.1. A structured approach is the simplest form of discretization and is very convenient as it gives efficient and discrete solutions. However, it lacks flexibility and cannot be integrated into complex geometries. It also does not allow for finer grids and nodes in certain areas which might be of greater interest. Unstructured grids on the other hand, can be adapted to any geometry, but they are also less efficient than their counterpart (Voller, 2009). A variety of shapes can be used for unstructured grids, such as hexahedrals or tetrahedrals and it is a common method for any automatic meshing systems in a CFD software.

One of the most common approaches to discretization is to use the *finite volume method* (FVM), which solves the partial differential governing equations as algebraic equations. FVM balances fluxes by controlling the volumes (Kolditz, 2002), it can be applied to both structured and unstructured meshes and is therefore well suited to a variety of geometries.

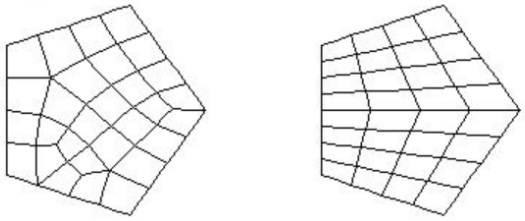

Figure 4.1: Unstructured vs. Structured grid generation

4.3 Turbulence modelling

The Navier Stokes equations are capable of solving any flow problem, however, it can quickly become very complicated, time consuming and expensive. This especially applies to the simulation of turbulent flows. A turbulent regime is defined by eddies, swirls, flow instabilities and diffusivity, and it is highly irregular in both space and time. It is chaotic and complicated in nature and the many length scales that are needed to analyze the flow - from the smallest fluctuations to large scale eddies - makes it very demanding to solve. (Tennekes & Lumley, 1972). Turbulence models are therefore used as a way of simplifying and approximating this issue, such that the flow problems can be solved without a massive resource requirement.

Turbulence arrives when the Reynolds number is high and will almost always be present in full scale hydrodynamic cases. To solve the issue of turbulence, several methods have been developed; the flow can be solved directly through DNS (Direct Numerical Simulation) or LES (Large Eddy Simulation). However these are only capable of dealing with simple problems as the computational effort and cost increases rapidly. (Tannehill et al., 1997)

Reynolds Averaged Navier-Stokes equations (RANS) is a mathematical model widely adopted in the engineering industry. It is a time-averaged version of the Navier Stokes equation and solves the turbulence problem by decomposing the velocity and pressure components of Navier Stokes into two parts, one mean and one fluctuating part. Such that the x-component, as an example, can be formulated as following, where $\overline{u}$ is the mean part and $u‘$ is the fluctuating part (Wendt et al., 2009).

$$u = \overline{u} + u‘ \tag{4.3.1}$$

By applying this decompostition to the governing equations, they can be rewritten as:

Incompressible continuity equation:

$$\frac{\delta \overline{u}_j}{\delta x_j} = 0 \tag{4.3.2}$$

Incompressible momentum equation:

$$\frac{\delta}{\delta t}(\rho \overline{u}_j) + \frac{\delta}{\delta x_j}(\rho \overline{u}_i \overline{u}_j) = -\frac{\delta \overline{p}}{\delta x_i} + \frac{\delta}{\delta x_j}(\overline{\tau}_{ij} + \rho \overline{u_i‘ u_j‘}) \tag{4.3.3}$$

Where $\overline{\tau}_{ij}$ is the viscous stress component and the term $\overline{u_i‘ u_j‘}$ is known as the Reynolds stress.

$$\overline{\tau}_{ij} = \mu(\frac{\delta \overline{u}_i}{\delta x_j} + \frac{\overline{u}_j}{\delta x_i}) \tag{4.3.4}$$

There are various RANS based turbulence models, which can be categorized as following (Rodriguez, 2019):

- Algebraic or zero-equation models
- One-equation models
- Two-equation models
- Reynolds stress transport models

K-ω SST Turbulence model The $k-\omega$ (SST) model was first presented by Menter (1994) as a two-equation RANS turbulence model that combines two other models: the $k-\omega$ model and the $k-\epsilon$ model. The first model functions best in the inner parts of the boundary layer, while the latter performs better in free shear flows. By using a blending function (F_1), the model is able to switch from from $k-\omega$ behaviour to $k-\epsilon$ as it enters free stream the model is capable of better capturing the turbulent flow problems. The equations presented by Menter (1994) were the following:

Turbulent Kinetic Energy:

$$\frac{Dk}{Dt} = \tau_{ij}\frac{1}{\rho}\frac{\delta(u_i)}{\delta x_j} - \beta^* \omega k + \frac{\delta}{\delta x_j}[(\nu + \sigma_k \nu_t)\frac{\delta k}{\delta x_j}] \tag{4.3.5}$$

Specific Dissipation Rate:

$$\frac{D\omega}{Dt} = \frac{\gamma}{\rho\nu_t}\tau_{ij}\frac{\delta(u_i)}{\delta x_j} - \beta_i\omega^2 + \frac{\delta}{\delta x_j}[(\nu + \sigma_\omega\nu_t)\frac{\delta\omega}{\delta x_j}] + 2(1 - F_1)\frac{\sigma_{\omega 2}}{\omega}\frac{\delta k}{\delta x_j}\frac{\delta\omega}{\delta x_j} \tag{4.3.6}$$

Where ω is the dissipation k is the turbulent kinetic energy, β^*, σ_ω, γ, β_i are constants. ν and ν_t are the kinematic viscosity and kinematic eddy viscosity.

Detached Eddy Simulation RANS modelling is usually sufficient for most hydrodynamic analyses, there are however some areas where problems can arise. For instance, the $k-\omega$ model usually gives satisfactory results in near-wall regions, but can struggle in cases of pressure induced-separation flows. Hybrid solutions, such as the detached eddy simulations (DES), may then be necessary. DES are modificated large eddy simulations (LES). The LES functions by calculating the dynamic eddy behaviour by resolving the larger eddies explicitly while approximating the behaviour of the small scale eddies. This is a faster method than the DNS approach, which solves the entire spectrum of eddies, from small Kolmogorov fluctuation to large scale eddies Still, it is a very computationally demanding method. (Rodriguez, 2019). Detached eddy simulations combines LES and RANS as a way of limiting the computational cost of using only LES, while avoiding potential issues with RANS in large separation regions. It does this by treating the attached boundary layers using RANS, while the LES approach is applied to separated regions (Spalart, 2009). This way it improves the ability to predict flow separation.

The delayed detached eddy simulation (DDES) and the improved delayed detached-eddy simulation (IDDES) are versions of the DES that were created to tackle issues that can occur in the border area between LES and RANS. Such as grid-induced separation which can occur in thick boundary layers with fine meshing, when the grid spacing parallel to the wall becomes smaller than the thickness of the boundary layer and can cause issues in the border area between the LES and RANS. (Spalart, Deck, Strelets, & Travin, 2009).

4.4 Free surface modelling

Modelling the free surface can present some particular challenges in CFD. Solutions specially adjusted for handling it is necessary due to the complex geometries and nonlinear influences, such as wave breaking and spraying.

When modelling free surfaces there are two boundary conditions to consider: the kinematic and the dynamic. The kinematic conditions assumes that all fluid particles on the surface will remain on the surface (Faltinsen, 2005). Hence, the condition connects the motion of the free surface to the fluid particle velocities at the free surface. It does this by implying that the normal component of the fluid particle velocity at the surface is equal to the normal component of the free surface velocity.

The dynamic condition states that momentum at the free surface should be conserved and that all forces working on the free surface are in equilibrium. Meaning that the fluid pressure at the surface must be equal to the atmospheric pressure (Faltinsen, 2005).

In general, there are two methods for modelling the free surface. Either by interface tracking or interface capturing. Tracking means that the domain follows the free surface and that the grid adapts after it. This method is limited as it is unable to solve problems that involves large deformations of the grid, such as steep or breaking waves. Capturing means solving the RANS

equation over a grid that covers the entire domain, it is more demanding, but it allows for more complex problems (Molland et al., 2011).

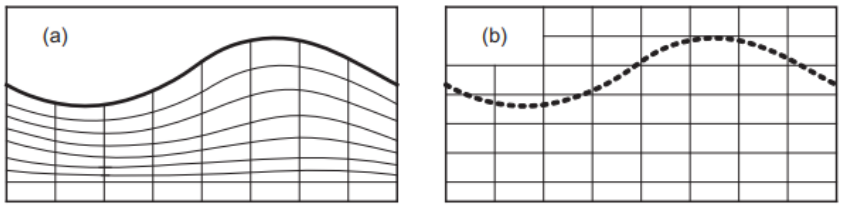

Figure 4.2: The two methods for free surface modelling in CFD. (a) shows grid generation by tracking and (b) shows interface capturing method. Reprinted from Molland et al. (2011, p. 171)

Volume of Fluid (VOF) is an interface capturing method that locates the free surface by using a fractional function, B (Hirt & Nichols, 1981). The function is assigned a value between one and zero ($0 \leq B \leq 1$). For tracking the surface between two different fluids, B is defined as zero if only fluid 1 is present and $B = 1$ if only fluid 2 is present. If $0 < B < 1$, it means that there is an interface present. It does not give very detailed results at first and must therefore be iterated with grid refinements until satisfactory results are achieved.

4.5 Numerical uncertainties

The uncertainties and errors related to numerical modelling can be summarized as follows (Tu, Yeoh, & Liu, 2013):

- *Convergence errors.* These are generated in the iteration process and can occur if the model has not yet fully converged.
- *Discretization errors.* These stems from approximations in the space and time discretizations, which will cause a difference in the CFD solution compared to the exact solutions of the governing equations.
- *Round off errors.* Computers use a finite number of digits, this leads to errors when the variables are rounded off.
- *Modelling errors.* Errors caused by simplifications or other uncertainties in the models and related parameters.
- *Human error* caused by the CFD user.

4.6 Fine/Marine

The integrated CFD software Fine/Marine was developed by the company Numeca International and can be used for the simulation of both mono- and multi-fluid flows around various types of vessels. As most CFD solvers, the software analyses the problem over three steps: (1) pre-processing, (2) solver and (3) post-processing. A flow chart is shown in figure 4.3. The domain set up and general parameters are handled directly in the programs interface, while the internal systems HEXPRESS, ISIS-CFD and CFview has been specifically created for the

remaining steps. (Wackers, 2021) They will be briefly expelained below.

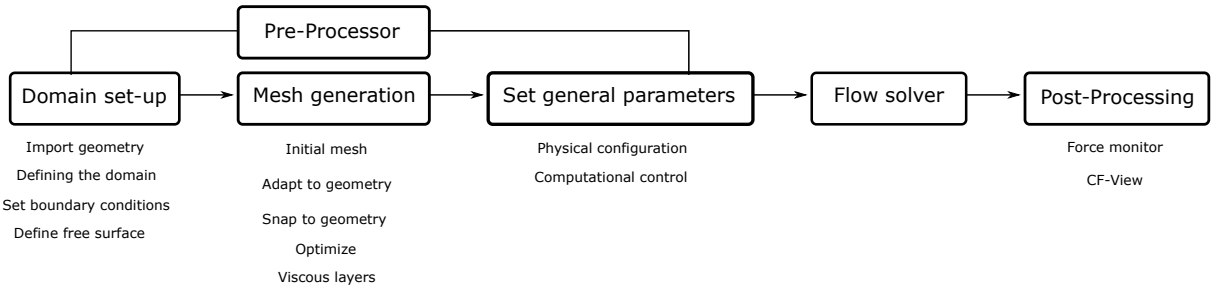

Figure 4.3: Flow chart of the flow solver process in Fine/Marine

HEXPRESS is an automated grid generator system that solves the pre-processing step. By using unstructured hexahedral meshes it is able to generate meshes for various complex geometries. Here the domain and geometry of the problem is defined and the mesh is generated. The Volume of Fluid method (VOF) is used for modelling the free surface. The entire mesh generation is processed over five steps:

1. Initial mesh
2. Adapt to geometry
3. Snap to geometry
4. Optimize
5. Viscous layers

ISIS-CFD is a three dimensional flow solver within Fine/Marine developed by Ècole centrale de Nantes. Incompressible RANS-equations are to solve the governing equations and the transport equations are then discretized using the finite volume method. Here, during the solver step the physical properties of the flow problem are set, such as flow type and turbulence model (Numeca International, n.d.).

CFView is the post-processor and the final step of the simulation process. Here, the solution is visualized using visualization methods such as vector fields and iso-surfaces that can be used for analysing.(Numeca International, n.d.)

Chapter 5

Characteristics of the bow wave

The bow wave is the dominating wave system for a ship and therefore also for a surface-piercing hydrofoil, as it functions as a proxy for a ship hull. Hence, it is interesting to look into some of the bow waves characteristics as it will be the most defining for the resulting wave profile.

Some of the aspects that make the bow wave interesting, is the fact that it only depends on the shape of the bow and is independent of factors such as the ship length or the geometry behind the bow. Additionally, as it is very affected by non-linearities, wave breaking can often occur.

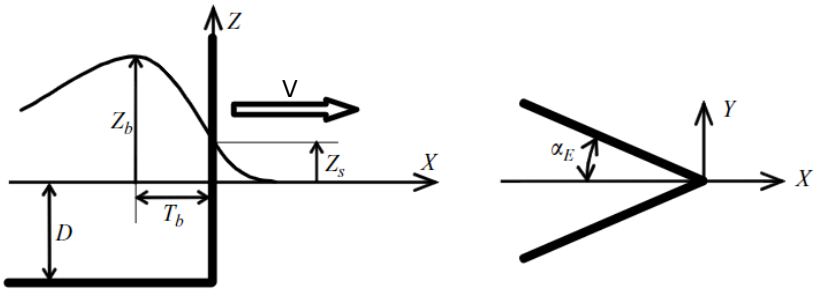

Figure 5.1: Coordinate system (x,y,z), bow wave height (Z_b), water rise (Z_s), distance between wave crest and ship stem (T_b), ship draught (D) incoming velocity (U) and waterline entrance angle $2\alpha_E$ defined. Reprinted from Noblesse et al. (2008, Fig. (1))

As noted by Noblesse et al. (2013); for numerical and analytical purposes, a ship in steady motion is assumed to produce a steady bow wave. However, this is not always the case. It can be easily be proved through observation that ships in steady motion can generate unsteady bow waves. Especially slow ships with blunt bow shapes often develops turbulent breaking waves. The bow wave is therefore divided into two categories: steady and unsteady bow waves. Steady or overturning bow waves, are thin sheets of water that mostly remain steady until they hit the free surface (Noblesse et al., 2008). While the unsteady waves are turbulent, breaking waves. Noblesse et al. (2013), presented a simple criterion to predict whether a ship would produce a steady or unsteady bow wave by using velocity, draught and the waterline entrance angle as parameters (see figure 5.1), which will be summarized in the section, along with other characteristics of the wave.

The non-dimensional height of a bow wave for a ship with a non-bulbous wedge-shaped bow can be expressed as:

$$z_b = \frac{Z_b g}{V^2} \approx \frac{2.2}{1 + Fn_h} \frac{\tan \alpha_E}{\cos \alpha_E} \tag{5.0.1}$$

Where α_E is half the waterline entrance angle, which is defined as the angle between the centerline and the tangent to the waterline at the bow, Z_B is the bow wave height and F_{nh} (eq.

(7.0.1)) is the depth based Froude number and z = 0 at the mean free surface.
By using the Bernoulli relation at the free surface one gets:

$$\frac{p}{\rho} + gz + \frac{[(u-V)^2] + v^2 + w^2}{2} = \frac{p_{atm}}{\rho} + \frac{V^2}{2} \tag{5.0.2}$$

V and (u, v, w) are the incoming velocity and the flow velocities due to the ship. The coordinate system (x, y, z), moves with the ship, Z is the vertical direction pointing upwards, defined as zero at the mean free surface. X goes along the ship path and is positive towards the bow.

By applying equation (5.0.2) to the free surface ($p = p_{atm}$), an upper bound for the free surface elevation can be found to be:

$$\frac{Z_b g}{V^2} \leq \frac{1}{2} \tag{5.0.3}$$

From the previous equations, a criterion that separates the regimes where an unsteady or steady, overturning bow wave can be found:

$$Fn_h(\alpha_E) = \frac{V}{\sqrt{gh}} = \begin{cases} 0 & \text{if } \alpha_E \leq \alpha_E^B \\ \frac{4.4 \tan \alpha_E}{\cos \alpha_E} - 1 & \text{if } \alpha_E \geq \alpha_E^B \end{cases} \tag{5.0.4}$$

With the waterline entrance angle $2\alpha_E$ that defines the border between steady and unsteady bow wave as:

$$\alpha_E^B \approx 12.5^\circ \tag{5.0.5}$$

Which means that the critical waterline entrance angle is $2\alpha_E \approx 25^\circ$. Meaning that a vessel with a waterline entrance angle ($2\alpha_E$) smaller than approximately 25°, can create an overturning bow wave at any velocity, while one with a waterline larger than 25°will generate unsteady waves, unless it has a higher Froude number than defined by equation (5.0.4).

The height of an unsteady wave will be approximately the same as the upper bound for the bow wave height (eq. (5.0.3)) (Noblesse et al., 2008):

$$z_b = \frac{Z_b g}{V^2} = \frac{1}{2} \tag{5.0.6}$$

Noblesse et al. (2013) also gave the following equation for the energy in breaking and non-breaking waves. For a non-breaking wave, the energy transported in deep water can be expressing in simple terms and is proportional to the wave amplitude (A):

$$e_{NBW} \propto \frac{\rho g A^2}{2} \tag{5.0.7}$$

An unsteady wave is much more complex and cannot be expressed in terms of A, it can however be assumed to depend on the volume (∇) of the wave and can be related to the drag on the ship bow. The energy of a breaking wave can therefore be assumed to be proportional to ∇:

$$e_{BW} \propto \rho \nabla V_s^2 \tag{5.0.8}$$

Chapter 6

Waterline measurement

To analyse the wave profiles of the surface-piercing hydrofoil, it is necessary to accurately reconstruct the waterline. There are several ways of doing this, which comes with different advantages and disadvantages. Placing an underwater camera at a set location, that photographs the hull as it passes by is one of the most common ways to do this. This is relatively simple and gives reliable results. However, the approach is limited, as it only provides results at the moment when the object passes the camera. This means that details and aspects can get lost. Another possible method includes placing electrical wetting probes around the hull, a widely used method, but it can be intrusive and thereby affect the results. Other methods such as painting techniques are also used. (Nataletti et al., 2019).

A non-intrusive method of detecting the wave profiles was proposed by Nataletti et al. (2019), which will presented here. The procedure is planned to be used to estimate the wave profiles from the towing test. In the study by Nataletti et al. (2019), two cameras were fastened to the towing carriage above the waterline, astern the hull. This has been done previously, but the procedure leaves one with the issue of accurately translating the waterline into spatial coordinates. The proposed solution was to place the cameras such that the contrast between the solid hull and the fluid were visible and could be tracked using computer vision technique. In this way, the location of the waterline could be identified. These points are then translated from the coordinate system used in the experiments to a standard ship coordinate system, making it possible to reconstruct the waterline there.

Computer vision uses a triangulation technique to detect the position of a point in a 3D space. To be able to do this, the cameras were calibrated against a known geometry pattern, to define the perspective projection matrix of the cameras. By using two cameras, an epipolar plane can be defined, which creates a constraint for the projected point, such that one can approximate the position of a point on an epipolar line.

By using reference points on the hull its also possible to determine the pose of the model in the cameras reference system, meaning the position and orientation in the space. The reference are reproduced from CAD drawings. This both allows one to transform coordinate points to the stereo camera and to find valid pictures that are not too affected by vibrations from the set up. Afterwards the waterline is identified in both camera images and filtered with a low pass filter. Triangulation then allows one to track the waterline, before the 3D locations of the waterline can be reconstructed to the CAD system.

The method showed some discrepancy when validated, the relative error was usually around 10-15%. Nataletti et al. (2019) also commented that the error increased with increasing distance between camera and hull. There were also difficulties identifying the waterline if reflections from the water or other visual disturbances were present. Still, the method presents a non-intrusive method that was able to track the waterline with an overall good level of accuracy.

Chapter 7

Ventilation

Ventilation occurs when a non-condensible gas, such as air enters into the separated wake of an object and generates a multi-phase flow. (Faltinsen, 2005). In the case of a surface-piercing hydrofoil in water, it occurs when an air channel is generated from the free surface to the suction side of the foil. It can be an important factor for lifting bodies operating close to the free surface, especially those operating at high velocities or at a large yaw angle. Examples of candidates in high risk of ventilation are rudders, surface piercing foils, propellers and foils operating close to the free surface. This section will go deeper into the characteristics of a ventilated flow by reviewing studies written on the subject.

Ventilation possesses similarities to cavitation, with the biggest difference being that a ventilated flow is multi-fluid. For simplicity, ventilation is often referred to as a cavitated flow or as cavitation throughout this text, it should however not be confused with the phenomenon where low pressure generates vapour-filled cavities. Unlike cavitation, ventilation does not pose a risk when it comes to sound and fatigue as the air bubbles does not implode. It does however, affect the performance of the foil, especially the lifting force can be drastically reduced, which can result in loss of vessel speed, stability and manoeuvrability. (Harwood et al., 2014) Still, ventilation can in some cases be used to ones advantage. If the device has been designed well, ventilation can lead to improved stability and a reduction in drag under certain conditions. (Faltinsen, 2005). However, a drastic change in the lift/drag ratio, will in most cases have negative consequences. As ventilation can majorly affect the performance of the vessel, it is important to understand the physics of ventilation and how and why it occurs.

For ventilation to develop and be sustained there are two requirements that must be fulfilled according to Swales et al. (1974)

- Sub-atmospheric pressure at the suction side of the foil
- Flow separation around the foil.

As noted by Swales et al. (1974), no ventilation will occur unless both conditions are fulfilled. However, they are not sufficient in themselves: an air channel must be supplied continuously to the separated wake for ventilation be sustained. Hence, the surface layer of the free surface must be broken such that air can enter. How this usually occurs will be discussed further in section 7.4.

The development of ventilation depends on the factors, angle of attack (α), the immersed Froude number, Fn_h and the immersed aspect ratio, AR_h (Young et al., 2017). For simplicity they will often be referred to as only Froude number and aspect ratio forwards in this text.

$$Fn_h = \frac{V}{\sqrt{gh}} \tag{7.0.1}$$

$$AR_h = \frac{h}{c} \tag{7.0.2}$$

Here, c is the chord length of the foil, h is the submerged depth, and $g = 9.81 m/s^2$ is the gravitational acceleration.

According to Breslin and Skalak (1959) a ventilated flow is considered stable if it meets the following criteria:

$$C_L \geq 5Fn_h^{-2} \tag{7.0.3a}$$

$$Fn_h \geq 3 \tag{7.0.3b}$$

7.1 Two-Dimensional cavity flows

It is useful to look at a two-dimensional cavity flow around a cross section to better understand how one can approach three-dimensional cases. The two-dimensional force coefficients for lift, drag and yaw moment are defined as:

$$C_{L_{2D}} = \frac{L}{0.5\rho V^2 c} \tag{7.1.1a}$$

$$C_{D_{2D}} = \frac{D}{0.5\rho V^2 c} \tag{7.1.1b}$$

$$C_{M_{2D}} = \frac{M}{0.5\rho V^2 c^2} \tag{7.1.1c}$$

Where L, D and M are the lift, drag and moment forces per unit section with origin around the mid-chord. The chord length is defined as c. The coordinate system of the 2D foil can be seen in figure 7.1.

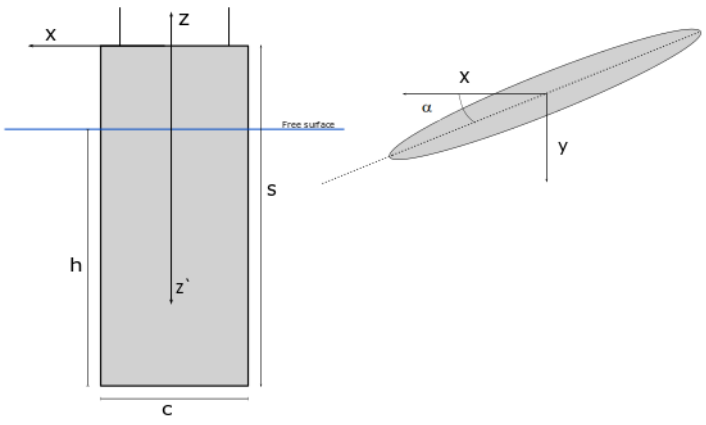

Figure 7.1: Coordinates defined for 3D and 2D foil

The flows around the foil was characterized by (Harwood et al., 2014) as either fully wetted (FW), partially ventilated (PV) or fully ventilated (FV). These concepts are explained more detailed in section 7.3. The flow regime surrounding the foil will as mentioned, affect the forces.

Young et al. (2017) presented the following equations for the cavity length and force coefficients in the three flow regimes.

A fully wetted flow has no substantial or sustainable amount of ventilation. For a streamlined hydrofoil with no camber the force coefficients can be simplified to:

$$C_{L_{2D}} = 2\pi\alpha_{2D} \tag{7.1.2}$$

$$C_{D_{2D}} = 0 \tag{7.1.3}$$

$$C_{M_{2D}} = \frac{\pi}{2}\alpha_{2D} \tag{7.1.4}$$

A partially ventilated flow has a span that is partially covered in ventilated cavities. L_c is the length of the cavity, and L_c/c is the non-dimensional cavity length, which for a PV flow must be in the region $0 < L_c/c < 1$. The following values are for partial leading edge cavity (Young et al., 2017).

$$\frac{L_c}{c} = \cos^2\beta \tag{7.1.5}$$

$$\frac{\sigma_c}{\alpha_{2D}} = 2\cot\beta\frac{1+\sin\beta}{1-\sin\beta} \tag{7.1.6}$$

$$C_{D_{2D}} = \pi\alpha_{2D}^2(1+\frac{1}{\sin\beta}) \tag{7.1.7}$$

$$C_{M_{2D}} = \frac{\pi\alpha_2 D}{8}(-3-6\sin\beta+\sin^2\beta+4\sin^3\beta) \tag{7.1.8}$$

Here, β is a transformation variable.

For a fully ventilated flow, the cavitational regime extends over the entire suction side and the characteristics are as given by Young et al. (2017).

$$\frac{c}{L_c} = \cos^2\beta \tag{7.1.9}$$

$$\frac{\sigma_c}{\alpha_{2D}} = 2\cot\beta \tag{7.1.10}$$

$$C_{L_{2D}} = \pi\alpha_{2D}\frac{1}{\sin\beta(1+\sin\beta)} \tag{7.1.11}$$

$$C_{D_{2D}} = \pi\alpha_{2D}^2\frac{1}{\sin\beta(1+\sin\beta)} \tag{7.1.12}$$

$$C_{M_{2D}} = \pi\alpha_{2D}\frac{4+\sin\beta}{8\sin\beta(1+\sin\beta)^2} \tag{7.1.13}$$

7.2 Hydrodynamic forces

The hydrodynamic forces; lift, drag and moment are all to some extent effected by ventilation. Lift reduction is the dominating effect, but it can also lead to changes in the drag force and yaw moment. How these changes specifically affects them are further discussed in this section.

The replacement of a low pressure liquid (water) for a higher pressure gas (air), can cause a dramatic loss of lift on the foil. Pressure below the atmospheric pressure is a requirement for ventilation to develop, however, it is usually substantially lower than that on the suction side. When ventilation occurs and the low pressure side is covered in aerated cavities, the pressure will be constrained by the atmospheric value, $p_c = p_{atm} = 101$ kPa. This can mean a huge change in the lift force and the lift/drag ratio. Reductions of up to 70% of the lifting coefficient were reported by Breslin and Skalak (1959). At large Froude numbers and positive yaw angles, the direction of the lift might also be reversed (Young et al., 2017).

Harwood et al. (2014) reported that the total drag, is not affected in any large extent by the multi-phase flows. Instead, the viscous drag is decreased as air has a lower viscosity than water. Simultaneously, the pressure drag increases. This means that the changes in drag cancels each other out and the force will remain approximately the same. Although this is what generally occurs, it should be noted that a drag loss might occur for certain conditions and foils, as reported by (Breslin & Skalak, 1959).

Overall change in pressure on the foil has an affect on the yawing moment as well. Harwood et al. (2014) and Young et al. (2017) notes that it leads to a non-linear increase of the moment and that the change in pressure on the suction side results in the pressure centre moving towards the mid- point of the foils chord length.

The three dimensional lift, drag and yaw moment coefficients can be calculated as (Faltinsen, 2005), where L is the lift force, D is the drag force and M the moment in yaw:

$$C_{L,3D} = \frac{L}{\frac{1}{2}\rho V^2 hc} \tag{7.2.1}$$

$$C_{D,3d} = \frac{-D}{\frac{1}{2}\rho V^2 hc} \tag{7.2.2}$$

$$C_{M,3D} = \frac{M}{\frac{1}{2}\rho V^2 hc^2} \tag{7.2.3}$$

7.3 Flow regimes

Harwood et al. (2014) establishes three ventilated flow regimes that are recognised by their flow stability. These flows were termed as fully wetted flow (FW), fully ventilated flow (FV) and partially ventilated flow (PV). The authors specified that the term stability used here, should not be mistaken for steadiness. The PV flow for example, will in all cases be unsteady. By stability it refers to the flows ability to remain in the specific region. To distinguish between the flows, three criterion were established by (Harwood et al., 2016):

- H = 0 for FW flows
- H = h and $\Phi < 45°$ for FV flows

- $0 > H > h$ or $\Phi \geq 45°$ for PV flows

Here, H is the depth of the cavity, measured from the free surface and downwards and Φ is the local angle of the cavity closure line. (See figure 7.2).

The angle, Φ defines the linearized angle of the cavity closure line, related to the re-entrant jet. The jet develops from a cavity closure, meaning the area where the cavity flow reattaches to the surface of the foil. The streamlines inside the stagnated flow are forced to induce a jet that undercuts the cavity (Harwood et al., 2016). It is a common phenomenon for cases such as cloud cavitation, where it leads to a periodic shedding of the downstream part of the cavitation (Kuiper, 1998). As explained by Harwood et al. (2014), the direction of the jet can be generalized to a reflection of the incoming flow. If Φ surpasses 45°, the jet will have a upwards direction. This causes instability in the flow and possibly a large scale shedding of the cavities and a closure of the air channel. Hence, a flow with a re-entrant jet with an angle larger than 45° must be considered partially ventilated.

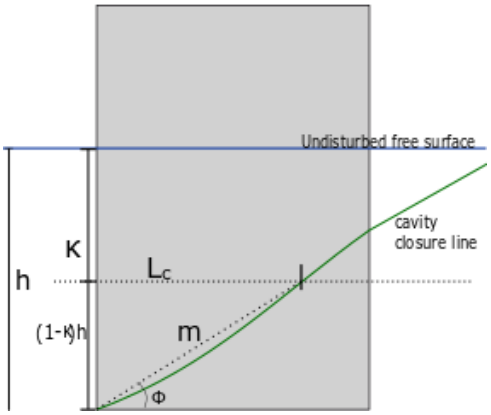

Figure 7.2: Representation of the cavity closure line, with Φ, L_c, m and κ defined

Harwood et al. (2014) and Young and Brizzolara (2013) characterized three different flow regimes, which will be defined in this section (in the article by Young and Brizzolara, the first two regimes are referred to as fully attached and transitional). A mapping of these regimes as a function of Froude number and angle of attack is shown in figure 7.4.

Fully wetted flow is a non-ventilated regime. It is defined as not having any large degrees of air entrapment and an unruptured free surface. As noted by (Swales et al., 1974), this was a requirement for ventilation to occur as it allows air ingress when vortices drags air down from the surface. The free surface around the trailing edge can be deformed and distorted, but the perturbations are not large enough to cause significant air supply to the separated flow. Small aerated areas of cavities are often observed in the wake behind the trailing edge, but as they are only located in a small and confined area, they do not develop or affect the flow significantly.

Partially ventilated flow is the unsteady region of flow that exists between the fully wetted and the fully ventilated flow. The perturbations on the surface has generates air supply to the surface of the foil and ventilation occurs. However, the cavity does not cover the entire depth of the suction side, causing a mix of flows to be present.

Fully ventilated flow, the free surface is ruptured and the ventilated cavities covers the entire span of the suction side. This can be observed as smooth cavity walls. Breslin and Skalak (1959). The stability criteria for a ventilated flow are met and no destabilizing re-entrant jet

exists.

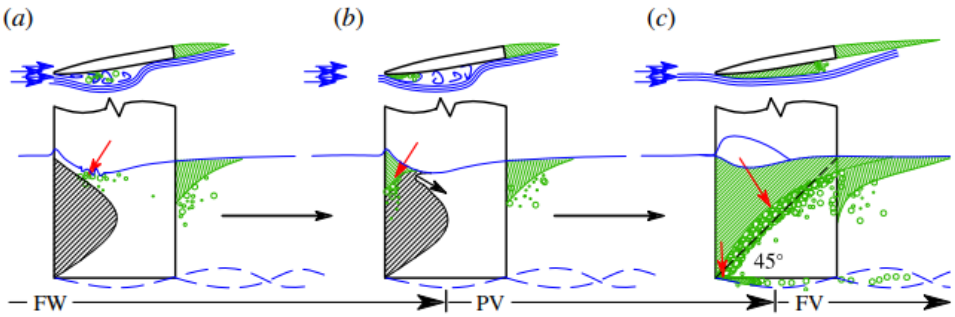

Figure 7.3: Ventilation formation from FW to FV flow by a spontaneous stall-induced ventilation. Black hatches shows boundary layer separation, blue lines are streamlines, green hatchings shows areas of air entrapment and the red arrows indicates the paths of air entering. Reprinted with permission from Harwood et al. (2016, Fig. (18))

Bi-stable regions are regions of unstable flow that appear in between and overlaps the mentioned regimes. In these areas the flow can go either towards fully ventilated, partially ventilated or fully wetted. A mapping of these areas can be seen in figure 7.4
From experiments done by Harwood et al. (2016), it was shown that fully ventilated flows only exists past the stall angle, which is where the maximum lift coefficient is found. If the Froude number is sufficiently high, the flow will be forced to separate past this point. Ventilation will then occur and the lift drops. The lowest angle where wetted flow and ventilated flows can intersect is known as the bifurcation angle (α_b) (Damley-Strnad et al., 2019). At angles lower than the α_b only wetted flow remains.

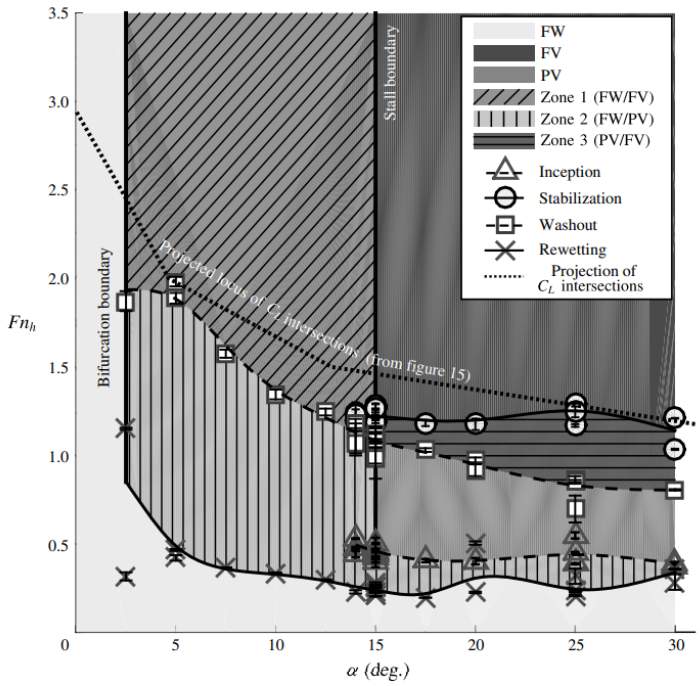

Figure 7.4: Steady flow regime map for a hydrofoil with AR_h = 1.0. The flow regimes are plotted as a function of the yaw angle and Fn_h. Reprinted with permission from (Harwood et al., 2016)

7.4 Ventilation inception

Harwood et al. (2016) experiments on surface-piercing hydrofoil, went into details about how a ventilation forms and disappears. Ventilation formation refers to the transition from a non-ventilated state to a fully ventilated flow, while elimination is the transition back from ventilation to fully wetted flow. Inception occurs when the change in flow is initialized and aerated cavities forms along the surface of the foil. Unless the cause of the inception subsides, the flow will start to stabilize. The stabilization can be viewed as the transition between partially ventilated and fully ventilated flow. (Harwood et al., 2014)

According to Harwood et al. (2016), ventilation inception generally occurs in two different manners. Via spontaneous inception or perturbation inception. Wetzel (1957) and Breslin and Skalak (1959) also described these, but referred to them as creeping and flash ventilation or as spontaneous and forced inception.

Spontaneous inception are self-generated forms of ventilation that develops naturally without outside intervention. They are generated when the vortices from the wake breaks through the surface layer and an air channel is created. There are different manners in which such ventilation can develop, Harwood et al. (2016) describes two types, (1) stall-induced formation and (2) tip vortex formation a third type, tail ventilation was described by Swales et al. (1974). Wetzel (1957) also observed these types and made the conclusion that the first develops at high yaw angles and the second at low yaw angles.

Spontaneous stall-induced ventilation is a form of spontaneous ventilation observed by Harwood et al. (2016), Swales et al. (1974) and Breslin and Skalak (1959). It starts to form when the yaw angle exceeds the stalling angle. Meaning the point where the angle becomes so large that it forces a separation in the boundary layer, which leads to a lift reduction. The stall angle can therefore be found from the maximum lift coefficient. Harwood et al. (2016) describes the stall-induced inception that starts to develop from a large vortex, it generates a separation in the flow starting from the leading edge. Eventually, this can grow to cover the entire suction side. Meanwhile, perturbations in the wake forms small vortices under the surface and the depressed surface creates instabilities that can lead the perturbations too be easily magnified. This will eventually cause the surface to rupture (Swales et al., 1974). If the air ingress is sufficient, the flow transitions into a ventilated flow, this usually happens rapidly. The transition from fully wetted to fully ventilated for a spontaneous stall angle can be viewed in figure 7.3.

Tail ventilation usually occurs at higher velocities and moderate yaw angles and was observed in the works of Swales et al. (1974). It is similar to the stall induced inception, but the air ingress has a more complex mechanism behind it. The air channel is formed close to the trailing edge and is caused by Taylor instabilities that develops when the wake behind the foil is accelerated downwards. This leads to air ingress through a train of small perturbations, hence it develops slowly and can spend a relatively long time in the partially ventilated regime. (Young et al., 2017) (Swales et al., 1974).

Tip-vortex inception is another form of spontaneous inception that forms from a strong trailing tip vortex that draws air down to the tip. It was described by (Harwood et al., 2016) and (Young et al., 2017) as expanding rapidly from wetted to fully ventilated, with very little time spent in the partially ventilated region. Hence, the name flash ventilation in the work of Wetzel (1957). Young et al. (2017) notes that this is most likely due to the fact that the flow is already susceptible to ventilation at the angles and velocity needed to generate a strong tip vortex. This type of ventilation is common for fully submerged lifting surfaces at shallow depths, such as

shallowly submerged propellers.

If no natural perturbations are sufficient to rupture the surface layer, the flow can stay in the fully wetted region long after the ventilation conditions are met. In these cases, *forced inception* or *perturbation induced inception* can be introduced. Here, the inception is triggered by an external disturbance in the surface of some kind. Breslin and Skalak (1959) studied the phenomenon by inserting a small, sharp object into the free surface. It was observed that an immediate flow separation took place in the area and ventilation was induced by the trailing edge. Harwood et al. (2016) suggested injecting high pressured air into the wake would also work for this. It was noted by Harwood et al. (2016) that these methods works so effectively, despite having shorter leading edge separation bubbles that are unable to rupture the surface, because there exists a thin layer of separated flow just beneath the surface. By manually breaking it, ventilation can easily and rapidly be reached.

7.5 Prevention and elimination of ventilation

Elimination is the process where ventilation is destabilized and reduced, such that it returns to a partilly ventilated or fully wetted regime. This typically happens when the velocity or the angle of attack is reduced. Harwood et al. (2014) describes the elimination, or "washout", meaning the transformation from a ventilated to non-ventilated flow, as a two step process. First, it is the actual washout. This is caused by a destabilization in the flow that transitions it from fully to partially ventilated, as it no longer meets both criterion for a fully ventilated flow. Lastly, there is a reattachment of the separated flow, which marks the transition back to a completely attached flow, also called "rewetting". It is usually the re-entrant jet that that initiates the washout process as it steepens and surpasses the 45° limit. This was demonstrated in an experiment by Harwood et al. (2014), where a surface-piercing hydrofoil was decelerated while kept at a constant yaw angle. As the velocity reduced, the cavity length was reduced, however the cavity depth remained the same, such that the cavity closure line steepened and exceeded the maximum angle. This made the jet move upwards and parts of the cavitation was cut off. Neither of the ventilation criterion were met any longer. An exception to this is when the angles are very low ($\alpha \leq 5°$), for these cases the jet lacks sufficient momentum to be able to undercut the cavity (Young et al., 2017). Instead the cavities are reduced gradually as there is a turbulent reattachment of the streamlines.

Harwood et al. (2014) also introduced an expression for the critical washout Fn_h by using the cavity closure angle. The 45° criterion gives a slope, m. The definitions of m and κ is illustrated in figure 7.2.

$$m = \frac{(1-\kappa)h}{L_C} = 1 \tag{7.5.1}$$

Where all variables are defined in figure 7.2.

A non-dimensional approximation of the cavity length, L_C is given by:

$$\frac{L_c}{c} = a\left(\frac{\alpha_{eff}}{\sigma_c}\right)^b \tag{7.5.2}$$

Where a and b are constants, σ_c is the cavity number and α_{eff} is the effective angle of attack. Which can be approximated to the following for a fully ventilated vertical foil:

$$\alpha_{eff} = \alpha\frac{2AR_h}{2AR_h + 1} \tag{7.5.3}$$

α is the angle of attack and AR_h is the immersed aspect ratio (eq. (7.0.2)). By combining the expressions it gives:

$$1 = \frac{(1-\kappa)h}{L_C} = \frac{1-\kappa}{a(\frac{AR_h F_{Nh}^2 \alpha}{\kappa(2AR_h+1)})^b}\frac{h}{c} = \frac{1-\kappa}{a(\frac{AR_h F_{Nh}^2 \alpha}{\kappa(2AR_h+1)})^b}AR_h \tag{7.5.4}$$

This can the be solved for a critical Froude number $Fn_{h_{washout}}$ as a function of non-dimensional parameters, which marks when washout initiates:

$$Fn_{h_{washout}} = \sqrt{\frac{\kappa(1-\kappa)^{1/b}}{a^{1/b}}\frac{(2AR_h+1)}{AR_h^{\frac{b-1}{b}}}\frac{1}{\alpha}} \tag{7.5.5}$$

Hysteresis plays an important role when one looks at the ventilation process. Instinctively, one might think that washout is initiated at the same conditions as formation begins. This is however not the case. As stated by Rothblum et al. (1969, p. 5): *The previous non-ventilated regime usually cannot be reestablished simply by restoration of the previous conditions on the fluid boundaries.* During their experiments it was found that ventilation persisted down to and even slightly beyond a yaw angle of zero degrees. Harwood et al. (2016) observed that ventilation characteristics was found to persist down to the bifurcation angle, after this all flows were reported to be fully wetted. The bifurcation angle was found by Harwood et al. (2016), to be $\alpha_b \approx 2.5^\circ$, but this can vary with the geometry. Damley-Strnad et al. (2019) named five critical angles, here the rewetting angle α_{rewet} is defined as the point where the flow naturally returns to fully wetted, while α_b is the lowest angle where wetted and ventilated flow intersects.

As unwanted ventilation can cause many negative side-effects it is useful to look at ways to prevent it. Swales et al. (1974) suggested using fences placed normal to the foil on the suction side, as it physically stops nose ventilation from progressing beyond the fence. It does, however increase the vorticity and for tail ventilation, inception can actually occur slightly earlier. Another way of preventing ventilation is by separation control, delaying the separation would prevent ventilation but this is complicated and there is no effective and practical way of doing this yet. When ventilation first occurs, it can, as mentioned, be eliminated by reducing either the velocity or angle of the foil.

7.6 Scale effects

This section looks into some of the challenges and requirements for scaling models that are prone to ventilation. The usual requirements for geometric, kinematic and dynamic similarities apply (Molland et al., 2011). Geometric similarity is easily achieved by keeping the same shape and AR_h ratio for model and full scale. Young et al. (2017) notes that is also necessary to keep the same sectional cavitation number σ_c to ensure that the ratio between cavity pressure (p_c) and hydrostatic pressure (p_0) remains the same. Dynamic similarity requires that the Froude number (Fn_h) is kept equal. There are however some other aspects that should be considered as well, that will be discussed in this section.

The Weber number (We) represents the ratio between the fluid inertia and surface tension and is useful when one is looking at multi-phase flows. We may affect the scaling as the surface tension can cause changes in the surface wave and spray sheet pattern for smaller models. It has however, been shown that for $We \geq 250$ the surface tensions are negligible. (Young et al., 2017), (Harwood et al., 2016).

$$We = \frac{\rho u^2 c}{\gamma} \geq 250 \tag{7.6.1}$$

Where γ is the surface tension.

The Reynolds number influences the development, location and extent of the flow separation, keeping the Reynolds number equal for model and full scale can be one of the more challenging aspects of ventilation scaling (Young et al., 2017), and turbulence simulation is often necessary to obtain similar conditions. For a surface-piercing hydrofoil, the relevant Reynolds number is based on the chord length:

$$Rn = \frac{Vc}{\nu} \tag{7.6.2}$$

Other factors that can influence scaling for ventilation susceptible lifting bodies are flow compressibility, symbolized by the Mach number (Ma). Young et al. (2017) mentions the effects of Ma could affect the cavity shedding frequency. This is however negligible as long as $Ma \leq 0.1$. It was also documented by Rothblum et al. (1969) that the presence of waves also have an influence as they cause disturbances in the surface and a body is often more susceptible to ventilation in open sea than for model testings.

7.7 The effect of added mass on ventilation

As noted by Harwood et al. (2016), the two- dimensional lift and drag force can be divided into a steady and unsteady component as follows:

$$L = L_{unsteady} + L_{steady} \tag{7.7.1a}$$

$$D = D_{unsteady} + D_{steady} \tag{7.7.1b}$$

The unsteady forces are defined by the added mass due to the inertia forces that arise when the body is accelerated in a fluid. By looking at a 2D section of a foil, the unsteady force components can then be described as:

$$L_{unsteady} = m_{21}a = \frac{1}{2}\pi\rho(\frac{c}{2})^2 \sin^2(\alpha)V \tag{7.7.2}$$

$$D_{unsteady} = m_{11}a = \pi\rho(\frac{c}{2})^2 \sin^2(\alpha)V \tag{7.7.3}$$

Where m_{21} and m_{11} are added mass components, where the first subscript denotes the direction of the force and the second gives the direction of the unit acceleration that causes the inertial component, where (x, y, z) = (1, 2, 3). V and a, are the velocity and acceleration of the incoming flow respectively.

This gives the following equations:

$$L = \frac{1}{2}\pi\rho(\frac{c}{2})^2 \sin^2(\alpha)V + \frac{1}{2}C_L\rho V^2 c \tag{7.7.4}$$

$$D = \pi\rho(\frac{c}{2})^2 \sin^2(\alpha)V + \frac{1}{2}C_D\rho V^2 c \tag{7.7.5}$$

7.8 Analysing ventilation using CFD

Assessing ventilation using numerical simulations presents some particular challenges. Especially when it comes to analysing bi-stable flows that can either reach ventilation or go back to an attached flow. As stated by Charlou et al. (2020), who investigated ventilated flows on a surface-piercing hydrofoil by using a $k-\omega$ turbulence model. They noted that the simulation could easily assume that a bi-stable flow is wetted and stable, when in reality it could rapidly transform into a ventilated flow if perturbations are present. A number of experiments and simulations were also performed by Andrun et al. (2020), who also used a RANS solver in the form of a $k-\omega$ turbulence. It was investigate how CFD is able to handle ventilation problems and how this affects the flow parameters. It was remarked that the simulations could predict and simulate ventilation to a good accuracy at high angles of attack ($\alpha \geq 20°$), but for bi-stable flows, it was dependent on having a very low Courant number ($C = \frac{U\Delta t}{\Delta x} << 1$).

Andrun et al. (2020) results showed that the simulated lift agreed well with experimental results, however the drag was consistently overestimated. For the simulations performed by Charlou et al. (2020), the simulated forces gave similar results as the experimental ones, however the limits for fully wetted and fully ventilated differed due to the difficulties of accurately simulating the flow transitions and bi-stable regimes.

Another issue is the hysterectic effect, as the ventilated flow cannot be viewed by itself, rather in context with the flow history. The same flow conditions could give different flow regimes depending on the history of the flow. Charlou et al. (2020), noted that it was also vital to correctly simulated the stability of the flow, if not the bi-stable regions of the flow could easily be mistaken as safe from ventilation. Simulating natural inception on the other hand is not as vital as outside perturbations can easily occur in real life situations.

Chapter 8

Experimental method

A series of experiments were conducted in a section of the towing tank *Slepetanken* in cooperation with Sintef and NTNU at the centre of Marine Technology on Tyholt. The measurements of the tank section used were $L_x x L_y x L_z$ = 175x10.5x5.6 [m]. The tests took place over four days, February 22-24. Two foils were tested with different immersed Froude numbers and angles of attack with two separate intentions: (1) measuring wave profiles and (2) obtaining and observing a ventilated flow. Note that from here and forward the drag and lift forces are referred to as respectively, F_x and F_y to avoid any confusions with the coordinate systems. The immersed Froude number Fn_h, is referred to as Froude number for simplicity and the immersed aspect ratio, AR_h only as the aspect ratio.

8.1 Force predictions and conceptual choices

The force predictions and conceptual choices were conducted in the project thesis, written autumn 2020. The decision to use two foils were made from the following considerations:

- A wider cross section will generate larger waves and thus make it easier to investigate the wave profiles.
- A slender foil is more at risk for flow separation and is therefore more susceptible to ventilation.

The models were created to fit an already existing rig, *Ottoriggen*, which had a maximum force capacity of 400N. The forces on the foils were predicted using the following equations, where F_y is the drag force and F_x is the lift:

$$F_y = \frac{1}{2}\rho u^2 hc C_L cos(\alpha) \tag{8.1.1}$$

$$F_x = -\frac{1}{2}\rho u^2 hc C_D sin(\alpha) \tag{8.1.2}$$

$$F_{Tot} = \sqrt{F_x^2 + F_y^2} \tag{8.1.3}$$

$$C_L = \frac{2\pi\alpha}{1 + \frac{2}{ARh}} \tag{8.1.4}$$

$$C_D = \frac{C_L^2}{\pi ARh} \tag{8.1.5}$$

The lift coefficients were found by assuming linear growth with the yaw angle, which is a simplification and does not take the stall angle or thickness into consideration. Still, it gives a useful estimation. Tables containing all calculation for velocities and angles in the range: $V = 0{-}2.0 m/s$ and $\alpha = 0 - 30°$ can be found in appendix B.

As the surface effects can generate spray sheet patterns and complicate scaling, a Weber number large enough to be able to neglect the surface effects, meaning $We = \frac{\rho u^2 c}{\gamma} \geq 250$ was also considered. When considering the generation of wave profiles, it was interesting to include the occurence of breaking bow waves. Breaking bow waves can be generated for a objects with waterline entrance angle $2\alpha_E \lesssim 25°$ (see chapter 5). This gives a critical Froude number for generating overturning bow waves, as shown in equation 8.1.6.

$$Fn_h \leq \frac{4.4 \tan \alpha_E}{\cos \alpha_E} - 1 \tag{8.1.6}$$

The range of Fn_h and angles that were tested were based on previous studies mentioned in the literature study. Particularly the mapping of the flow regimes as a function of yaw angles and Froude numbers made by Harwood et al. (2016), see figure 7.4.

8.2 Physical model

Two foils with identical chord length and span, but different thicknesses, were made by employees at NTNU. Main characteristics are summarized in table 8.1. The cross sections are symmetrical in both x- and y-direction and are both based upon a mirrored and elongated NACA0024 profile. The foils are made from Divynicell-plates with a density of $60 kg/m^3$. Composed by one plate with a diameter of 8mm in the centre and two plates with a thickness of 86mm glued to each side of the centre plate. Tracks were milled through the plates to fit a vertical steel shaft with a diameter of 30mm, that will connect the foil to the towing rig. The shaft had drilled holes for four horizontally placed threaded rods to stiffen the foil.

The foils were then milled to achieve their shape. The outside of the foils were painted with a total of three layers of polyester, as well as one layer of glass fibre in polyester. Finally, the foils were plastered, smoothed and lacquered. The slender foil (foil 2) was painted with quadratic squares measuring 25 cm^2, which made it easier to assess the size of the ventilated flow.

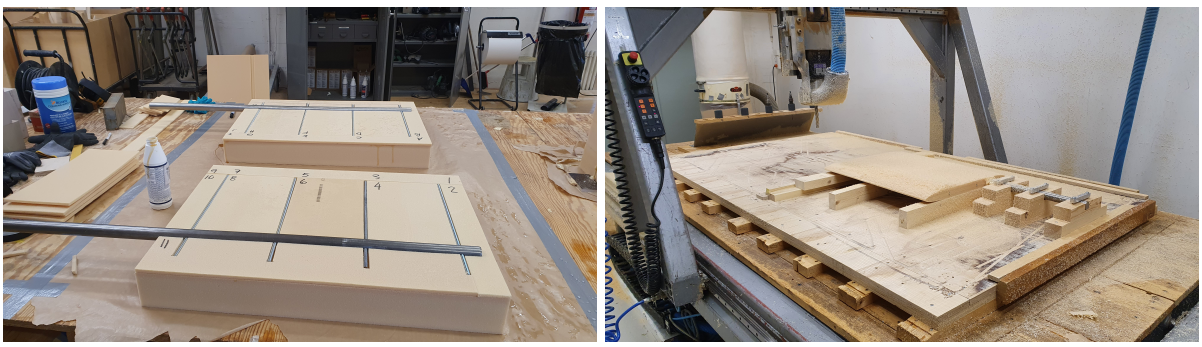

Figure 8.1: The process of making the foils. To the left the plates that composed the foil, as well as the vertical shaft and horizontal rods can be seen. Foil 2 after milling is shown to the right. Photos are taken by Trond Innset.

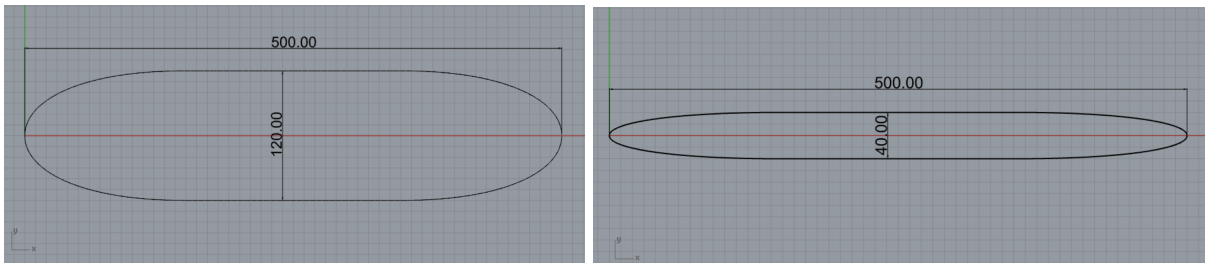

(a) Foil 1: Maximum thickness = 120 mm (b) Foil 2: Maximum thickness = 40 mm

Figure 8.2: Cross sections of the hydrofoils. Foil 1 is used for investigating waveprofiles, while foil 2 is used to achieve ventilated flows.

Table 8.1: Foil characteristics

		Foil 1	**Foil 2**	**Unit**
Chord length	c	500	500	mm
Total span	s	700	700	mm
Submerged depth	h	472	470, 300, 250	mm
Aspect ratio	AR_h	0.94	0.94, 0.6, 0.5	-
Max. thickness	t	120	40	mm
Velocities	V	0.1 - 1.25	0.1 - 2.0	m/s
Froude nr.	Fn_h	0.046 - 0.581	0.046 - 1.437	-
Yaw angle	α	−20° - +20°	−22.5° - +22.5°	deg.

8.3 Model setup

As mentioned previously, the foils were made to fit an already existing rig, *Ottoriggen*. The rig has a maximum force capacity of 400N. By calculating the forces using linear foil theory, it was estimated that for 20° angle of attack, the velocity could be maximum 2m/s, if the angle was to be increased to 25°, maximum velocity would be approximately 1.9m/s. This is only an estimation, but indicated that the forces needed to be observed when a combination of high angles and high velocities were used. These calculations can be viewed in appendix B.

Forces in x- and y-direction were measured by a force transducer placed at the top of the foil (see figure 8.4). Velocities were controlled by the towing rig, and a wave probe was placed in the water close to the foil to measure the wave height. The immersed depth of the foil (h), could be modified by raising or lowering the foil manually in the towing rig. The yaw angle (α), could also be adjusted by rotating the foil relative to the towing carriage. This could be done before the run for a static angle towing, or during the run for testing dynamic angles. The angles were adjusted down to an accuracy of $\frac{1}{2}$ degrees. As an extra precaution, the rig had the option of locking the foil into its position, to minimize horizontal movements in the foil. The foil was locked during runs using static yaw angles, but remained unlocked when dynamic angles were tested.

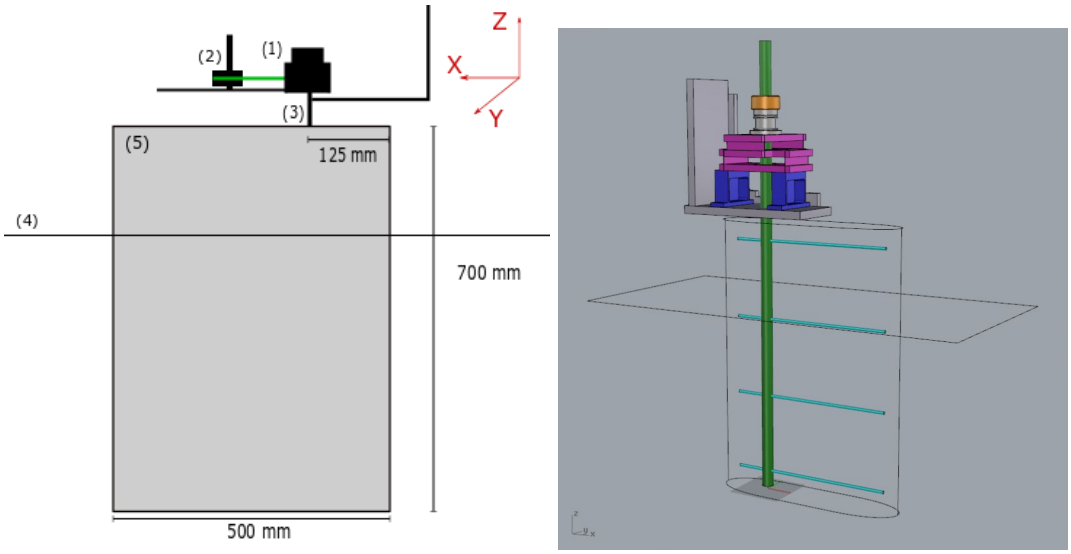

(a) Simplified drawing (b) CAD drawing of the foil set up.

Figure 8.3: Set-up in *Ottoriggen*, the figure contains the following (1) Force transducer, (2) Yaw angle adjustment, (3) Rod that attaches the foil to the rig, (4) Free surface, (5) Foil.

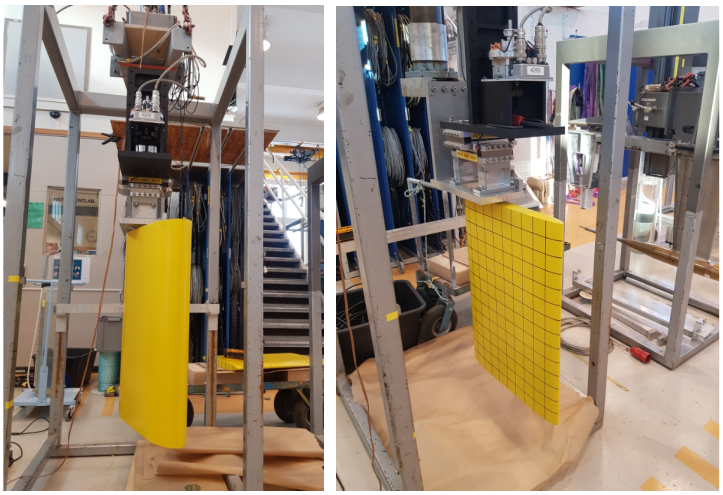

(a) Foil 1 (b) Foil 2

Figure 8.4: Both foil models placed in *Ottoriggen*

Two high speed cameras were fastened to the towing rig, positioned above the surface, astern the foil, vertically above each other. For the ventilation tests an underwater go-pro camera was placed above the surface, facing directly towards the suction side of the foil. This way the underwater flows could be visually observed. The exact positioning of the cameras were adjusted during the tests to ensure a good view of the waterline and the surrounding flows. To avoid VIV due to the underwater camera, two small foils were placed vertically below, attached to the same cylinder that held the camera. All sensors were calibrated by Sintef at their location.

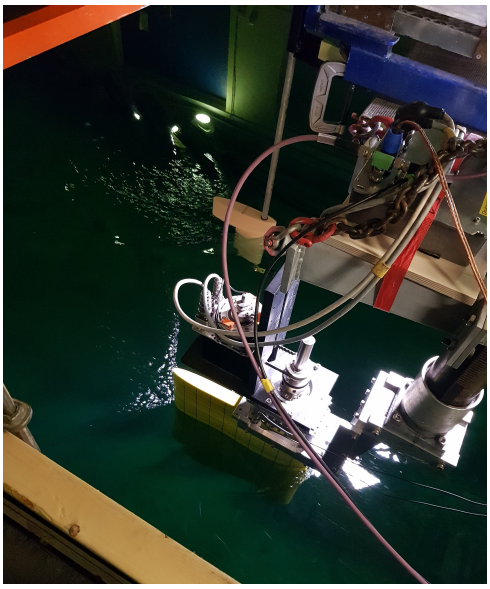

Figure 8.5: Foil 2 placed in the towing tank. The foils attached to the underwater camera can be seen at the opposite side of the surface-piercing foil.

8.4 Method

A complete run list of all conditions tested during the model towing tests are included in Appendix A. The experimental phase were mainly divided into two parts:

1. Measuring and investigating wave profiles on foil 1.
2. Obtaining and investigating ventilated flows on foil 2.

At the beginning of each day a test towing at 0° was run to stir up the water to establish similar water conditions for the following runs. There was a waiting period between each run, such that the generated waves could still down, but as the foil were run at low to moderate Froude numbers, long waiting periods did usually not occur.

8.4.1 Wave profiles

The data for wave profile related experiments conducted on foil 1, comes from the first 34 towings and can be viewed in appendix A, table A.4. The angles were adjusted with five degrees increments and the same angle were tested at both negative and positive y-axis. At the end the foil were also ran at ±2.5°. Summarized the angles ran on foil 1 were the following:

	Yaw angles										
[H]	-20°	-15°	-10°	-5°	-2.5°	0°	2.5°	5°	10°	15°	20°

The towing carriage was started at a velocity of 0.1m/s and the velocity was increased step wise every 10 seconds up to a maximum velocity of 1.25m/s, then the velocity was decreased in the same manner. Giving the following velocity development in figure 8.6

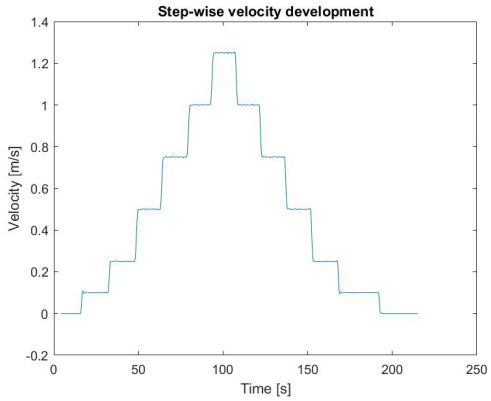

Figure 8.6: Step wise velocity development

8.4.2 Ventilation

Spontaneous stall induced ventilation (see section 7.4) was used to achieve ventilation for all runs in this section. This made it possible to achieve ventilation at moderate Froude numbers by increasing the yaw angle until the foil exceeded the stall angle and flow separation occurred. Different methods of velocity development were tested as well, and how static versus dynamic yaw angles would affect the flow around the foil. This way it is possible to observe and analyse how different parameters and transients affected ventilation, by looking at factors such as the point of inception and washout, as well as the size and development of the ventilated flow. In order to increase the Froude number, the immersed depth of the foil was reduced twice during the experiments. An overview over the different runs are summarized in table A.

Different conditions were used as a way of testing flows sensitivity to transient. Mainly three methods of towing the foil were tested and these are described below. As was discussed in the literature study, ventilation depends on the Froude number (Fn_h) and the angle of attack (α). By using different methods to reach the conditions needed for ventilation to occur, the effect of the transients and conditions can be investigated. Table 8.2, summarized what the constant and varying parameters for the different ventilation methods:

Table 8.2: Methods of velocity development

Method	Constants	Variables
Step-wise	a	α, V, h
Quasi steady	V, h	α, a
Dynamic angles	a	α, V, h

Step wise. Here, the velocity of the foil was accelerated and decelerated in step wise intervals. Same method as was used previously for foil 1 and the wave profile tests. The velocity development was as seen in figure 8.6. The velocity was increased every 10 seconds until it reached a set maximum velocity, then the towing rig decelerated at the same rate until full stop. For most of the runs the velocity was in the range V = 0.1-1.25 m/s. A few exceptions to this were made in the four last runs. Run 2205 and 3000 were run at V = 1.5-2.0 m/s, run 3001 at V = 1.0-2.0m/s and run 4027 were run at V = 0.86-2.57 m/s. A static angle of attack was set before each run. The angles were increased by 2.5 degrees for each adjustment from 0 to 20° on the negative y-axis. A few angles were tested from the positive y-axis for force comparisons.

Quasi-steady state. The foil was accelerated with a set acceleration from 0m/s to a maximum velocity and then decelerated back to 0m/s again. The angle was kept static throughout the run. To observe the effect acceleration had on the flows around the foil, the maximum velocity was kept at 2.0m/s through all these tests and the accelerations and yaw angles were the varying parameters.

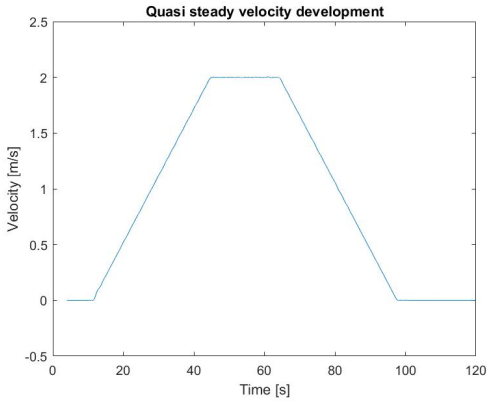

Figure 8.7: Quasi steady velocity development

Dynamic angles. The foil was accelerated from zero to a maximum velocity and then decelerated back again, as seen in figure 8.8b. During the run the angles were changed dynamically. Only angles in the range $1|5° - 22.5°|$ were tested here, as it had been confirmed from the previous runs that no ventilation occurred below 15° at the velocities used in this experiment. An example of how one angle were adjusted can be seen in figure 8.8a. One single run could test one or several angles, depending on the velocity and objective of the run. For the dynamic angles the foil was initially set to 0° and accelerated to maximum velocity. Approximately 10 seconds after reaching this velocity the hydrofoil was rotated to a set negative yaw angle and then rotated to the same angle at the positive y-axis. Each angle was kept steady for approximately 10 seconds. However, as the angles were changed manually from the rigs computers, the changing of the angles were not consistent for all runs. During these runs the acceleration was kept constant, while the Froude numbers and yaw angles were adjusted. The Froude number were adjusted both by varying the velocity and the immersed depth of the foil.

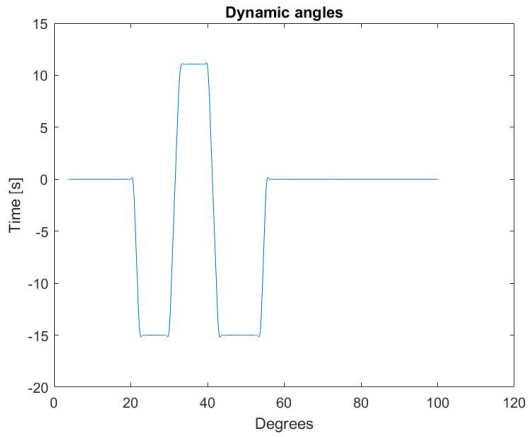

(a) Dynamic angles

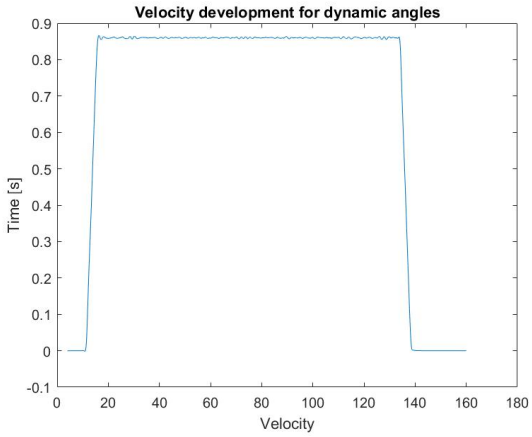

(b) Velocity development for dynamic angles

8.5 Post-Processing

A total of 100 sub conditions were tested and collected data for. This includes 34 runs using foil 1 and 66 runs using foil 2. All sub conditions are listed in Appendix A. All run numbers in the format 1xxx refers to towings done with foil 1, for wave profile investigations. While ventilation investigations done with foil 2 includes run numbers of the format 2xxx, 3xxx and 4xxx. The data collected includes video footage, force measurements in the x- and y-direction and wave elevation measurements. Both over water and underwater footage was recorded for all sub conditions using foil 2. This way the ventilated flow could be better visually assessed. While only the over water go-pro camera was used for foil 1 and the wave profiles.

The data collected from the force sensors were analysed in two ways. (1) The sub-conditions using step wise increments to accelerate and decelerate were imported to the software program ShipY and processed there. Further, the mean values could be extracted and exported to excel. Here, the data could be viewed and organized more easily. Finally, the data was plotted and visualized in Matlab. Non-dimensional values were also calculated here, such as the Froude number, Fn_h, and the force coefficient C_L and C_D. (2) The remaining conditions were processed using a catman-reader to read the .bin files and lowpass filter functions to filter the data. This was done in Matlab by functions provided by Sintef.

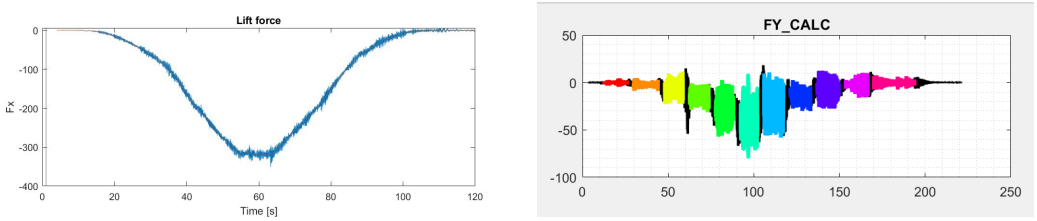

(a) F_y results using a lowpass filter on a quasi steady state in the catman-reader.

(b) Filtered F_y results on a step wise run from ShipY

Figure 8.9

The ventilated flows were investigated visually using the videography from the underwater camera to determine factors such as the time and velocity at inception and washout. From these data a ventilation matrix could be built. The point of inception in the different runs were set up against factors such as the depth based Froude number (Fn_h), acceleration (a) and angle of attack (α). This made it easier to draw conclusions on how the factors affected the flow.

Visual assessment were also used to compare ventilation areas for a set of sub conditions. Snapshots were taken at five second intervals from the point inception until washout for four different sub conditions. Additionally, the ventilation area at Fnh = 0.5, were compared for these runs. By using the grid pattern on the foil the area of the ventilated flow could be estimated by counting the squares, with an accuracy of $\pm\frac{1}{8}$ of a square. Each square measured 25 cm^2. The sub conditions and run numbers that were used for comparison are listed in table 11.1. Additionally, snap shots of the four conditions at equal depth Froude numbers were taken and compared.

Chapter 9

Numerical Set up

This chapter presents the method and set up of the numerical study conducted in the CFD software Fine/Marine. The results of these studies are later compared to the experimental results for validation of the CFD results.

To compare and validate the wave profiles, a total of 8 cases where simulated in Fine/Marine on the blunt foil (foil 1), which had a maximum thickness of 120mm. First, three cases at 0° were simulated. This was to run a convergence study to validate the meshing. For the remaining cases the angle of attack was increased by 2.5° for each run up to a yaw angle α = 12.5°

Table 9.1: Cases simulated in FineMarine

Yaw angle	0°	2.5°	5°	7.5°	10°	12.5°

A flow chart of the work progress in Fine/Marine is presented in figure 9.1. Further explanation of how the program functions can be found in section 4.6. The domain set up, mesh generation and general parameters are described in the following sections, the results from the post-processing are presented in chapter 11.

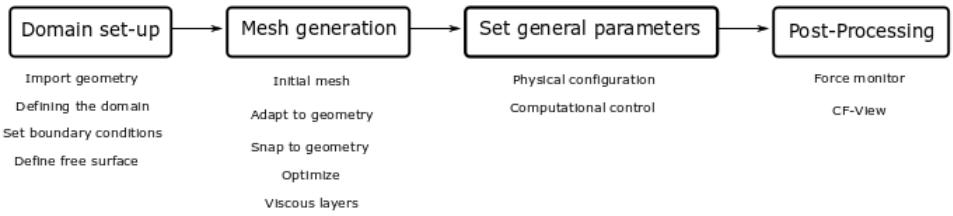

Figure 9.1: Flow chart for work progress in Fine/Marine

9.1 Domain set up

The geometry of the foil was based on the CAD drawings and could simply be called into Fine/-Marine as .x_t-files. As the program assumed a 3D body to be aligned along the x-axis, the alignment of the foil could not be adjusted in the interface and a new geometry-file had to be called for each case pertaining a different angle of attack. Meaning that an individual domain and mesh had to be made for each of these cases.

The initial domain had the dimension L_xxL_yxL_z = 12.5x7x4 [m]. The geometry and coordinate system can be seen in figure 9.2. The axis are defined as zero at the centre at the bottom of the foil at 25% from the leading edge, which is where the shaft attaching the foil to the towing rig were placed. See figure 9.2. For the domain, the length in y- and z-direction was kept constant in all cases, but the domain size in the y-direction was increased to accommodate for larger yaw

angles. For each increased angle, the width was adjusted by a ratio equal to the distance in the y-direction between the bounding box in the zero-degree case and the inclined cases. Where a bounding box is defined as an imaginary box that exactly outlines the outer of the foil. For the zero degree case this gives an 0.5x0.12x0.7 [m] cubic. The width of the bounding box for the inclined cases was found as $Y_B = 0.12 + 0.5 \tan \alpha$, and the ratio, $R = Y_B/0.12$. Where 0.12 is the width of the bounding box at zero degrees and 0.5 is the length, both given in meters. The ratios and the length of the domain in the y-direction, L_y, for each case are summarized in table 9.2.

The free surface is represented by the interface between the two fluids; water and air. For accurate representations of the wave profiles in this area, an internal surface was created at the location of the still free surface, at Z= 0.47m.

Table 9.2: Increased width of the domain

α [Deg.]	Y_B [m]	R	L_y [m]
0	0.12	1	7
2.5	0.142	1.18	8.27
5	0.164	1.36	9.55
7.5	0.186	1.55	10.84
10	0.208	1.73	12.14
12.5	0.231	1.92	13.47

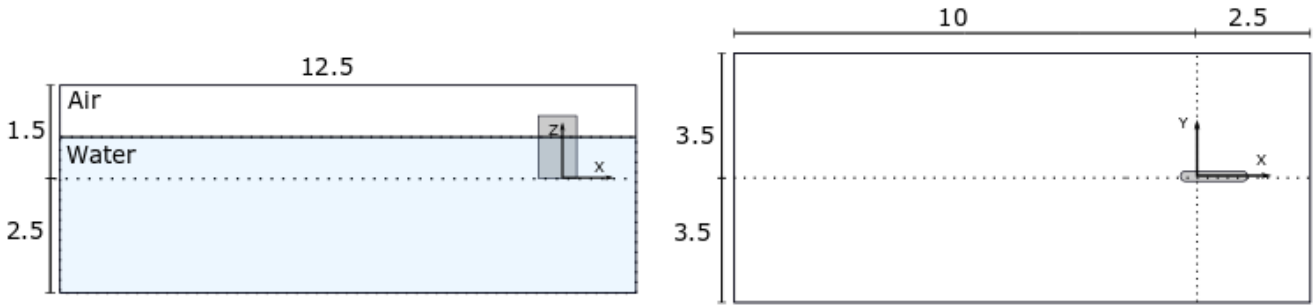

Figure 9.2: Domain used for numerical simulations. All values are given in meters.

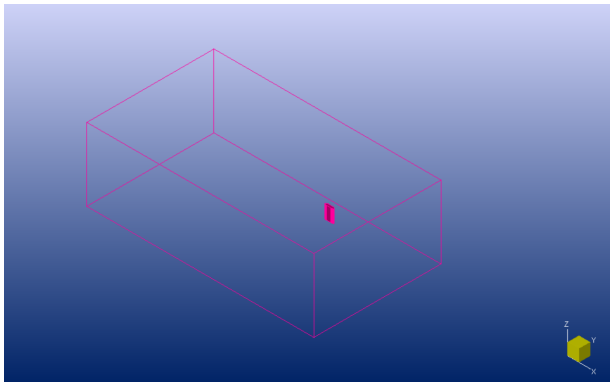

Figure 9.3: Domain set up for a zero degree yaw angle case.

9.2 Mesh generation

As a new domain was made to accommodate the increasing angles for each geometry-file, a new mesh had to be generated for each case as well. To avoid large aspect ratios for the grid cells in x- and y-direction, the initial mesh along the y-axis had to be increased accordingly. The number of initial cells in each direction are listed in table 9.3. The initial mesh for the zero-degree case was validated through a mesh study presented later in section 9.4.

Table 9.3: Initial mesh

Initial mesh			
Yaw angle [Deg.]	X	Y	Z
0°	23	13	7
2.5°	23	13	7
5°	23	16	7
7.5°	23	18	7
10°	23	19	7
12.5°	23	22	7

To better capture the free surface flow surrounding the foil, especially the bow wave and the wake, three mesh refinement boxes were placed around the foil. This assured further refinement in the areas of interest. See figure 9.4 and table 9.4, for visualization and coordinates. For a smooth transition, the mesh diffusion was set as 4.

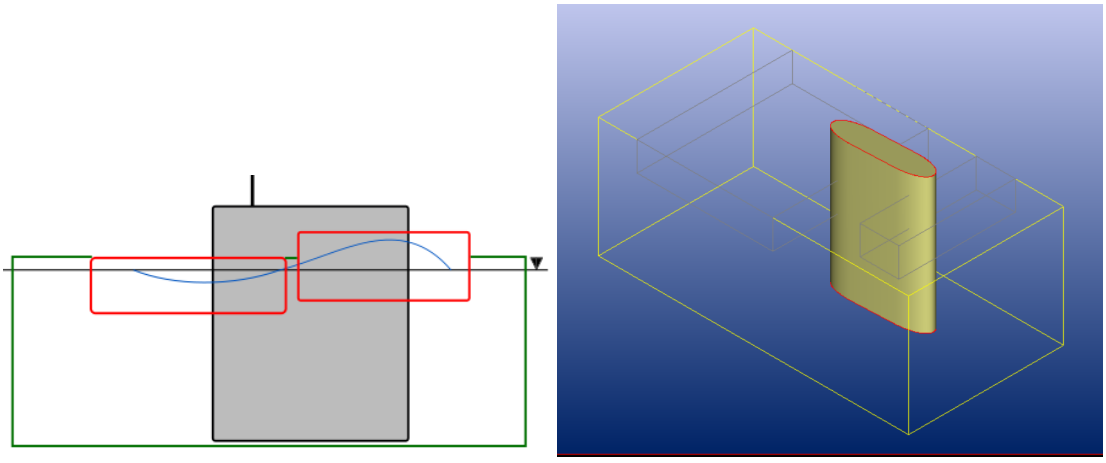

Figure 9.4: Mesh refinement boxes used to refine the cells in the area where the surface of the bow wave and wake is predicted to be.

Table 9.4: Corner coordinates for the mesh refinement boxes

X	Y	Z
0.05	-0.3	0.45
0.25	0.3	0.6

(a) Bow wave box

X	Y	Z
-1.0	-0.4	0.35
-0.3	0.4	0.5

(b) Wake box

X	Y	Z
-1.2	0.4	0.5
0.4	-0.4	-0.12

(c) Foil box

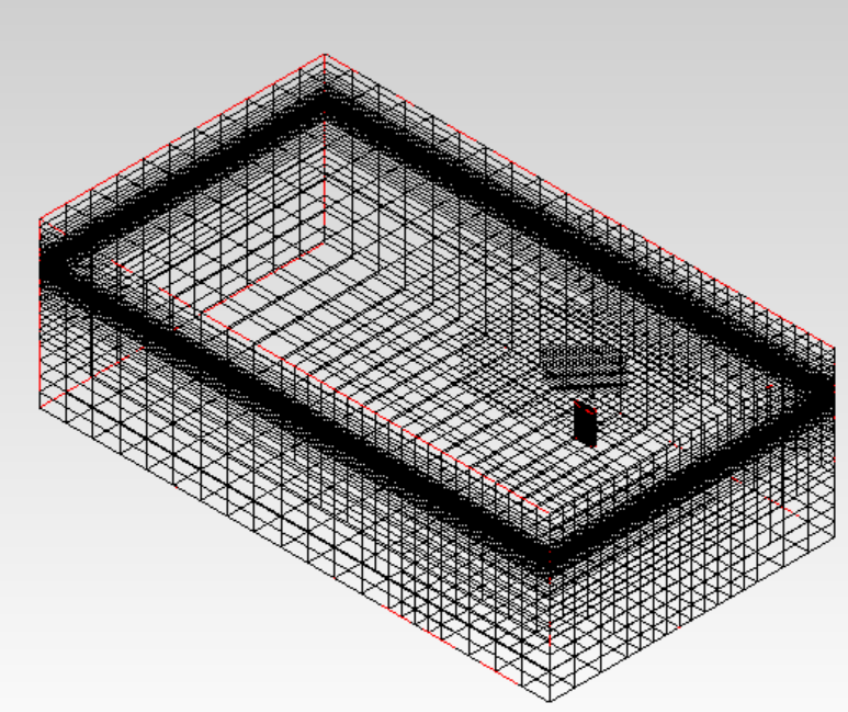

Figure 9.5: Generated mesh in Fine/Marine.

9.3 General parameters

The general parameters of the case are set in the Fine/Marine interface. The model was defined as a multi-fluid case and the domain was accelerated from 0 to 1m/s using an unsteady time configuration. Boundary conditions for the walls and bottom of the foil were set as wall-function, while the top plate, which is at all times above the free surface, were set as slip (zero shear stress). The external boundaries in the z-direction used hydrostatic pressure, while the other domain walls were defined by far field conditions. As the angles were static for all simulations, only motions in the surge direction were allowed. Table 9.5, summarizes some of the other general parameters used for the simulations. Note that steady time configuration was used first, but case 3 was run a second time for an unsteady configuration to improve the drag force results.

Table 9.5: General parameters

Physical configuration		
Time configuration	Unsteady	
Turbulence model	$k-\omega$ (SST-Menter)	
Reference length	0.5	m
Reference velocity	1.0	m/s
Motion law	1/4 sinusoidal ramp	
Acceleration time	2	s
Interface position, z	0.47	m
Computational control		
Number of time steps	6000	
Time step value	0.005	s

9.4 Mesh Study

To validate the meshing, a mesh study was conducted on foil 1 for all three cases with zero degree yaw angle. The domain was set up as described previously, but with a steady time configuration. Three simulations were run with different initial mesh sizes. The number of initial cells in the x-, y- and z-plane is listed in table 9.6.

As validation for the CFD simulations the following steps were taken:

- The average force and force history of the three cases were compared to each other.
- Wave profiles from the CFD simulations were compared to each other.
- The forces and waveprofiles were compared to experimental values.

Simulations were run for three cases with different initial cell sizes, to draw conclusions on the accuracy of the results. The first case used the recommended cell sizes provided by Fine/Marine. Per recommendations from a supervisor, the number of initial cells were increased by a factor of $\sqrt{2}$. For the last simulation the values midway between the first two cases were used. All values were approximated to the closest integer. The number of initial cells for each case is listed in table 9.6.

Table 9.6: Initial mesh in the x-, y- and z-plane for the mesh refinement study.

	Nr. of initial cells		
Case	X	Y	Z
1	16	9	5
2	19	11	6
3	23	13	7

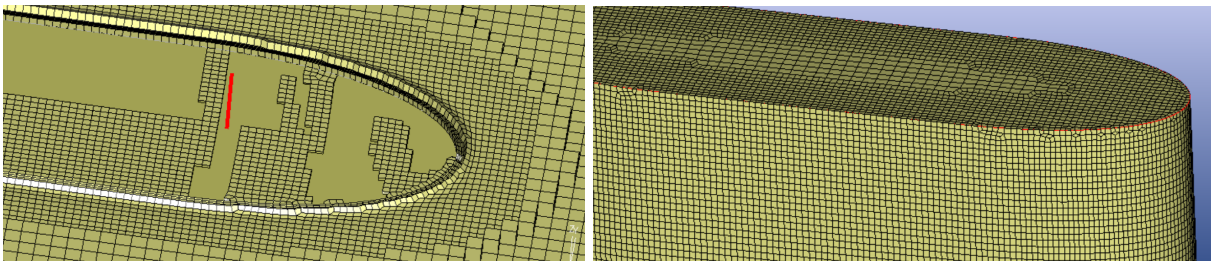

(a) Mesh at still free surface, Z=0.47m (b) Mesh around the surface of the foil

Figure 9.6: Close up of the mesh refinement in case 3.

As the mesh study was conducted on a zero- degree case where the lifting forces should go towards zero, the convergence of the forces were only investigated for the drag forces, F_x. As seen from figure 9.7, the drag forces are converging towards a similar value for all three cases.

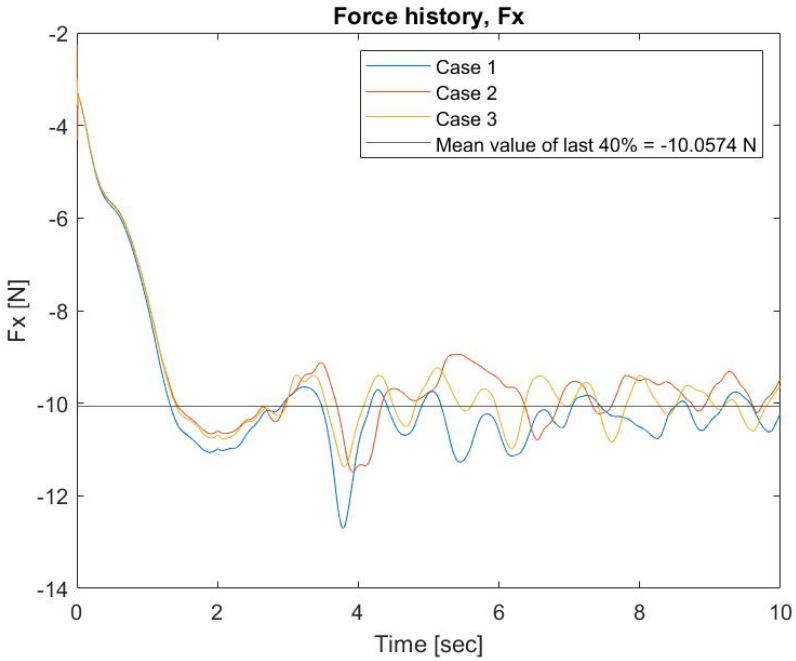

Figure 9.7: Force history of the drag force (Fx) in each simulation case. The forces can be observed converging as the time passes.

The wave profiles could be inspected visually in CFview, by looking at the mass fraction between the two fluid present in the simulation. The interface between these fluids represents the wave profile along the surface of the hydrofoil. Figure 9.8, shows the waterline along the foil of each case from coarsest to finest mesh. Blurring can be seen along the sides, but the height of both the bow wave and stern wave are approximately the same for all cases.

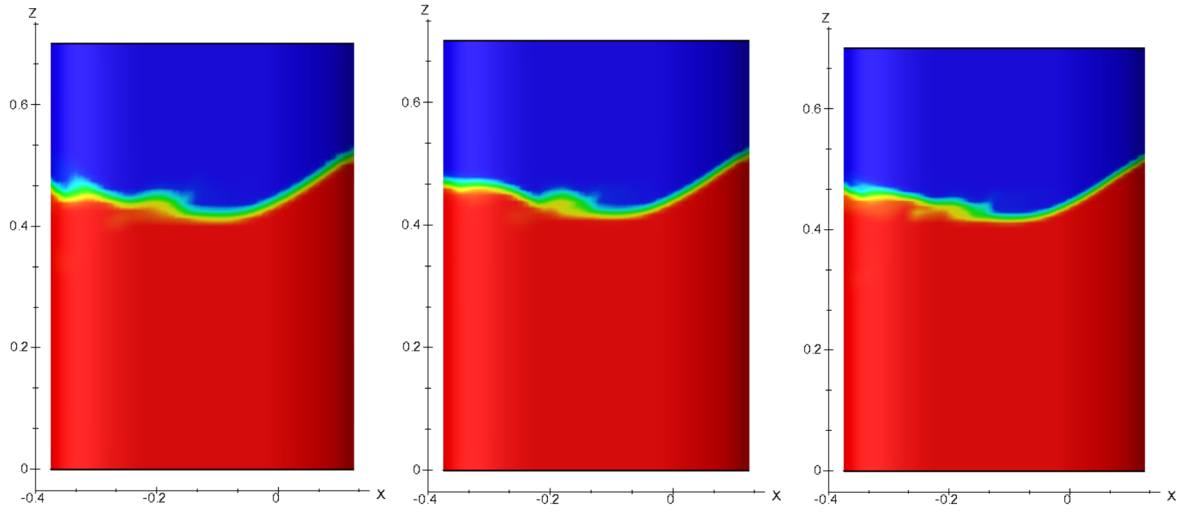

Figure 9.8: Comparison of the wave profiles generated in Fine/Marine for a foil with a velocity of 1m/s and a zero degree yaw angle. The figures show respectively case 1, case 2 and case 3. Meaning that the foil with the coarsest mesh is located to the left and the finest mesh to the right.

The numerical wave profile can also be qualitatively compared to the videography of experimental wave profile.

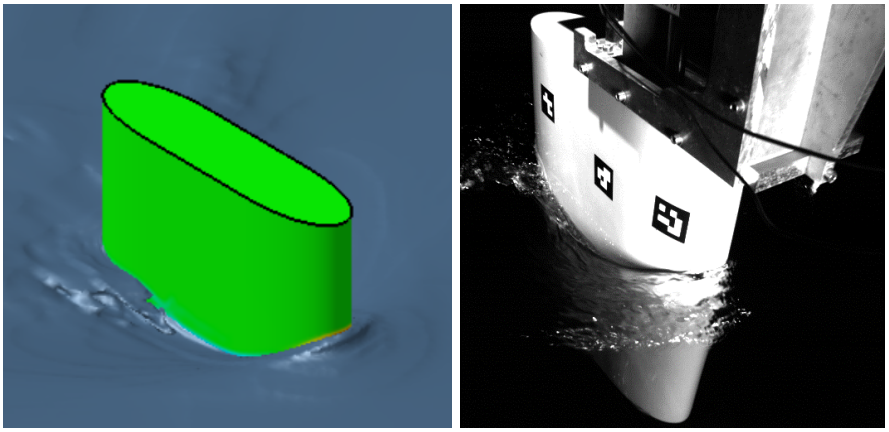

(a) (b)

Figure 9.9: Numerical and experimental waveprofile at $\alpha = 0^\circ$

The absolute mean values of the experimental and numerical drag force are listed in table 9.7, the relative error is calculated as shown in equation (9.4.1). The values are given absolute values, as the coordinate system in the numerical and experimental setting have opposite direction for the x-axis. The experimental value is the mean value gathered from run 1000-1005 where foil 2 were towed at 0° angle of attack.

$$\epsilon_{rel,k} = \left| \frac{F^{k-1}_{x,mean} - F^{k}_{x,mean}}{F^{k-1}_{x,mean}} \right| \cdot 100 \qquad [\%]+ \tag{9.4.1}$$

Table 9.7: Comparison of the absolute mean values for the numerical and experimental drag force (F_x) at 0° and V = 1.0m/s

	Experimental	Case 1	Case 2	Case 3 (steady)	Case 3 (unsteady)
F_x [N]	8.43	10.37	10.02	9.82	9.20
e_{rel}			3.40%	1.92%	

The relative error estimated from the numerical cases are 1.92% for case 3, which is the finest mesh. This is well below the common tolerance level of 5% and can therefore be deemed acceptable compared to the other mesh cases. However, the relative error between case 3 and the experimental value was found to be e_{rel} = 14%. By adjusting the time configuration to unsteady, the drag force was reduced to F_x = 9.2N, which gave results that aligned better to the experimental values and a relative error of 8.4%.

Since there was a discrepancy in the experimental and numerical results, the Y+ values were checked to see if the mesh size was small enough to model the near wall viscous layers. When using the $k-\omega$ - turbulence model, a maximum Y+ value below 300, indicates that the mesh is sufficiently small to be able to model the boundary layers correctly. As seen from figure 9.10, the Y+ values for case 3 are in an acceptable range.

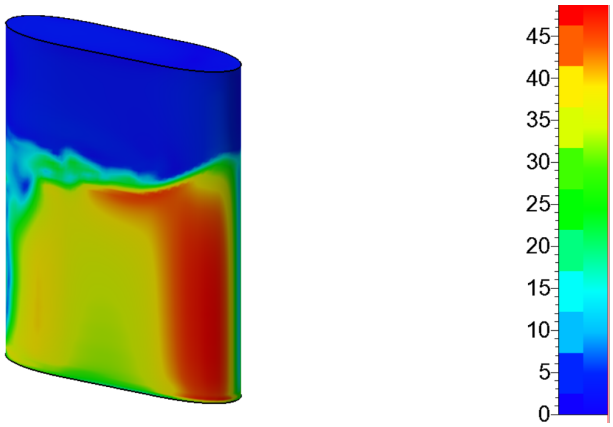

Figure 9.10: Y+ values for case 2.

The lift forces were also checked and found to be approximately zero for all cases, as a symmetrical foil with no angle of attack should not produce lift. As all other factors seemed appropriate for the case, it was decided to continue with the mesh from case 3, despite a slightly larger F_y than the experimental results.

Chapter 10

Uncertainty analysis

The results of physical experiments will always have an element of uncertainty in them. These errors are commonly divided into *bias error* and *precision error*. Where precision error are inherent uncertainties that are associated with the the measurements, as there will always be a certain "scatter" in measurements. Bias error are systematic errors that cannot be found through repetitions. (Steen, 2014).

To know how reliable the results gained from an experimental method is, an analysis should be carried out in order to determine the level on uncertainty and if any outlier results should be rejected from the results. Due to time limitations, only a few repetition runs were run, this chapter summarizes the precision error on one case which was repeated a total of six times.

10.1 Precision error

The precision error was calculated from six measurements made on the blunt foil at an angle of attack, $\alpha = 5°$ for the forces in drag and lift. These are summarized in table 10.1 The forces used are the mean measurements taken at the maximum velocity, V = 1.25m/s. A Gaussian distribution with a 95% confidence interval was assumed, the method followed is as given by Coleman and Steele (2009).

Table 10.1: Repeated tests. Mean lift and drag force at $\alpha = 5°$ taken at the maximum velocity, V =1.25m/s.

Run nr.	F_y [N]	F_y [N] [N]
1010	39.9431	26.8579
1011	41.1434	26.5929
1012	40.3305	26.8940
1013	39.0227	26.7879
1014	39.4171	26.9173
1015	44.6920	28.0094

The mean value, $\bar{X}$ is given for N number of samples as:

$$\bar{X} = \frac{\sum_{j=1}^{N} X}{N} \tag{10.1.1}$$

Standard deviation S_x and the standard deviation of the mean, $S_{\bar{X}}$ are as following:

$$S_X = \sqrt{\frac{1}{N-1}\sum_{j=1}^{N}(X_j - \bar{X})^2}, \tag{10.1.2}$$

$$S_{\bar{X}} = \frac{S_X}{\sqrt{N}} \tag{10.1.3}$$

Precision limit, P_x for a sample and the mean precision limit, $P_{\bar{x}}$:

$$P_x = t_s S_x \tag{10.1.4}$$

$$P_{\bar{x}} = t_s \frac{S_x}{\sqrt{N}} \tag{10.1.5}$$

Where t_s is the weight for estimating confidence intervals using student's t-distribution. The value of t_s was wound from a built in Excel-function.

Using these values, the uncertainty of a single force measurement can found to be:

$$e_x = \frac{P_x}{\bar{X}} \tag{10.1.6}$$

And the uncertainty of the mean, $e_{\bar{X}}$ as:

$$e_{\bar{X}} = \frac{P_{\bar{X}}}{\bar{X}} \tag{10.1.7}$$

It is observed from table 10.1 that run 1015 has a considerably larger F_y force. For a small sample number this can have significant influence on the uncertainty. Chauvenet's criterion for rejecting outliers was therefore considered for all the data tested (Limb et al., 2017):

$$\left|X_j - \bar{X}\right| > t_c \cdot S_x \tag{10.1.8}$$

Where t_c is specified from the number of samples. For N = 6, $t_c = 1.73$. From table 10.2, it can be seen that the deviation from the mean is large enough to reject the run.

Table 10.2: Chauvenet's criterions

	$\left\|X_j - \bar{X}\right\|$	$t_{chauvenet} \cdot S_x$
$F_{y,1015}$	3.93	3.56
$F_{x,1015}$	1.00	0.91

The results from run 1015 is therefore considered an outlier and excluded from further analyses. This gives the following uncertainty results:

Table 10.3: Results from the uncertainty analysis of the model resistance with six measurements at V = 1.25m/s. This corresponds to $Fn_h = 0.582$

Quantity	F_Y	F_x	Unit
$\bar{X}$	39.9714	26.8010	N
S_X	1.0776	0.2590	N
$S_{\bar{X}}$	0.4819	0.1158	N
t	2.7764	2.7764	-
P_X	2.9918	0.7190	N
$P_{\bar{X}}$	1.3380	0.3216	N
e_X	7.49	2.68	%
$e_{\bar{X}}$	3.35	1.20	%

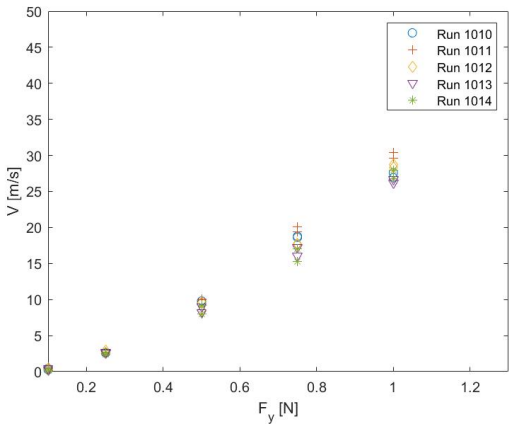

(a) Lift force, F_y

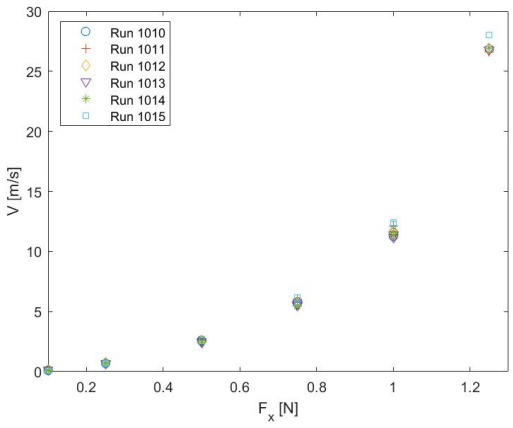

(b) Drag force, F_x

Figure 10.1: The force data for each run at $\alpha = 5°$, showing the scatter of the measured results.

10.2 Bias errors

The bias errors are not very quantifiable, as it is difficult to obtain specific information on them. Some sources of bias errors in the experimental phase are listed here:

- Wall tank effects may have had an affect on the flow around the foil. This includes wave reflections from the end of the tank, and to a lesser extent from the sides.
- Still water levels were assumed to be the same at every run. There was a break period between each run, but there might still have been smaller variations in the immersed depth of the foil.
- Geometry of the rig. Factors such as symmetry could have affected the accuracy of the angle and force measurements.
- The foil was observed to be vibrating in yaw and this would have had an affect on the accuracy of the angles. It was especially noticeable in high yaw angles when the forces were larger.
- Only qualitative visual comparisons were made of the wave profiles.

- The foil struggled to reach high angles of attack at high velocities, when the angles were adjusted dynamically.
- Other factors such as the calibration and small inaccuracies in the geometries of the foils are also possible sources of bias error.

Chapter 11

Results and Discussion

In this chapter the results of this thesis is presented and discussed for both the experimental and numerical study. The experimental results are divided into one section for the wave profile investigation conducted on the blunt foil, and a following section for the result obtained from the ventilation investigation on the slender foil. The next section pertains the results from the numerical study conducted on the blunt foil. The final section compares the numerical and experimental studies on free wave generation.

The majority of the results are given in absolute values here, as the coordinate systems for the experimental and numerical set up are defined differently. The positive direction of the x- and y-axis are defined in the opposite direction. The numerical x-axis is positive in the foils direction of motion, while the experimental x-axis is positive in the opposite direction. See figure 11.1, where the axis are illustrated. The angles are given as absolute values unless otherwise stated.

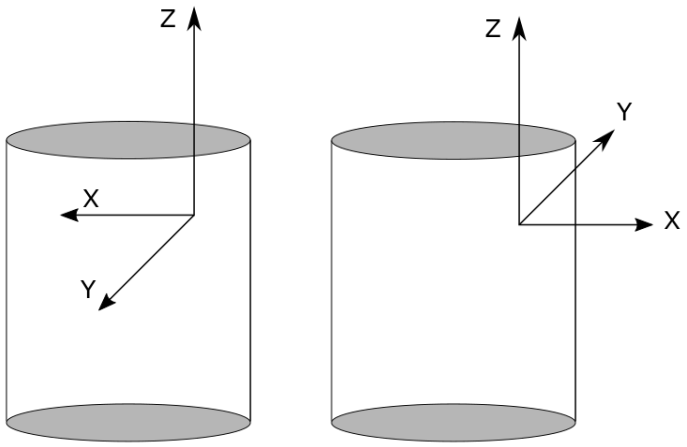

(a) Experimental (b) Numerical

Figure 11.1: Coordinate systems

11.1 Experimental Results

The following section presents the main findings from the experimental study. First the results from the wave profile investigation on foil 1, the blunt foil, is presented. Afterwards, the results from the ventilation investigation on foil 2, the slender foil, can be found.

11.1.1 Experimental results from Wave profile Investigations

Hydrodynamic forces

The following figures shows the mean values extracted from ShipY and then plotted in Matlab. Each figure represents the hydrodynamic coefficients, C_L and C_D, as a function of the Froude number at one yaw angle. The figures contains the data from each run conducted at that angle of attack at both positive and negative y-axis.

Theoretically, the absolute hydrodynamic forces for a symmetric foil should give the exact same result when measured at the same angle at opposite sides of the y-axis. However, as can be observed from the drag coefficients in figure 11.2 - 11.6, there is a disparity between the drag coefficients that becomes more apparent as the yaw angle increases. This likely stems from a bias error, possibly from a small imperfection in the foil model or the symmetry of the set up and towing rig which could lead to the angle measured not being equal to the true angle in the tank.

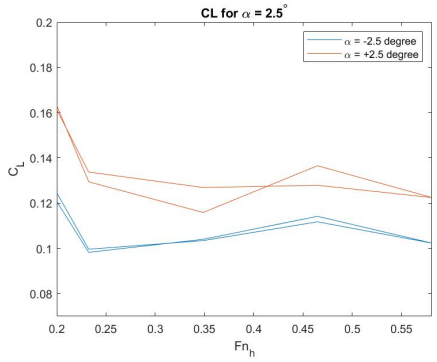

(a) C_L at $\alpha = 2.5°$

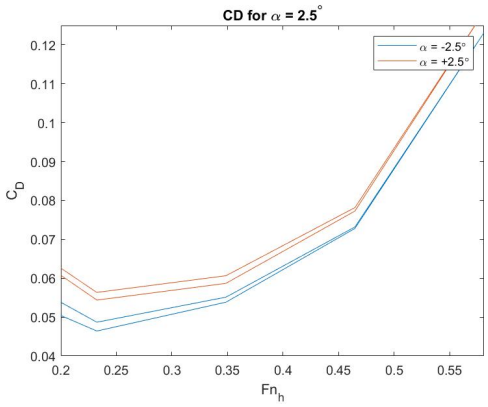

(b) C_D at $\alpha = 2.5°$

Figure 11.2: Lift and drag coeffcients at ±2.5° yaw angle. Lift is given as absolute values.

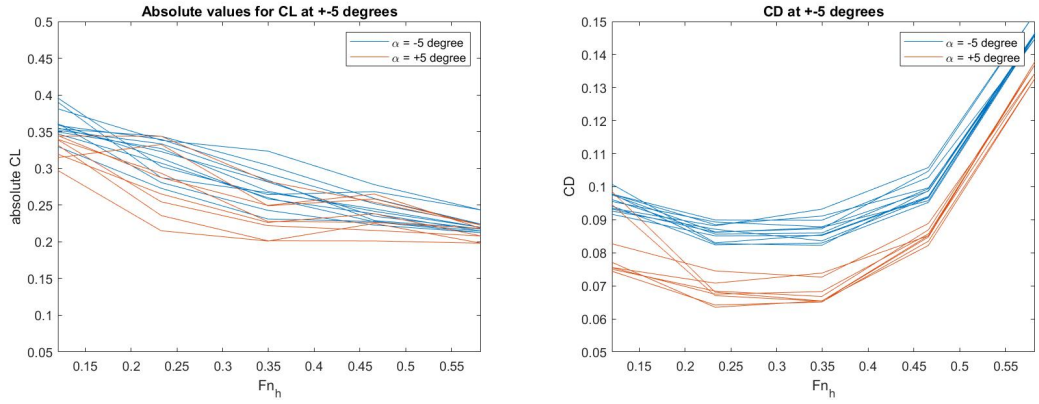

(a) C_L at $\alpha = 5°$ (b) C_D at $\alpha = 5°$

Figure 11.3: Lift and drag coefficients at ±5° yaw angle. Lift is given as absolute values.

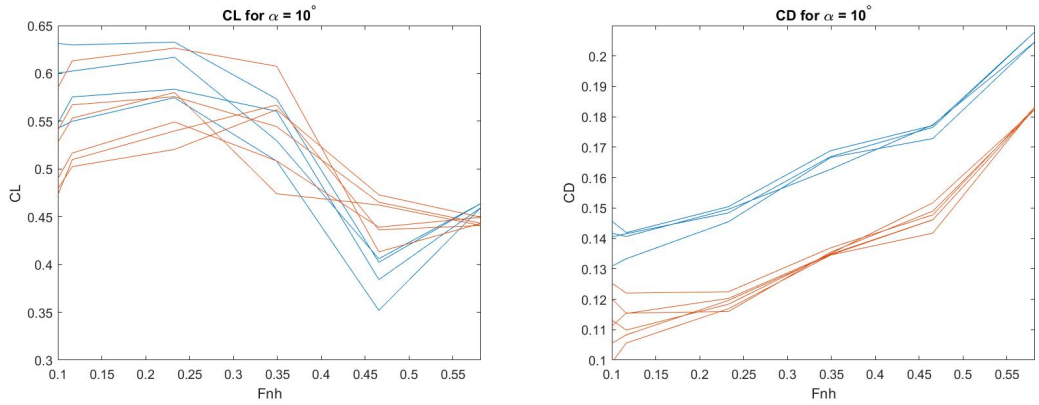

(a) C_L at $\alpha = 10°$ (b) C_D at $\alpha = 10°$

Figure 11.4: Lift and drag coefficient at ±10° yaw angle. Lift is given as absolute values.

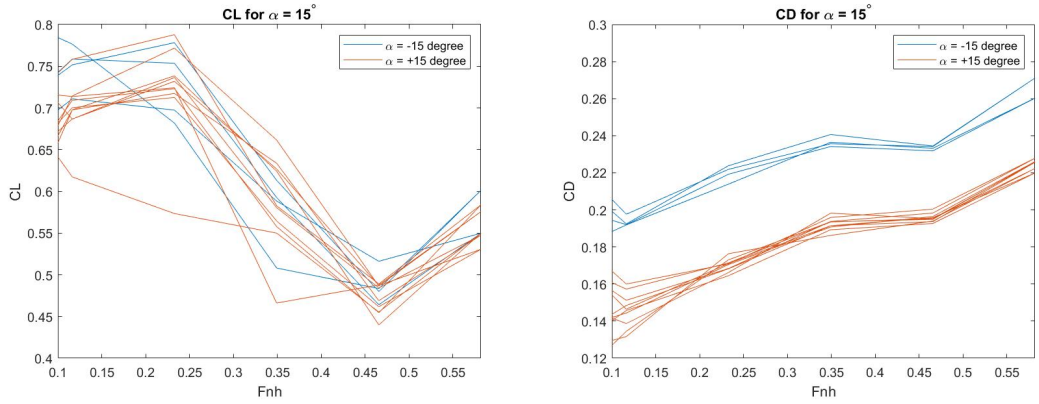

(a) C_L at $\alpha = 15°$ (b) C_D at $\alpha = 15°$

Figure 11.5: Lift and drag coefficients at ±15° yaw angle. Lift is given as absolute values.

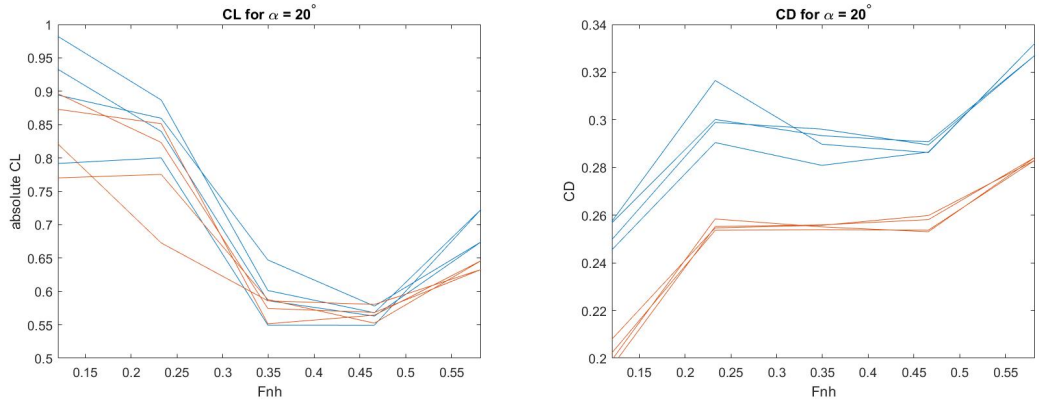

(a) C_L at $\alpha = 20°$ (b) C_D at $\alpha = 20°$

Figure 11.6: Non dimensional lift and drag coefficient at ±20° yaw angle. Lift is given as absolute values for comparison.

Wave profiles

The wave profiles were filmed using high speed go-pro cameras attached to the towing ring. The original plan was to capture the wave profiles at the same Froude number as the CFD simulations by using the method described in chapter 6. However, there were difficulties detecting the contrast between the waterline and solid foil at the moderately high Froude numbers. Within the time limitation, the wave profile could only be investigated qualitatively, by comparing them to the videography footage. Presented are a selection of the wave profiles on foil 1, as seen from the high speed cameras.

As foil 1 was run at both positive and negative yaw angle, it gives a good view of both the low pressure suction side and the high pressure side. Figure 11.7, shows two runs with a 15° yaw angle, on both positive and negative y-axis. Here, the suction side can be seen in figure 11.7a, where a flow separation from the leading edge can be observed is observed. Figure 11.7b.

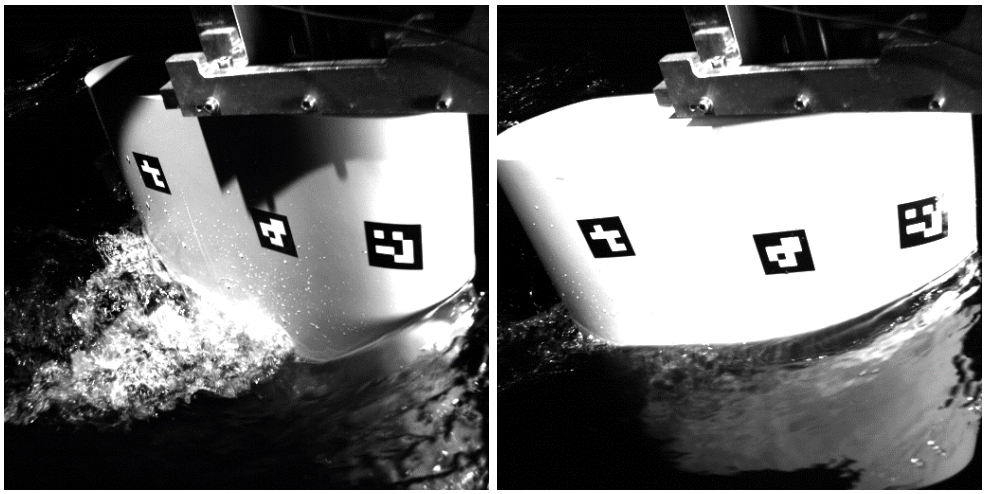

(a) Suction side (b) Pressure side

Figure 11.7: Wave profiles at $\alpha = \pm 15°$, V = 1.25m/s and $Fn_h = 0.582$.

The wave breaking criteria is defined as:

$$Fn_h(\alpha_E) = \frac{4.4 \tan \alpha_E}{\cos \alpha_E} - 1 \quad \text{if} \quad \alpha_E \geq \alpha_E^B \tag{11.1.1}$$

Where α_E is half the waterline entrance angle of the foil, and α_E^B is the critical waterline entrance angle. Which is defined as $\alpha_E^B \approx 12.5°$. Since the angle of the blunt foil exceeds this with $\alpha_E \approx 30°$, it should produce unsteady waves as long as the Froude number stay below the critical limit, $Fn_h \approx 2$. As the blunt foil was only tested for Froude numbers below $Fn_h = 0.581$, it should produce unsteady waves in all cases. This can observed in figure 11.8, where a foil with zero-degree yaw angle can be seen producing an unsteady bow wave. A Kelvin wave pattern can also be seen generating from the sides of the foil in figure 11.8a.

The difference between the wave profiles on the inclined foil can be seen in figure 11.7. At the pressure side in figure 11.7b, a overturning wave creating a thin sheet of water past the bow can be seen. While at the suction side, a great deal of turbulence and non-linearities can be viewed behind the separation point. Comparatively, the slender foil has a waterline entrance angle below the breaking bow wave criteria, with $\alpha_E \approx 11.5$ and should therefore produce a steady overturning wave for all Froude numbers. The difference can be seen in figure 11.9, were pictures of the slender foil is included. The slender foil generates steady waves with very little perturbations outside the wake.

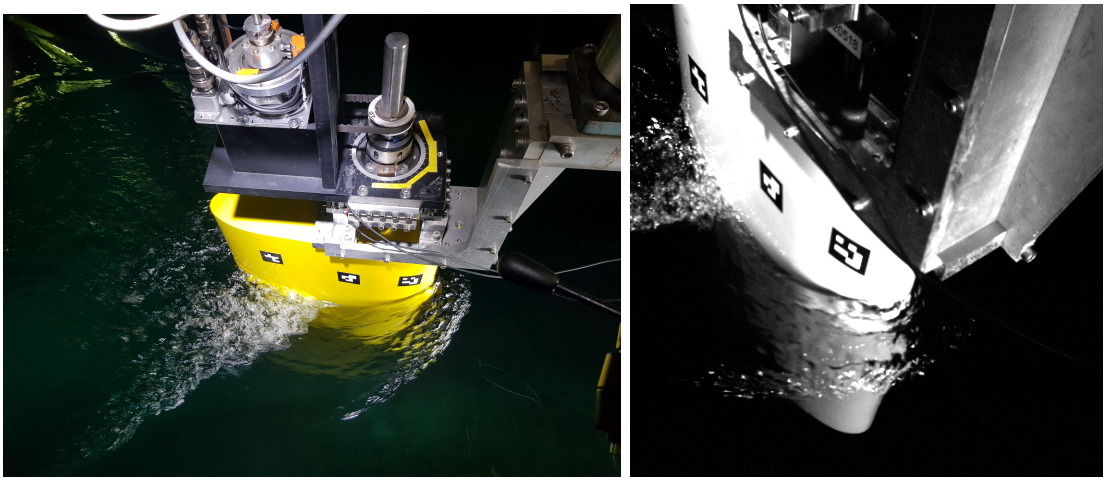

(a) (b)

Figure 11.8: Unsteady bow wave at a zero-degree angle

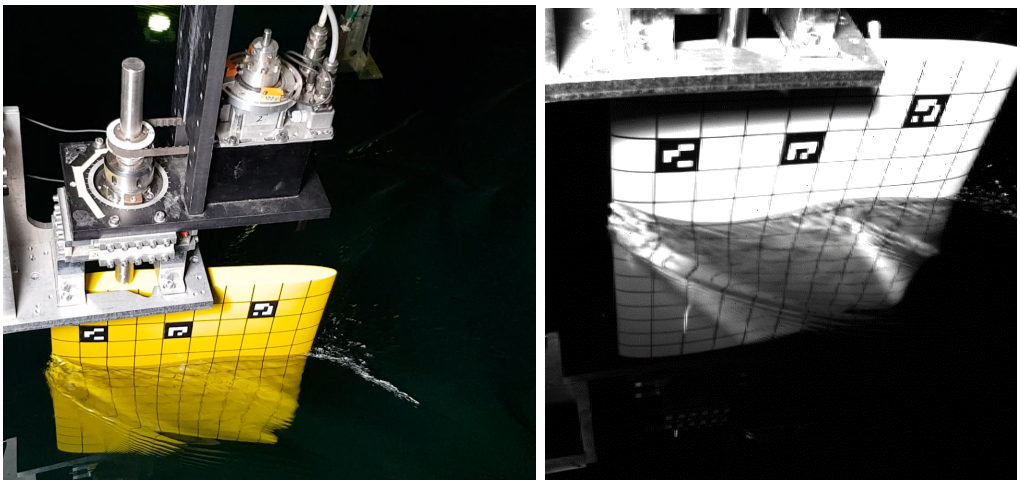

(a) (b)

Figure 11.9: Steady bow wave at a zero-degree angle

11.1.2 Experimental results from Ventilation investigations

Ventilated flows were achieved through spontaneous stall-induced ventilation, where the angle of attack were increased past the stall angle. This causes a flow separation and a stable air channel develops from the free surface and down to the foils suction side. In figure 11.11, the three flow regimes are seen. They can be compared to the illustration in 11.10 which shows the ventilation formation process due to a stall induced ventilation. Figure 11.11a, shows a slightly deformed free surface, but no air bubbles - a fully wetted flow. In figure 11.11b a stable air channel has formed after a flow separation near the leading edge. The aerated bubble expanded quickly, covering a large section of the suction side. The free surface is heavily deformed. The entire span of the foil is not covered yet and the flow is therefore defined as partially ventilated. The fully developed ventilated flow is shown in figure 11.11c, the ventilation bubble can be seen to cover the entire span of the foil, and the angle between the cavity closure line and the bottom of the foil is below the criteria for ventilation, $\Phi \leq 45°$. The air channel and cavity closure is visibly smoother.

The ventilation bubble can be seen from above in figure 11.12. Here, the air pocket is clearly visible and covered by a thin layer of water. A spray of fluids is pushed up from underneath the cavity, creating a highly turbulent wake.

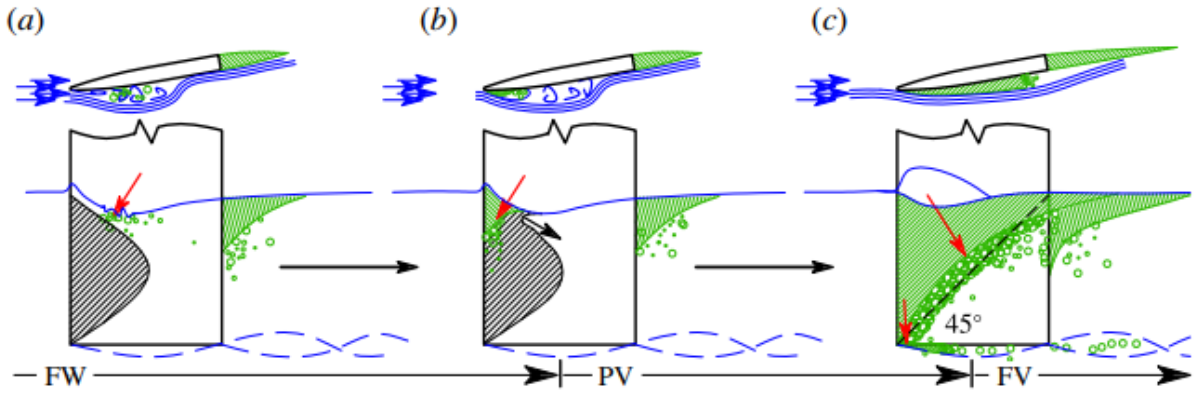

Figure 11.10: Ventilation formation from FW to FV flow by a spontaneous stall-induced ventilation. Black hatches shows boundary layer separation, blue lines are streamlines, green hatchings shows areas of air entrapment and the red arrows indicates the paths of air entering. Reprinted with permission from Harwood et al. (2016, Fig. (18))

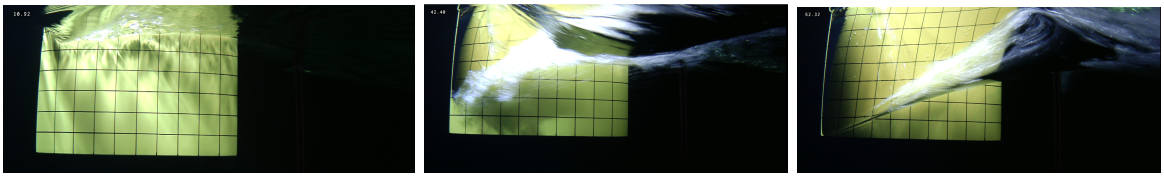

(a) Fully wetted flow (b) Partially ventilated flow (c) Fully ventilated flow

Figure 11.11: The three flow regimes as seen from the underwater camera. All photos are from run 4027.

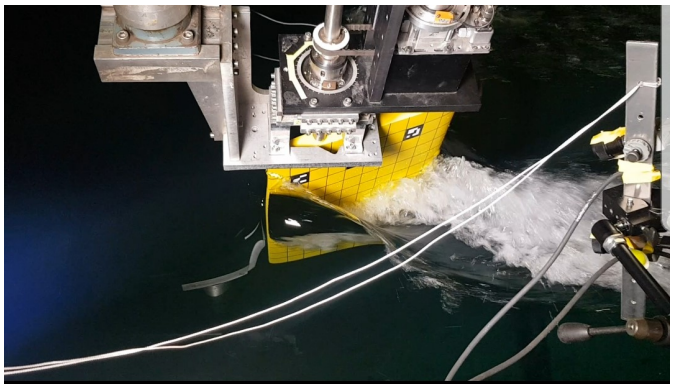

Figure 11.12: The ventilated flow as seen from above.

Step wise ventilation

For these tests, the towing rig was accelerated in a step wise manner until a maximum velocity was reached and then decelerated at the same rate. For the majority of the tests, the foil stayed in the velocity range 0.1-1.25m/s ($Fn_h = 0.047 - 0.582$) . Figure 11.13, maps the flow regions as a function of yaw angle (α) and Froude number (Fn_h). In the white regions the flows remained fully wetted. Light green marks partial ventilation, and the flow was fully ventilated in the dark green area. The stall angle was observed to be at $\alpha = 15°$ and functioned as a lower boundary for ventilated flow to occur. The lower Froude limit for ventilation was found to be $Fn_h = 0.349$. Above these boundaries, inception occurred and the flow entered partial ventilation. A few runs were tested for higher velocity ranges as well. A fully ventilated flow was only achieved once, when the Froude number was increased to Fnh = 1.197 at $\alpha = 20°$. It was also observed that no ventilation occurred at $\alpha = 15°$, when the initial velocity was increased and the velocity range was changed to 1.5-2.0m/s. Ventilation still occurred at $\alpha = 15°$ for V = 1.0-2.0m/s. It also developed when $\alpha = 20°$ at V =1.5-2.0m/s. Indicating that the ventilated flow develops more easily when the foil is accelerated from lower velocities and that a higher yaw angle is needed when the velocities has a higher starting point.

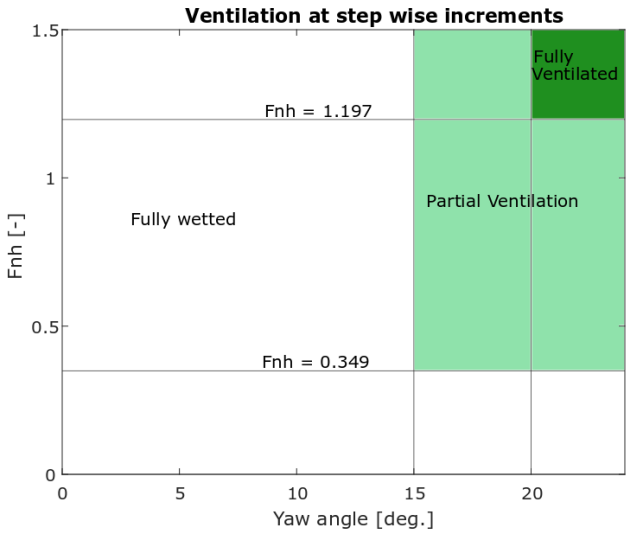

Figure 11.13: *Flow regimes - Step wise velocity* Mapping of flow regimes as a function of depth based Froude number (Fn_h) and yaw angles (α). The foil was accelerated in step wise increments as shown in figure 8.6. White areas represents fully wetted flow, light green show partially ventilated flow and fully ventilated flow are represented by deep green.

The hysteresis effect on the flow was investigated by registering the points of inception and washout for a selection of the ventilated runs. In figure 11.14, these points are plotted as a function of the yaw angle and Froude number. Here, one can see that the inception occurred at higher Froude numbers during acceleration. In a decelerating flow hysteresis influenced the flow and the ventilation remained for up to 60% lower values of Froude numbers than during acceleration. This effect did however lower as the angle of attack increases.

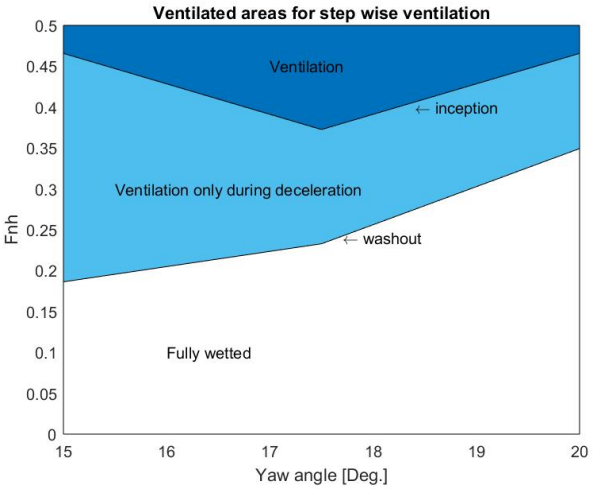

Figure 11.14: Mapping of ventilated areas when step wise velocity development is used to achieve ventilation. White areas represents fully wetted flow. Light blue are areas where the flow remained ventilated during the deceleration, but was fully wetted during acceleration. Dark blue represents areas where the flow remained ventilated at all times.

Figure 11.15 shows the non-dimensional force coefficients, C_L and C_D plotted as a function of the Froude number (Fn_h) for every angle tested with step wise ventilation in the range $Fn_h = 0.047 - 0.582$. It can be observed that the increase for each lift coefficient plotted for a yaw angle, reduces when $\alpha \leq 10°$. The lift for different angles are even closer in values as the angle surpasses 15°. Which is the lower boundary for ventilation.

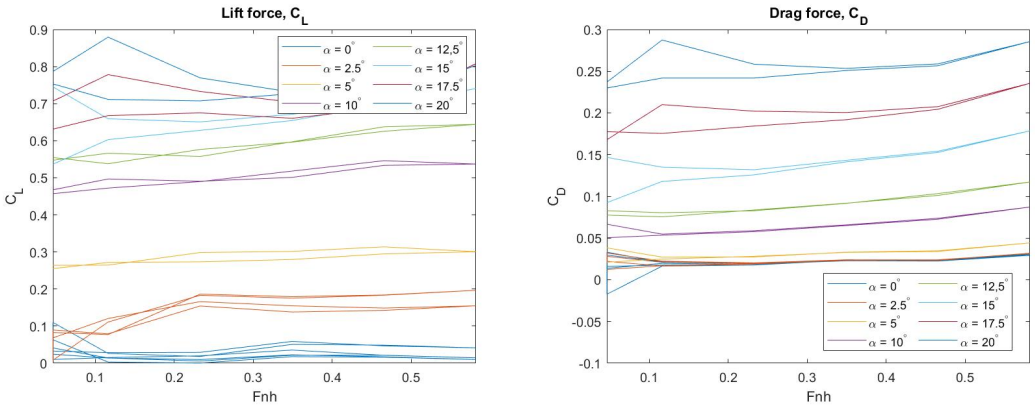

(a) C_L (b) C_D

Figure 11.15: The non dimensional lift (C_L) and drag (C_D), as a function of Fn_h, plotted for all angles $0 - 20°$.

A consequence of ventilation can be a dramatic loss of the lifting force, which can negatively

impact speed, stability and manoeuvrability. This force reduction could be clearly seen for the step wise ventilation in figure 11.16. Here, two partially ventilated runs and one non-ventilated are plotted as a function of the lift coefficient and the Froude number. C_L during acceleration is marked with dashed lines. Solid lines marks deceleration. While the non-ventilated state remained close in data throughout the acceleration and deceleration, the ventilated foils showed discrepancies at lower Froude numbers. This is caused by the different points of inception and washout due to hysteresis. At high Froude numbers, where the flow remained ventilated at all times, the data coincided. At lower Froude numbers however, where the hysteresis effect caused the ventilated flow to remain longer during deceleration, the loss of lift became visible. For a 20° angle of attack, the lift started to differ at $Fn_h = 0.349$, which marks the lower boundary for ventilation seen in figure 11.11. (Breslin & Skalak, 1959) reported reductions in the lift coefficient of up to 70%, in this thesis the reduction was found to be approximately 20% at most, however only a selection of runs were checked.

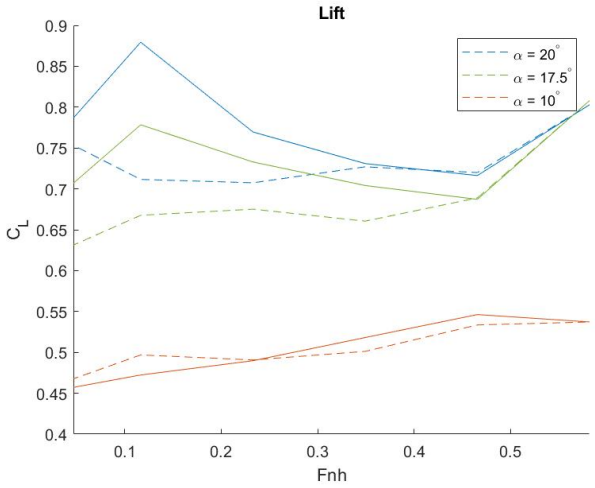

Figure 11.16: Absolute hydrodynamic lift coefficient plotted as a function of the Froude number for three selected yaw angles. Dashed lines represents the lift coefficient during acceleration and solid lined during deceleration. $\alpha = 20°$ and $\alpha = 17.5°$ shows two partially ventilated runs, while $\alpha = 10°$ remains fully wetted.

Quasi steady ventilation

For the quasi steady tests the maximum velocity was kept constant at 2.0m/s, or $Fn_h = 0.931$, while the acceleration and yaw angle were the varying parameters. In figure 11.17, the flow regimes are mapped as a function of the yaw angle and acceleration. Only partial ventilation was achieved during these tests and are marked as green in the plot. In the white regions the flow remained fully wetted.

By adjusting the acceleration, the effect it had on ventilated flows could be investigated. One noticed effect was the shift in the angle that marked the transition from fully wetted flow to a ventilated one, as is visualized in figure 11.17. At lower accelerations, namely $a \leq 0.15$, this angle was $\alpha = 15°$. However, as the acceleration was increased, the flow remained non-ventilated until the angle of attack was increased to $\alpha = 16°$. Here, the ventilation was reached conclusively for all accelerations.

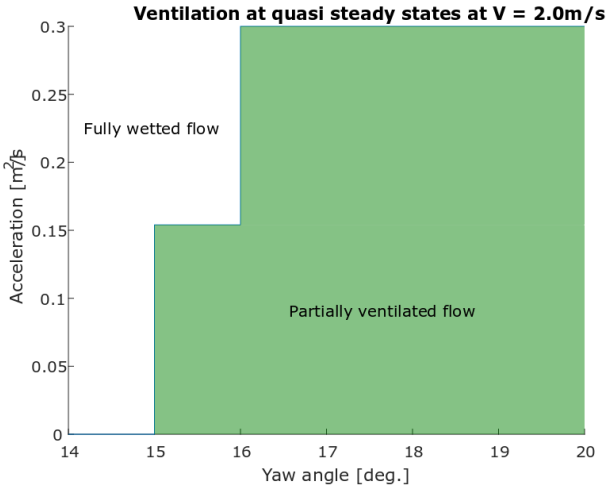

Figure 11.17: *Flow regimes - quasi steady states.* Ventilated areas are mapped as a function of acceleration and yaw angles. The foil was towed in a quasi steady state, with a maximum Froude number = 0.931. ($V = 2.0m/s$)

For these conditions the points of inception and washout were plotted as functions of Froude numbers and acceleration. The ventilated areas during acceleration and deceleration could then be mapped as seen in figure 11.18. Here, it could be observed that the opposite trend from the step wise ventilation runs transpired: inception would occur at lower Froude numbers than washout. This trend became more apparent as the acceleration increased, at the highest acceleration, $a = 0.3m/s^2$, ventilation developed almost immediately during acceleration and disappeared as soon as the foil started decelerating. The early washout of the ventilation when the acceleration was increased is assumed to be due to the water "pushing back" with greater force. Hence, the cavity tunnel was dissolved and the air connection between free surface and suction side was disconnected. The remaining air bubbles were simultaneously forced back and the flow returned to fully wetted.

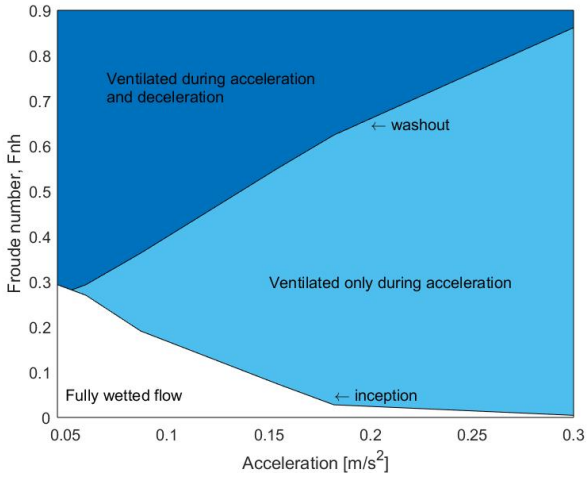

Figure 11.18: Map over ventilated areas as a function of Fn_h and acceleration, for a quasi steady state at a 17.5° yaw angle. The foil was towed with a constant acceleration until it reached a maximum velocity, V = 2m/s ($Fn_h = 0.931$), after having reached the maximum velocity the foil was decelerated at the same rate. The bottom line represents the point of inception during the acceleration and the top line is the point of washout during deceleration. Light blue represents areas that were only ventilated during acceleration. Dark blue areas were ventilated at all times.

The lowered inception point as the accelerations are increased, can be explained by considering the unsteady lift force and the added mass effect. As is shown in equation (11.1.2) and (11.1.3). The lift force can be divided into two components: steady lift and unsteady lift force, where the unsteady component is connected to the added mass generated by the acceleration. In figure 11.19a, the unsteady lift force is plotted as a function of acceleration. Figure 11.19b plots the point of inception for quasi steady states as a function of acceleration and velocity. This shows how the point of inception decreases at the same time as the unsteady lift force increases when the acceleration grows.

$$F_y = F_{y,unsteady} + F_{y,steady} \tag{11.1.2}$$

$$F_{y,unsteady} = \frac{1}{2}\pi\rho(\frac{c}{2})^2 \sin^2(\alpha) \tag{11.1.3}$$

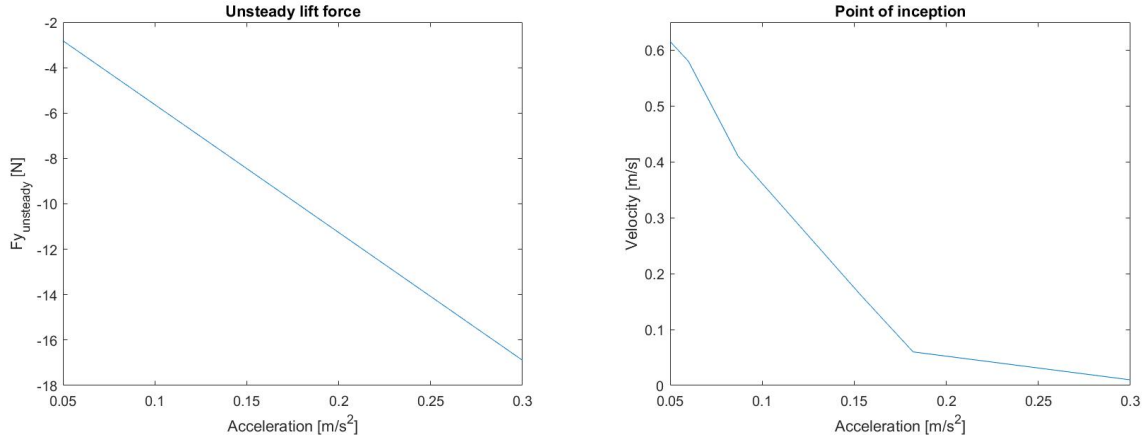

(a) (b)

Figure 11.19: Figure (a) shows the unsteady part of the lift force, $F_{y,unsteady}$ as a function of the acceleration. Figure (b) plots the point of inception as a function of velocity and acceleration. Both plots are based on experiments conducted on a foil with a 17.5° angle of attack in a quasi steady state with maximum velocity, $V = 2.0m/s$. Note that this plot only involves the accelerating part of the run and excludes the deceleration. The unsteady lift force is given in negative values.

Figure 11.20 shows two towing tests, where both foils have been accelerated to the maximum velocity, using a quasi steady state. Figure 11.20a was towed at the lowest acceleration used, $a = 0.046m/s$ and figure 11.20b at the highest, $a = 0.3m/s$. The figures shows the ventilated flows at the point where they were concluded to be at its largest, by calculating from pictures taken at 5 second intervals. Figure 11.20b had a ventilated area approximately 18% larger. The ventilated area over the entire time span is summarized in table C.2 and C.3 in appendix C, where the area of ventilation was documented from inception to washout. From the tables it is clear that the aerated bubble expanded much faster at higher a higher acceleration, but the ventilation endured to much lower Froude numbers when the acceleration rate was lower.

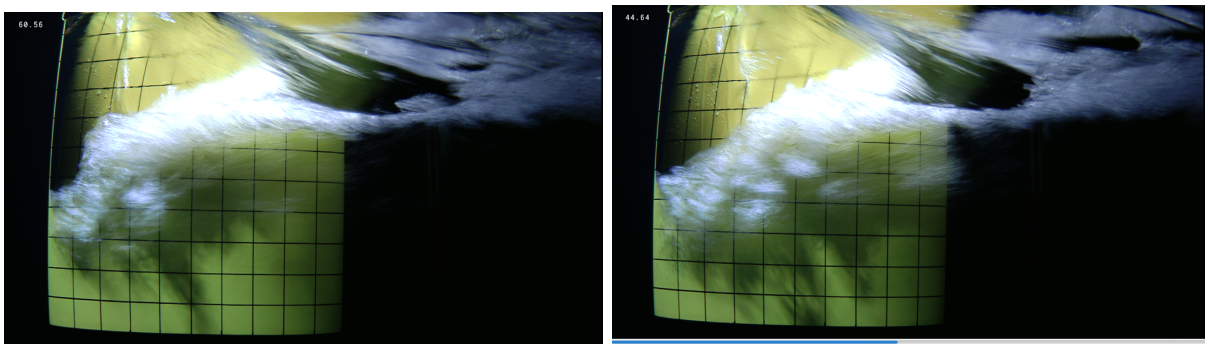

(a) Run 3006: $a = 0.046m/s^2$ (b) Run 4013: $a = 0.3m/s^2$

Figure 11.20: Run 3006 and 4013. Both are towed in a quasi steady state at maximum velocity, $V = 2.0m/$, $Fn_h = 0.931$, with an angle of attack, $\alpha = 17.5°$.

It is clear that the acceleration has an affect on the duration and size of the cavity. By plotting the lifting force (F_y) of the lowest and highest tested acceleration against each other, it can be observed that the effect on the lift is minimal. See figure 11.21. The lift coefficient is noticeably at lower Froude numbers, and particularly around $Fn_h \approx 0.5$, but as the Froude number grows, the lift coefficients goes towards the same values. The lift and drag coefficient was also plotted as a function of yaw angles in figure 11.22, which also showed force coefficients of similar sizes. Therefore, there are no significant effect on the hydrodynamic forces caused by the acceleration, most likely the difference in ventilation size was not considerable enough to cause an effect on the lift.

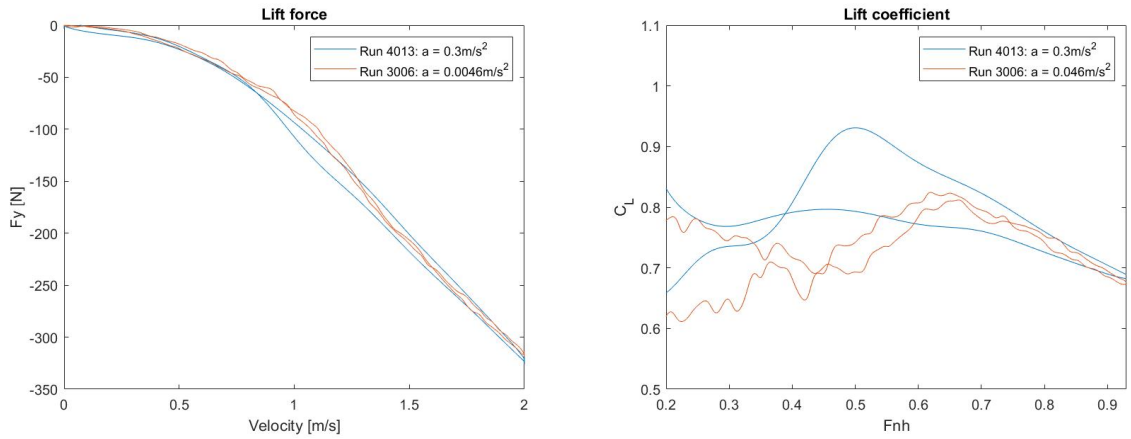

Figure 11.21: Lift force and lift coefficient for quasi steady state at angle of attack, $\alpha = 17.5°$, at the maximum and minimum acceleration tested. Respectively, $a = 0.3m/s^2$ and $a = 0.046m/s^2$. Lift coefficient is given in absolute values.

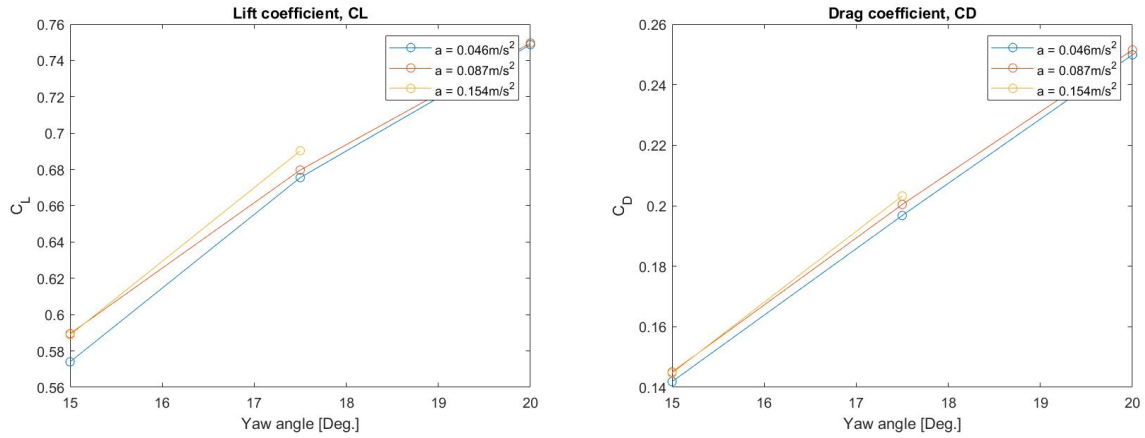

(a) Lift coefficient (b) Drag coefficient

Figure 11.22: The hydrodynamic coefficients for three quasi steady towing tests at $a = 0.046m/s^2$, $a = 0.087m/s^2$ and $a = 0.154m/s^2$, plotted as a function of the angle of attack. The point plotted are the mean values at maximum velocity, V = 2.0m/s or $Fn_h = 0.931$. The two first accelerations are plotted for $\alpha = 15°, 17.5°, 20°$, while the last only has points from $\alpha = 15°$ and 17.5°.

Dynamic angles

The effect of dynamic angles on ventilation were tested by dynamically rotating the foil to different angles at various Froude numbers. Ventilation proved to be less consistent for this method, and would not always give the same result if the same conditions where repeated. For the foil to be more susceptible to ventilation, the immersed depth was decreased, such that the Froude numbers increased. Figure 11.23 shows an overview over when ventilation occurred at different yaw angles and Froude numbers. Red illustrates conditions where ventilation never occurred, green conditions were they occurred every time and yellow conditions where ventilation occurred during some tests, but not all. White areas were not tested. The foil was rotated to both the negative and positive yaw angle during one run. Due to camera placement, only the ventilated flows induced on the negative yaw angle are documented.

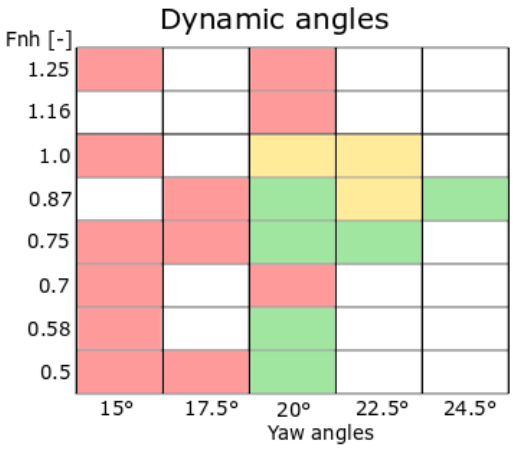

Figure 11.23: *Flow regimes - dynamic angles.* The figure illustrates the dynamic angles tested for depth based Froude number (Fn_h) and yaw angles. Each angle were tested at both positive and negative y-axis during a run. Green areas are conditions where ventilation occurred, in the red areas no ventilation occurred, the blank areas were not tested.

No ventilation occurred for dynamic angles before the angle of attack exceeded 20°. Additionally, it would develop less frequently at Froude numbers above Fnh = 1.0. The occurrence of ventilated flows was, in general, less consistent and occurred less frequently while using dynamically changing angles. Higher velocities and yaw angles were needed for aerated flows to develop and the tests would give different results for the same run conditions. This placed the runs in a bi-stable regime, as defined by Harwood et al. (2016). Here, ventilation is highly dependant on outside factors such as disturbances in the free surface.

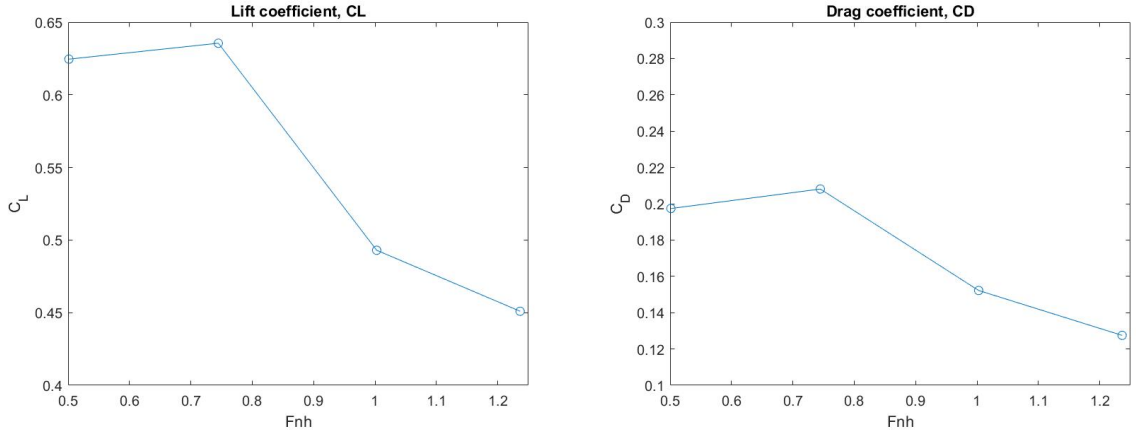

(a) C_L (b) C_D

Figure 11.24: Lift and drag coefficient as a function of Froude number for runs with dynamically changing angles

11.1.3 Comparing the methods

Figure 11.25 shows four ventilated flows at the same Froude number, Fn_h = 0.5, which were developed using four different conditions. (1) step wise development at α = 17.5°. (2) quasi steady state the lowest acceleration tested at α = 17.5°. (3) Quasi steady state at the highest acceleration tested at α = 17.5°. (4) Dynamically changing angle for α = 20°. These are listed in table 11.1. The dynamic case uses a larger angle of attack as no ventilation occurred there at lower angles. In this case the foil has a smaller immersed depth as well, h = 25cm, compared to h = 47cm which was used for the three first examples. From the figures it is clear that the ventilation on figure 11.25c, which shows a quasi steady state with $a = 0.3m/s^2$, developed faster and covers a larger area than the other conditions. The dynamic angle run, 11.25d is noticeably smaller, indicating that ventilated flow developed slower and at higher requirements for dynamic angles than for static angles. The difference between figure 11.25a, 11.25b are less distinct from each other, seemingly it did not result in large differences between a quasi steady state at a low acceleration and increasing the velocity in increments.

Table 11.1: Run numbers and conditions used for comparison

Run number	α [Deg.]	Type	Velocity [m/s]	Fnh	Acceleration $[m/s^2]$
2190	-17.5	Step-wise	1.25	0.582	
3006	-17.5	Quasi steady	2.0	0.931	0.046
4013	-17.5	Quasi steady	2.0	0.931	0.3
4019	-20	Dynamic angles	0.62	0.5	

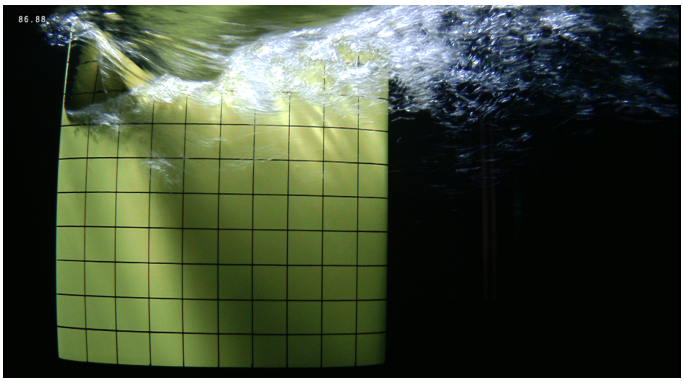

(a) Run 2190: step wise method, α = 17.5°

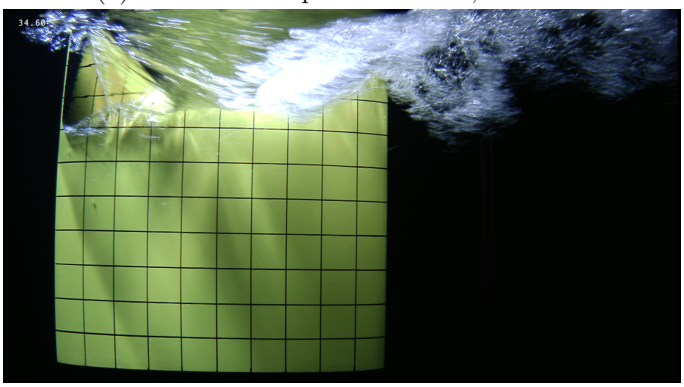

(b) Run 3006: Quasi steady state, $a = 0.046m/s^2$, α = 17.5°

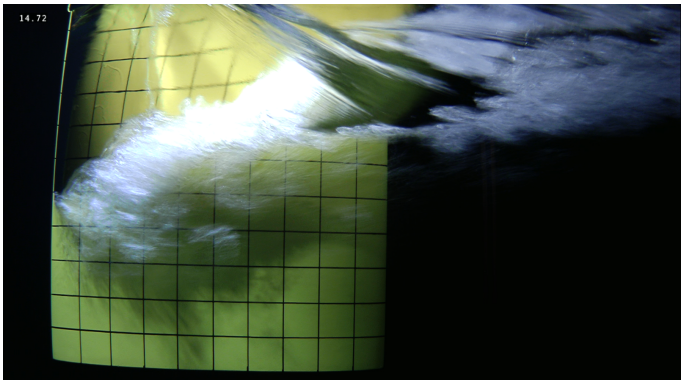

(c) Run 4013: Quasi steady state, $a = 0.3m/s^2$, α = 17.5°

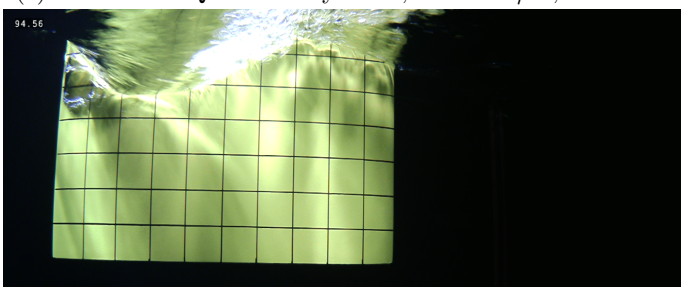

(d) Run 4019: Dynamic angles, α = 20°

Figure 11.25: Ventilated areas at Fnh =0.5.

The mean force coefficients, C_L and C_D are listed in table. 11.2. The drag coefficient was close to identical for all cases, which is logical as the drag is not very sensitive to boundary layer separation, or multi-phase flows along the sides of the lifting body. The dynamic angle has a lower lift coefficient compared to the other runs, despite having a larger inclination and smaller cavitation bubble.

Table 11.2: Mean forces at Fn_h = 0.5 using different methods to achieve ventilation, given in absolute values

Run number	Method	Mean C_L	Mean C_D
2190	Step wise	0.69	0.20
3006	Quasi steady, $a = 0.046m/s^2$	0.72	0.20
4013	Quasi steady, $a = 0.3m/s^2$	0.70	0.20
4019	Dynamic angles	0.62	0.20

In figure 11.26 the non-dimensional area of each example has been plotted against the Froude number. Non-dimensional area was used, as the dynamic angle used a different submergence and the ventilated area was therefore divided by the total area under the still free surface. This was to make them comparable to each other. The exact values are listed in appendix C, and was found by taking snapshots from the videography at 5 second intervals. The grid pattern on the foil surface was then used to calculate the area covered by aerated flow. The area was counted down to an accuracy of $\frac{1}{8}$ squares, where each square measured $25cm^2$. Meaning the area counted has an error of $A \pm \frac{25}{8}cm^2$. Additionally, large angles caused a very deformed and steep bow wave, due to this, the entire waterline was not within the cameras view at all times. This area could not be counted in to these calculations. All data, except the dynamic data are taken from one run at α = 17.5°. The dynamic data points are calculated from the mean of several runs, as the angles were not adjusted until the velocity was fully developed. The data is therefore from a selection of runs at different Froude numbers and α = 20°.

The quasi steady state at $a = 0.3m/s^2$, developed ventilation earlier and gained the largest area. The step-wise method has a slightly earlier inception than the quasi steady at $a = 0.046m/s^2$, but the area stays at a similar size as it develops. No conclusions can be made for higher Froude number as the step wise method was not tested for higher Froude numbers for α = 17.5°.

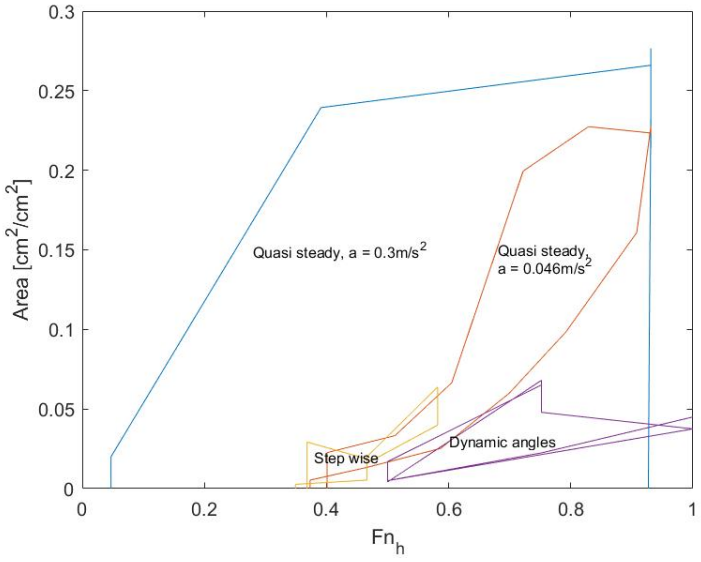

Figure 11.26: The ventilation areas as a function of the Froude number (Fn_h). The quasi steady and step wise data are from the runs listed in appendix C, all at 17.5°. The data for the dynamic angles are taken as averages from run nr. 4019, 4020, 4021, 4022, 4033 and 4034, at 20°. The data for the dynamic values had to be taken at a greater angle as no ventilation appeared for these conditions at 17.5°.

11.2 Numerical Results

This section presents and discusses the numerical results. Additionally, the wave profiles found numerically are qualitatively compared to the experimental wave profiles.

11.2.1 Lift and drag forces

The force history of the drag force (F_x) and lift force (F_y) are plotted as a function of time for each simulated yaw angle in figure 11.27a and 11.27b. They include the acceleration period of two seconds. The forces can all be seen to be converging towards a mean value after approximately ten seconds. The mean values are listed in table 11.3

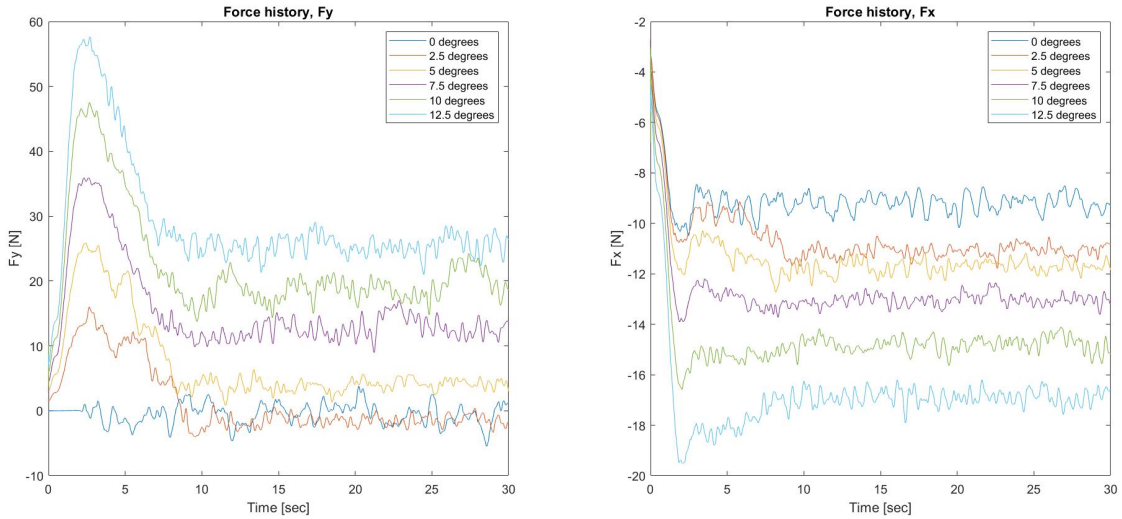

(a) Lift force, F_y

(b) Drag force, F_x

Figure 11.27: Force history of the forces for all cases simulated in Fine Marine. The foil were simulated with yaw angles from 0° to 12.5° with a velocity, V = 1.0m/s, Fn_h = 0.466

Table 11.3: Numerical mean values for each simulated angle of attack (α)

α [Deg.]	Mean F_x [N]	Mean F_y [N]	Mean $C_{L,3D}$	Mean $C_{D,3D}$
0°	-9.20	-0.52	0.004	0.08
2.5°	-10.82	-1.72	-0.01	0.09
5°	-11.85	2.94	0.03	0.10
7.5°	-13.00	12.93	0.11	0.11
10°	-14.77	19.44	0.17	0.13
12.5°	-16.86	25.38	0.22	0.14

11.2.2 Wave profiles

The wave profiles obtained from CFView are shown here for the angle of attack, α = 12.5°. A comparison of the wave profiles from the pressure and suction side for α = 12.5° is shown in figure 11.29, by visualizing the mass fraction between the two fluids. For the inclined cases a flow separation is expected to occur close to the leading edge on the suction side of the foil. By investigating the hydrodynamic pressure, a low pressure zone can be observed close to the

leading edge in figure 11.30b and another near the trailing edge in figure 11.30a, which indicates flow separation. Indications of separation can also be seen in figure 11.29, by the vortex pattern forming close to the leading edge. The actual waterline around the foil is logical and follows wave generation theory, with a wave elevation by the leading edge, showing the bow wave, and a slight elevation by the trailing edge where the stern wave should be.

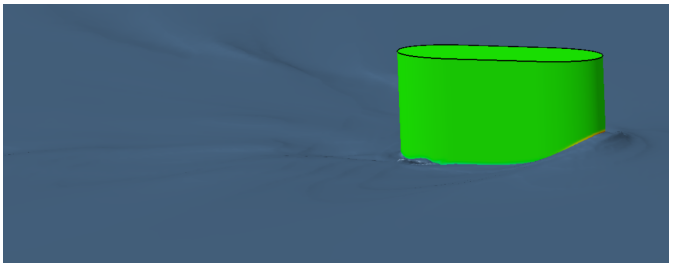

(a)

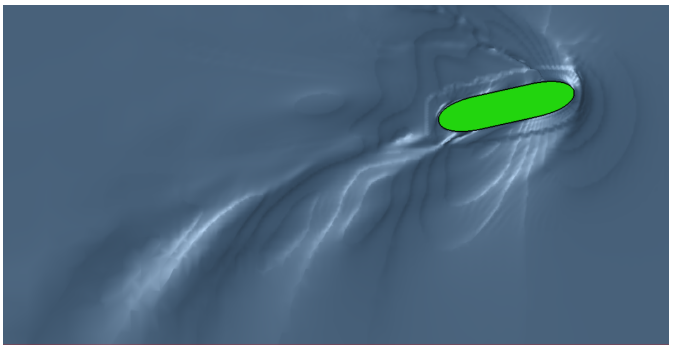

(b)

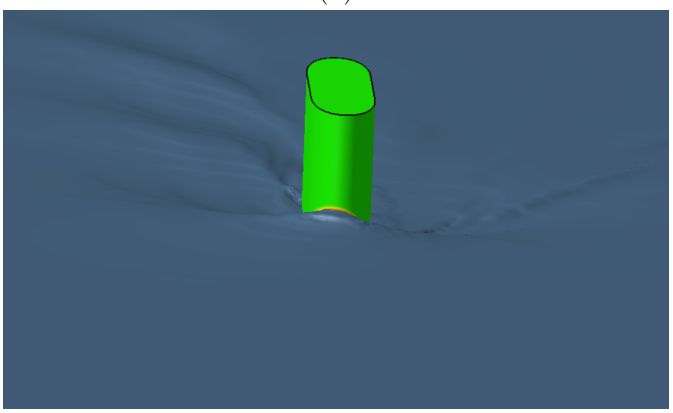

(c)

Figure 11.28: Wave profiles at $\alpha = 12.5^{\circ}$ simulated in Fine/Marine

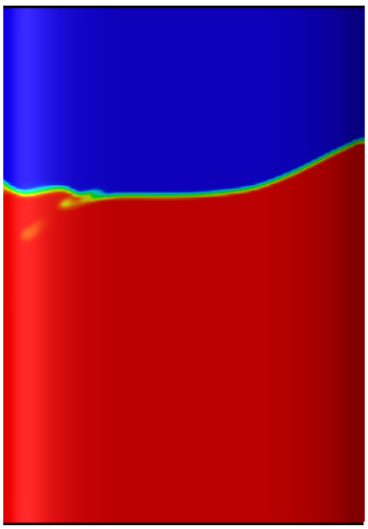

(a) Pressure side, leading edge is facing right.

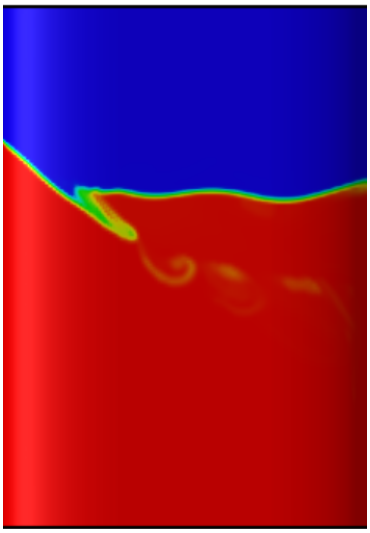

(b) Suction side, leading edge is facing left.

Figure 11.29: The pressure and suction side of the foil at $\alpha = 12.5^{\circ}$

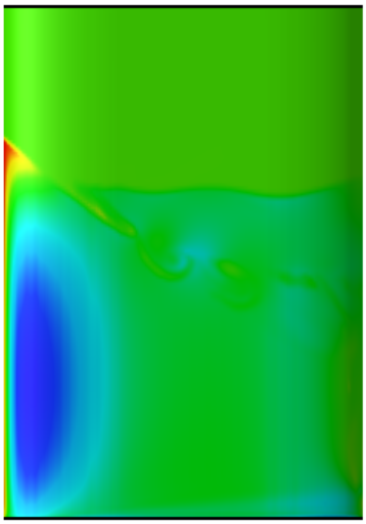

(a) Pressure side, leading edge is facing right.

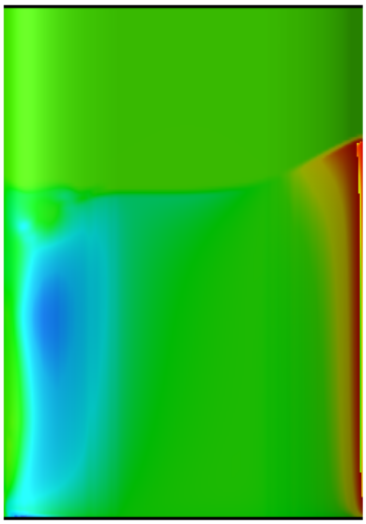

(b) Suction side, leading edge is facing left.

Figure 11.30: Hydrodynamic pressure for $\alpha = 12.5^{\circ}$

11.3 Comparison of the experimental and numerical result

This chapter compares the results from the numerical study to the results obtained from the towing tests conducted on foil 1. This includes hydrodynamic forces in x- and y-direction (drag and lift), as well as comparisons of the wave profiles on the foil.

11.3.1 Wave profiles

Here, a visual qualitative comparison of the wave profiles on the blunt foil and the numerical simulations are presented. By observing the numerical wave profiles the bow wave seem to be of a very similar dimension, although it is difficult to quantify and give a precise bow wave height

for the wave profile. The numerical wave elevation in the bow can also be seen as increasing with an increasing angle of attack, in good agreement with the numerical result. A flow separation near the leading can be observed in the numerical waterline on the suction side. There is noticeably more distortion and disturbances in the wake and near the trailing edge in the experimental photos, but the actual waterline along the hull seems to be in good agreement with each other.

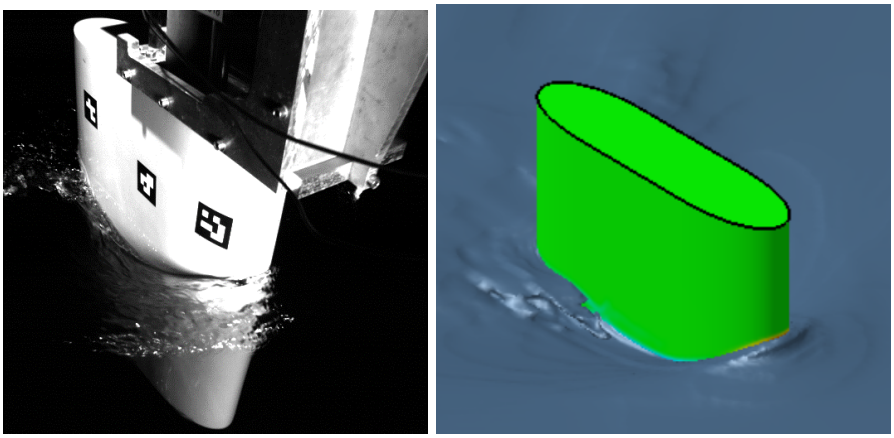

(a) $\alpha = 0°$ (b) $\alpha = 0°$

Figure 11.31: Wave profile at $\alpha = 0°$

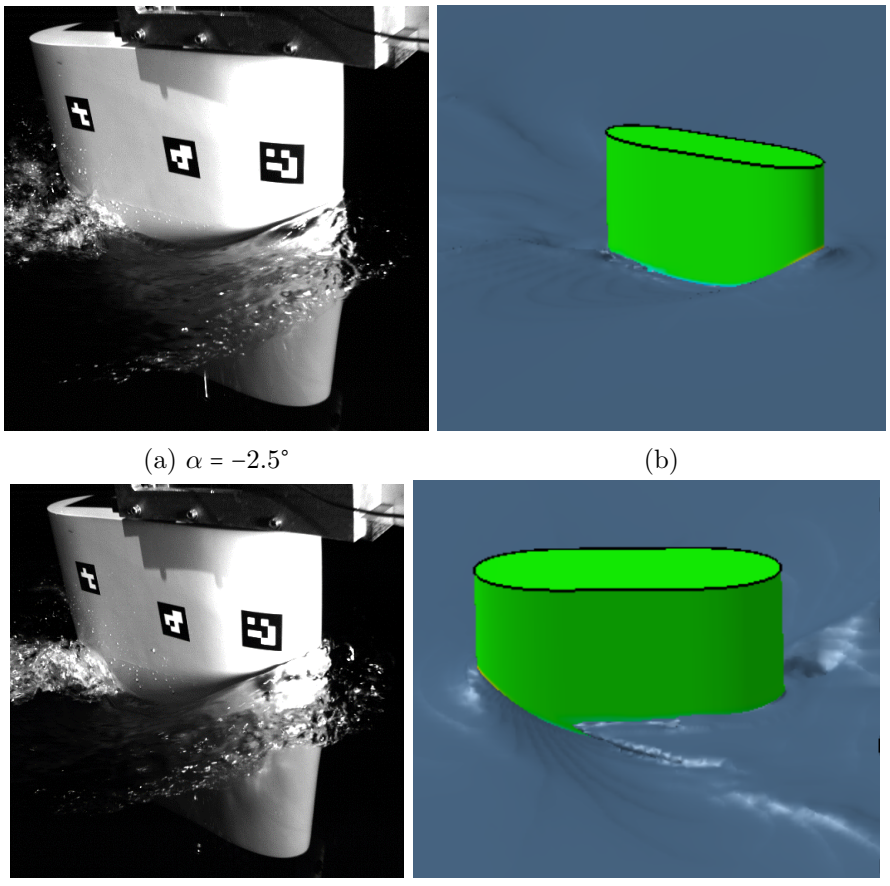

(a) $\alpha = -2.5°$ (b)

(c) $\alpha = +2.5°$ (d)

Figure 11.32: Wave profiles at $\alpha = \pm 2.5°$

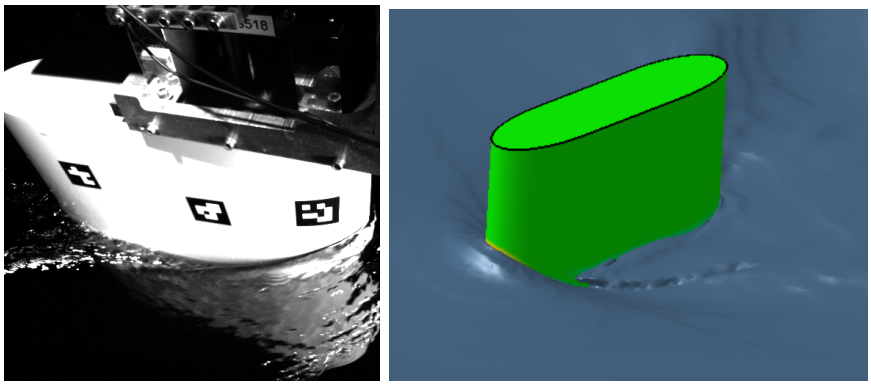

(a) $\alpha = -5^{\circ}$ (b) $\alpha = -5^{\circ}$

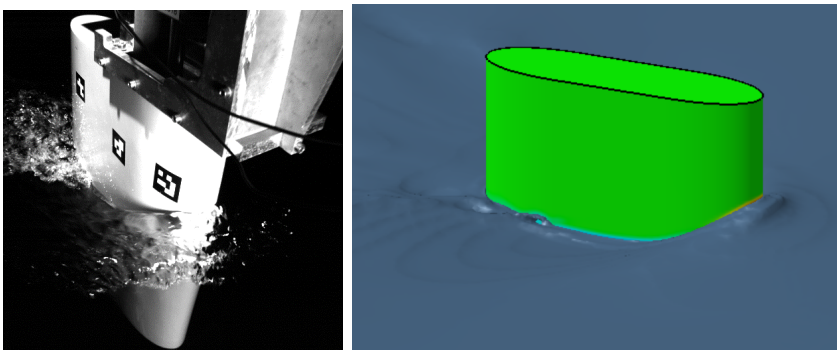

(c) $\alpha = +5^{\circ}$ (d) $\alpha = +5^{\circ}$

Figure 11.33: Wave profiles at $\alpha = \pm 5^{\circ}$

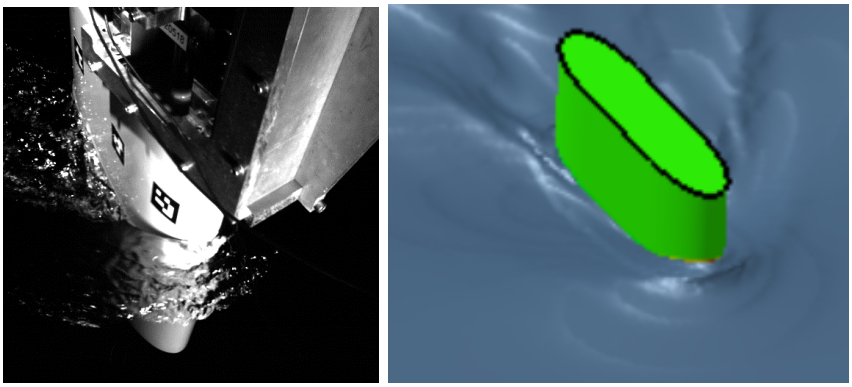

(a) $\alpha = -10^{\circ}$ (b) $\alpha = -10^{\circ}$

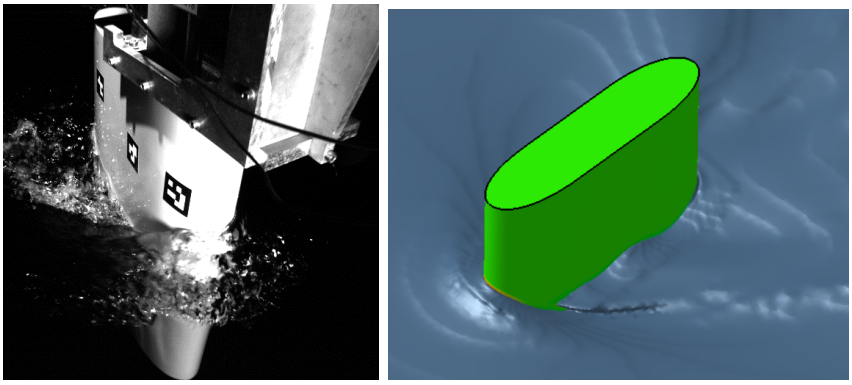

(c) $\alpha = +10^{\circ}$ (d) $\alpha = +10^{\circ}$

Figure 11.34: Wave profiles at $\alpha = \pm 10^{\circ}$

11.3.2 Hydrodynamic forces

The hydrodynamic forces in x- and y-direction from the experimental and numerical investigations are plotted against each other in figure 11.35 and 11.36. As can be seen, the numerical lift force values are significantly lower than the experimental values. There is a discrepancy in the drag for as well, but not as drastic. For comparison, the theoretical values from linear foil theory were plotted against the lift force, which followed the experimental data well, and suggests that the error lies in the numerical simulations. Additionally, as the only changing parameter in the simulations was the angle of attack, the forces would be expected to follow a close to linear increase. This is not the case, particularly the results from the 5° inclination deviates from this linearity.

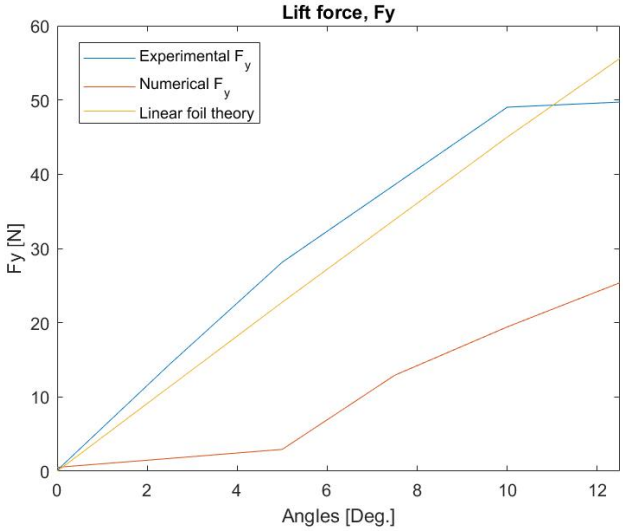

Figure 11.35: Experimental, numerical and theoretical lift forces plotted against the yaw angles at V = 1.0m/s or Fnh = 0.466. Experimental forces are plotted for foil 1 from the mean values of several runs on both the positive and negative yaw angle.

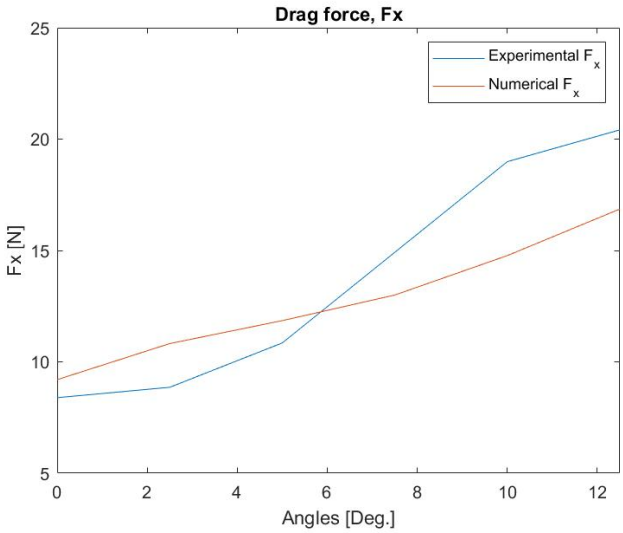

Figure 11.36: Experimental and numerical drag forces plotted against the yaw angles at V = 1.0m/s or Fnh = 0.466. Experimental forces are plotted from foil 1 from the mean values of several runs on both the positive and negative yaw angle.

The disparity between the numerical and experimental lift forces were concerning, at an angle of attack $\alpha = 10°$, the experimental F_y were more than twice as large as the numerical F_y. By comparing the data to theoretical values found using linear foil theory, it clearly indicated that the issue stemmed from the simulations. The experimental values lined up well with the theoretical and was therefore considered reliable. There was also a difference in the drag forces, but not as drastic, the gap was at its largest at $\alpha = 10°$, where the model test gave an approximately 25% larger lift force. The reasons contributing to the bad F_y results, will be discussed, but the difference was so drastic that after a close inspection of the numerical set up, it was decided to contact Numeca for advice. No reply was received within the time limitation.

A probable reason for the issue could be that the choice of turbulence model led to an insufficient modelling of the flow around the foil, particularly the flow separation. The foil was operating in a sub-critical Froude number region, with $Fn_h \approx 0.47$, but the Reynolds number had a value of $Rn \approx 5 \cdot 10^{-5}$, placing it in the critical Reynolds regime. This is where the separation point transitions from laminar to turbulent (Schlichting & Gersten, 2016). For a blunt body with high pressure gradients, such as this, it can lead to complications. In a numerical study conducted on risers by Eca et al. (2014), it was found that in this Reynolds area the CFD prediction for the average drag force could vary by as much as three times the minimum value around $Rn = 5 \cdot 10^{-5}$, depending on which turbulence model was used. It was suggested by Eca et al. (2014), that numerical errors could lead to very misleading results. These effects are more extreme for a circular cylinder, but would also affect a blunt body, such as foil 1, which was used for the simulations. The lift forces are also more affected by changes in separation and this could explain why the lift force was heavily affected and not the drag force.

The $k - \omega$ SST turbulence model is commonly used to simulate surface vessels as it is a relatively fast approach which usually gives good results for a wide range of flows (Rodriguez, 2019). RANS equations and the $k - \omega$ turbulence model was also used by Charlou et al. (2020) with good results. The same method was used by Andrun et al. (2020), where force discrepancies also occurred, but there the issues were with the drag forces. However, it seems like the approach and use of RANS equations were not capable of modelling the flow and especially flow separation in critical Reynolds regions. One solution to improve the results could be to model the flow again using a direct turbulence solver or a combination RANS, LES solver. Such as the Detached Eddy Simulation (DES). A better option could also have been to use the thin foil (foil 2) for the simulation as well as sharper, less blunt body would have been less susceptible to the Reynolds effects.

To test the theory that the error stems from the choice of turbulence model, an additional simulation was run by the CFD supervisor of this thesis at $\alpha = 7.5°$ with an IDDES - SST turbulence model, which is a delayed detached eddy simulation with improved wall modelling, optimized with shear stress transport (SST). The resulting hydrodynamic forces are summarized in table 11.4. It is obvious that the IDDES model gives a much better estimation of the lift force, it also gives an drag force closer to the experimental result.

The down side to using a direct solver, such as the detached eddy simulation to estimate the flow is that it more time consuming and computationally demanding than RANS-solvers (Rodriguez, 2019). Therefore, although they give very accurate results, they are not always a practical approach. In this case, new simulations using DES - solvers seems necessary as a pure RANS solver was not sufficient. It seem likely that the DES is a minimum requirement for solving this problem and provide quality validation for CFD wave profiles. A possibility could also be to use a pure LES solution for the entire flow, this is however, very computationally demanding and as the provisional results are very promising, the DES approach seems sufficient and satisfactory for this problem.

Visualizations of the wave profiles from the new simulations are presented in figure 11.37. As there was no towing test conducted for the blunt foil at an angle of attack α = 7.5°, no close comparison can be made. However, one clear difference between the $k-\omega$ free surface simulations and the DES is a greater presence of disturbances behind the boundary layer separation and in the wake. This visually coincides better with the appearance of the model test flow, and is a further indication that the DES turbulence model is better equipped at handling the flow problem here.

Table 11.4: The resulting mean hydrodynamic forces found from experiments, linear theory and numerically, using two different turbulence models. The blunt foil was not tested at α = 7.5° and the value is taken as the mid point between 5° and 10°

Method	α	Mean F_x [N]	Mean F_y [N]
$k-\omega$ SST	7.5°	13.00	12.93
IDDES - SST	7.5°	14.06	32.02
Experimental	7.5°	14.92	38.59
Theoretical	7.5°		33.98

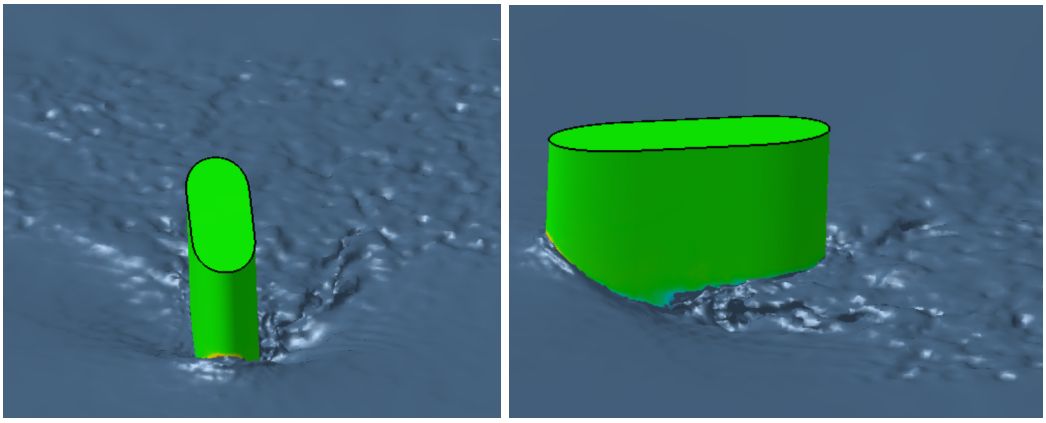

(a) (b)

Figure 11.37: Free surface flows around foil 1, using IDDES - SST turbulence modelling.

Chapter 12

Conclusion

Model testing of free surface flows around a surface-piercing hydrofoil has been combined with numerical simulations, in order to provide quality data on the prediction of wave profiles and ventilated flows. This thesis included two separate foils for experimental testing: One blunt to investigate wave pattern generation and one slender to incept and investigate ventilated flows. Numerical simulations of the blunt foil has also been conducted in order to provide insight on the accuracy of CFD in predicting wave profiles.

For the multi-phase flow investigation, all ventilation inceptions were achieved using spontaneous stall-induced inception. The varying parameters were the Froude number, angle of attack and acceleration. Two manners of velocity developments were used: Step-wise acceleration of the velocity, quasi steady state. Additionally, the foil were run using both static and dynamic angles of attack.

The results found from the step-wise ventilation, confirmed previous studies of multi-phase flows on vertical foils: spontaneous stall-induced ventilation develops at yaw angles exceeding the stall angle and leads to a reduction in the lift force as the pressure of the suction side becomes limited by the atmospheric pressure. Hysteresis was also documented: Washout at velocities more than 60% lower than the point of inception was observed. To reach full ventilation the Froude number had to surpass approximately $Fn_h = 1.2$.

For the quasi steady states the effect of the added mass and unsteady lift force caused cavity flows to develop earlier as the acceleration was increased, but it was also noted that a great angle of attack was required at accelerations above $a = 0.15m/s^2$. At the same time as the point of inception started earlier the washout would also occur earlier during deceleration, as the aerated areas was more quickly pushed back by the forces in the water at high deceleration rates.

The case of dynamically changing angles are relevant as they can more easily be translated to real life conditions. Here, ventilation occurred less frequently, at higher angles of attack and Froude numbers than in the other cases. Additionally, they were more irregular and different results would differ when the same conditions were repeated. Meaning that the ventilation were more dependent on outside factors, such as perturbations or other disturbances in the surface for inception to occur. Investigating the ventilation using static angles is a simple way observing the effects of factors such as acceleration and stall angles individually. Running a vessel straight ahead with a static and, is however, not very realistic to real life scenarios. Changing the angle dynamically more closely simulates the working conditions of lifting bodies, particularly the movement and application of rudders. This gives a better insight to how ventilation is likely to occur in real life situations. From the data obtained in these experiments it seems that ventilation develops more easily and drastically for the idealised conditions using a static angle. It is however evident that ventilated flows can have dramatic consequences if triggered correctly.

By comparing the different method used here to initiate ventilation, it was clear that the flow conditions before any actual ventilation occurred had a large impact on the flow. Higher accel-

eration would develop cavity bubbles faster and in greater sizes. However, if the velocities were increased too fast, higher angles were necessary, or no ventilation would develop. A dynamic versus static angle of attack would also significantly decrease the risk of ventilation.

The flow around the thicker foil was modelled using numerical simulations in Fine/Marine. Simulations were ran at six different angles of attack in the range $\alpha = 0 - 12.5°$. The waveprofiles were in good agreement with visual comparisons of the experimental ones, the lift force however did not agree with the experimental forces. The theoretical values found from linear theory, indicated that the fault was with the numerical models. The fault is assumed to stem from Reynold region of the foils. Even though the Froude numbers were sub-critical, the Reynold numbers were placed in a critical zone, due to this the $K - \omega$ (SST) turbulence model were not able to properly model the flow separation. This greatly affected the lift forces, the drag forces however, are less sensitive to the behaviour of the flow separation and the placement of the sepration point. Therefore, it was not affected in the same extent.

By analysing a test case using the detached eddy-simulation (DES) as the turbulence model, it was clear that a pure RANS method was not sufficient to predict the forces of this flow problem and the more computationally demanding DES, is necessary for quality results.

In conclusion, the experiments conducted on free surface flows on a surface-piercing foil provides interesting results, especially on the ventilated flows and its sensitivity to certain parameters. The numerical analysis provides observations on the complicated nature of the flow problem and although no conclusive results could be drawn on the validation of free surface wave prediction, it provides useful insight for further work.

12.1 Recommendations for future work

The following topics are recommended for further investigation:

All simulations should be repeated, using a detached eddy-simulation as the turbulence model for reliable free surface predictions. This way quality validation for CFD predictions of free surface flow can be provided.

The simulations should also be extended to include the the slender foil model. Ventilated flows are difficult to predict numerically, due to the sensitivity of ventilation inception and the inherent non-linearity of multi-phase flows. Numerical testing of this phenomenon could therefore help to draw conclusions on the accuracy of predicting ventilation.

Only a qualitative comparison of the numerical and experimental wave profiles were achieved. It would also be beneficial to run the simulations at lower Froude number to gain a clearer contrast between the waterline and solid surface of the foil. This way a computer vision technique can be used to detect the experimental wave profiles and provide a more accurate comparison to the numerical predictions.

The experiments conducted in this thesis were carried out without any turbulence stimulation. Turbulence affects the boundary layers and flow separation, and a recommendation for future testing would be to include turbulence stimulation to force a turbulent flow. This would provide a test case more transferable to real life situations, such as the case of rudders and ship hulls.

More extensive testing of ventilated flows using dynamically changing yaw angles would be beneficial, as these conditions proved less conclusive and less repeatable than tests were the angle of attack was static during the towing.

References

Andrun, M., Blagojevic, B., Basic, J., & Klarin, B. (2020). Impact of CFD Simulation Parameters in Prediction of Ventilated Flow on a Surface-Piercing Hydrofoil. *Ship Technology Research*.

Breslin, J., & Skalak, R. (1959). Exploratory Study of Ventilated Flows About Yawed Surface-Piercing Struts. *30th Symposium on Naval Hydrodynamics*.

Cengel, Y. A., & Cimbala, J. M. (2010). *Fluid Mechanics: Fundamentals and Applications, 2nd edition in SI units*. McGraw-Hill.

Charlou, M., Wackers, J., Deng, G., Guilmineau, E., Leroyer, A., Queutey, P., & Visonneau, M. (2020). Assessing Bi-Stable Ventilation for Surface-Piercing Hydrofoils Through Numerical Simulation. *Innov'sail 2020*.

Coleman, H. W., & Steele, W. G. (2009). *Experimental, Validation and Uncertainty Analysis for Engineers: 3rd Edition.* John Wiley & Sons.

Damley-Strnad, A., Harwood, C., & Young, Y. (2019). Hydrodynamic Performance and Hysteresis Response of Hydrofoils in Ventilated Flows. *6th International Symposiom on Marine Propulsors, smp'19*.

Eca, L., Vaz, G., Rosetti, G., & Pereira, F. (2014). On the Numerical Prediction of the Flow Around Smooth Circular Cylinders. *Proceedings of the ASME 2014 33rd International Conference on Ocean, Offshore and Arctic Engineering. Vol. 2: CFD and VIV*.

Faltinsen, O. (2005). *Hydrodynamics of High Speed Marine Vehicles*. Cambridge, United Kingdom: Cambridge University Press.

Harwood, C., Brucker, K., Montero, F., Young, Y., & Ceccio, S. (2014). Experimental and Numerical Investigation of Ventilation Inception and Washout Mechanism of a Surface-Piercing Hydrofoil. *30th Symposium on Naval Hydrodynamics*.

Harwood, C., Young, Y., & Ceccio, S. (2016). Ventilated Cavities on a Surface-piercing Hydrofoil at Moderate Froude Numbers: Cavity Formation, Elimination and Stability. *Cambridge University Press*.

Hirt, C., & Nichols, B. (1981). Volume of Fluid (VOF), Method for the Dynamics of Free Boundaries. *J. of Computational Physics, Vol. 39 (1)*.

Kolditz, O. (2002). *Finite Volume Method: Computational Methods in Environmental Fluid Mechanics*. Springer, Berlin, Heidelberg.

Kuiper, G. (1998). *Fluid Mechanics and its Application - In Fascination of Fluid Dynamics.* Wageningen, Netherlands: Kluwer Academic Publishers. (Cavitation Research and Ship Propeller Design, p. 33-50)

Limb, B., Work, D., Hodson, J., & Smith, B. (2017). The Inefficacy of Chauvenet's Criterion for Elimination of Data Points. *Journal of Fluids Engineering, Vol.139 (5)*.

Menter, F. R. (1994). Two-Equation Eddy-Viscosity Turbulence Models for Engineering Applications. *AIAA journal, Vol.32 (8), p.1598-1605*.

Molland, A., Turnock, S., & Hudson, D. (2011). *Ship Resistance and Propulsion.* Cambridge, United Kingdom: Cambridge University Press.

Nataletti, M., Savio, L., Hassani, V., & Auestad, (2019). Three-Dimensional Measurement of the Waterline of a Surface-Effect Ship. *J. Ocean.Eng 2020*. (For peer review)

Noblesse, F., Delhommeau, G., Guilbaud, M., & Yang, C. (2008). Simple Analytical Relations for Ship Bow Waves. *J. Fluid Mech, vol. (600), Cambridge University Press*.

Noblesse, F., Delhommeau, G., Liu, H., De-Cheng, W., & Yang, C. (2013). Ship Bow Waves. *ScienceDirect, Journal of Hydrodynamics, Elsevier*.

Numeca International. (n.d.). *FINE/MARINE8.2: Numeca Online Documentation Platform: Theory Guide.*

Rodriguez, S. (2019). *Applied Computational Fluid Dynamics and Turbulence Modelling: Practical Tips and Techniques, 1st edition.* Springer International Publishing.

Rothblum, R., Mayer, D., & Wilburn, G. (1969). Ventilation, Cavitation and Other Characteristics of High Speed Surface-Piercing Struts. *Naval Ship Research and Development Center, Report 3023*.

Sarraf, C., Djeribi, H., Prostin, S., & Billard, J. (2010). Thickness Effect of NACA Foils on Hydrodynamic Global Parameters, Boundary Layer States and Stall Establishment. *J. of Fluids and Structures, Vol. 26 (4)*.

Schlichting, H., & Gersten, K. (2016). *Boundary-Layer Theory.* Springer Berlin/Heidelberg.

Spalart, P. R. (2009). Detached-Eddy Simulation. *Annual Review of Fluid Mechanics, 41 (1), 181-202*.

Spalart, P. R., Deck, S., Strelets, M., & Travin, A. (2009). A New Version of Detached-eddy Simulation, Resistant to Ambiguous Grid Densities. *Theoretical and Computational Fluid Dynamics 20 (3), 181-195*.

Steen, S. (2014). *TMR7-Experimental Methods in Marine Hydrodynamics.* Centre of Marine Technology, Trondheim, Norway: Norwegian University of Science and Technology. (Lecture notes)

Steen, S., & Minsaas, K. (2014). *Ship Resistance: TMR4220 Naval Hydrodynamics.* Centre of Marine Technology, Trondheim, Norway: Norwegian University of Science and Technology. (Lecture notes)

Swales, P., Wright, A., McGregor, R., & Rothblum, R. (1974). The Mechanism of Ventilation Inception on Surface Piercing Foils. *Journal Mechanical Engineering Science*, *Vol. 16 No. 1*.

Tannehill, J., Anderson, D., & Pletcher, R. (1997). *Computational Fluid Mechanics and Heat Transfer* (2nd edition ed.). Washington DC, USA: Taylor and Francis.

Tennekes, H., & Lumley, J. (1972). *A First Course in Turbulence.* MIT Press.

Tu, J., Yeoh, G., & Liu, C. (2013). Chapter 5 - CFD Solution Analysis - essentials. *Computational Fluid Dynamics (2nd edition, pp. 177-217)*.

Voller, V. (2009). *Basic Control Volume Finite Element Methods for Fluids and Solids.* Danvers, USA: World Scientific Publishing Co. Pte. Ltd. (IISc Research Monographs Series (Vol. 1))

Wackers, J. (2021). Industrial Application of Adaptive Grid Refinement - The Case of Fine/-Marine. *Adaptive Modelling and Simulations (ADMOS 2021)*.

Wendt, J., Degrez, G., Degroote, J., Dick, E., Grundmann, R., & Vierendeels, J. (2009). *Computational Fluid Dynamics, an Introduction, 3rd Edition.* Berlin, Germany: Springer.

Wetzel, J. (1957). Experimental Studies of Air Ventilation of Vertical Semi-Submerged Bodies. *St. Anthony Falls Hydraulic Laboratory*.

Young, Y., & Brizzolara, S. (2013). Numerical and Physical Investigation of a Surface Piercing Hydrofoil. *3rd International Symposium on Marine Propulsors smp'13*.

Young, Y., Harwood, C., & Ceccio, S. (2017). Ventilation of Lifting Bodies: Review of the Physics and Discussion of Scaling Effects. *ASME. Appl. Mech. Rev.*, *Vol. 69 (1)*.

Appendix A

Run list

Table A.1: Run list - Waveprofiles - Foil 1

Foil 1 - Waveprofile					
Max. velocity = 1.25 m/s, Max. Fn_h = 0.582, Static angles All velocities are accelerated and decelerated step-wise as following: (0.1-0.25-0.5-0.75-1.0-1.25-1.0-0.75-0.5-0.25-0.1) [m/s]					
Run number	α [deg.]	F_y	F_x	$C_{L,3D}$	$C_{D,3D}$
1000	0	0.92	22.12	0.00	0.12
1001	0	-0.14	21.85	0.00	0.12
1002	0	0.26	22.14	0.00	0.12
1003	0	1.22	22.04	0.01	0.12
1004	0	-0.58	22.64	0.00	0.12
1005	0	-0.35	22.64	0.00	0.12
1140	2.5	22.49	23.61	0.12	0.13
1010	5	39.94	26.86	0.22	0.15
1011	5	41.14	26.59	0.22	0.14
1012	5	40.33	26.89	0.22	0.15
1013	5	39.02	26.79	0.21	0.15
1014	5	39.41	26.92	0.21	0.15
1015	5	44.69	28.00	0.24	0.15
1020	10	85.18	38.19	0.46	0.21
1021	10	84.42	37.59	0.46	0.20
1030	15	110.41	49.80	0.60	0.27
1031	15	100.99	47.81	0.55	0.26
1040	20	132.77	61.01	0.72	0.33
1041	20	123.83	60.07	0.67	0.33
1130	-2.5	-18.79	22.62	-0.10	0.12
1070	-5	-40.91	24.69	-0.22	0.1
1071	-5	-40.10	25.16	-0.20	0.14
1072	-5	-36.39	25.34	-0.20	0.14
1073	-5	-38.19	24.39	-0.21	0.13
1080	-10	-80.96	33.65	-0.44	0.18
1081	-10	-82.53	33.54	-0.45	0.18
1082	-10	-81.38	33.52	-0.44	0.18
1090	-15	-100.99	40.84	-0.55	0.22
1091	-15	-97.45	40.40	-0.53	0.22
1092	-15	-105.70	41.51	-0.58	0.23
1093	-15	-100.54	41.51	-0.55	0.23
1094	-15	-107.23	41.45	-0.58	0.23
1100	-20	-118.67	52.00	-0.65	0.28
1101	-20	-116.24	52.21	-0.63	0.28

Table A.2: Run list - step wise ventilation - Foil 2

Foil 2 - Ventilation								
Step-wise acceleration and deceleration of the foil. Static angles.								
Run nr.	α [deg.]	Vel. range [m/s]	Fnh range	Flow	F_y	F_x	C_L	C_D
2000	0	0.1-1.25	0.047-0.582	FW	1.82	5.38	0.00	0.03
2001	0	0.1-1.25	0.047-0.582	FW	7.60	5.63	0.04	0.03
2002	0	0.1-1.25	0.047-0.582	FW	2.66	5.44	0.01	0.03
2010	2.5	0.1-1.25	0.047-0.582	FW	37.96	7.83	0.21	0.04
2020	5	0.1-1.25	0.047-0.582	FW	58.53	10.95	0.32	0.06
2130	-2.5	0.1-1.25	0.047-0.582	FW	-36.11	5.85	-0.20	0.03
2031	-2.5	0.1-1.25	0.047-0.582	FW	-28.43	5.76	-0.15	0.03
2140	-5	0.1-1.25	0.047-0.582	FW	-55.21	8.12	-0.30	0.04
2160	-10	0.1-1.25	0.047-0.582	FW	-98.66	16.02	-0.54	0.09
2170	-12.5	0.1-1.25	0.047-0.582	FW	-118.32	21.53	-0.64	0.12
2180	-15	0.1-1.25	0.047-0.582	PV	-136.02	32.79	-0.74	0.18
2190	-17.5	0.1-1.25	0.047-0.582	PV	-148.42	43.27	-0.81	0.23
2200	-20	0.1-1.25	0.047-0.582	PV	-147.47	52.44	-0.80	0.28
2205	-20	1.5-2.0	0.699-0.931	PV	-352.90	117.60	-0.75	0.25
3000	-15	1.5-2.0	0.699-0.931	FW	-266.09	59.53	-0.57	0.12
3001	-15	1.0-2.0	0.466-0.931	PV	-256.93	53.86	-0.55	0.11
4027	-20	0.86-2.57	0.401-1.197	FV	-243.66	96.56	-0.33	0.13

Table A.3: Run list - Quasi steady ventilation - Foil 2

Foil 2 - Ventilation							
Quasi steady state Static angles Velocity, V = 2.0 m/s, Fn_h = 0.931							
Run nr.	α [deg.]	a $[m/s^2]$	Flow	F_y	F_x	C_L	C_D
3002	-15	0.046	PV	-268.91	66.50	-0.57	0.14
3003	-20	0.046	PV	-353.92	118.49	-0.75	0.25
3004	-20	0.046	PV	-355.35	118.81	-0.75	0.25
3005	-20	0.046	PV	-351.24	117.23	-0.75	0.25
3006	-17.5	0.046	PV	-317.12	92.40	-0.67	0.20
4001	-15	0.06	PV	-242.48	51.29	-0.52	0.11
4002	-17.5	0.06	PV	-313.57	91.97	-0.67	0.20
4003	-20	0.06	PV	-353.16	119.41	-0.75	0.25
4004	-20	0.087	PV	-352.18	118.13	-0.75	0.25
4005	-17.5	0.087	PV	-319.36	94.16	-0.68	0.20
4006	-15	0.087	PV	-276.96	68.15	-0.59	0.15
4007	-15	0.154	PV	-276.59	69.96	-0.59	0.14
4008	-15	0.154	FW	-265.74	58.74	-0.57	0.12
4009	-17.5	0.154	PV	-324.45	95.54	-0.69	0.20
4010	-17.5	0.182	PV	-321.12	93.94	-0.68	0.20
4011	-17.5	0.2	PV	-321.76	94.05	-0.68	0.20
4012	-17.5	0.25	PV	-322.32	94.27	-0.69	0.20
4013	-17.5	0.3	PV	-300.82	81.44	-0.64	0.17
4014	-16	0.154	PV	-321.64	94.01	-0.68	0.207
4015	-16	0.3	PV	-303.89	81.84	-0.65	0.17
4016	-15	0.154	FW	-261.67	58.84	-0.56	0.13
4017	-14	0.06	FW	-251.32	49.59	-0.53	0.11
4018	-17.5	0.087	PV	348.56	97.01	-0.59	0.16

Table A.4: Run list - Dynamic angles - ventilation - Foil 2. One run includes several angles, and this list includes all angles that reached a steady force. Each run is separated by a solid line. No flow regime is reported on positive angles, as there were no videography from this side.

Foil 2 - Ventilation									
Dynamic angles									
Run nr.	α [deg.]	h [m]	V [m/s]	Fn_h	Flow	F_y [N]	F_x [N]	$C_{L,3D}$	$C_{D,3D}$
2290	-20	0.47	1.25	0.58	PV	-153.69	51.72	-0.84	0.28
2290	+20	0.47	1.25	0.58		158.18	55.69	0.86	0.30
2290	-15	0.47	1.25	0.58	PV	-130.46	28.33	-0.71	0.15
2290	+15	0.47	1.25	0.58		134.59	32.70	0.73	0.18
2291	-20	0.47	1.25	0.58	PV	-153.09	48.88	-0.44	0.09
2295	-20	0.47	1.5	0.70	FW	-168.75	35.09	-0.64	0.13
2295	+20	0.47	1.5	0.70		124.35	25.00	0.47	0.09
4000	-15	0.47	2.5	1.16	FW	-326.74	63.46	-0.44	0.09
4019	-15	0.30	0.86	0.5	FW	-31.16	1.32	-0.36	0.08
4019	+15	0.30	0.86	0.5		34.23	1.32	0.39	0.02
4019	-20	0.30	0.86	0.5	PV	-48.16	16.54	-0.62	0.20
4019	+20	0.30	0.86	0.5		41.02	15.88	0.60	0.18

Table A.4: Run list - Dynamic angles - ventilation - Foil 2. One run includes several angles, and this list includes all angles that reached a steady force. Each run is separated by a solid line. No flow regime is reported on positive angles, as there were no videography from this side.

Foil 2 - Ventilation									
Dynamic angles									
Run nr.	α [deg.]	h [m]	V [m/s]	Fn_h	Flow	F_y [N]	F_x [N]	$C_{L,3D}$	$C_{D,3D}$
4020	-20	0.30	1.29	0.75	PV	-93.23	30.44	-0.48	0.16
4020	+20	0.30	1.29	0.75		94.45	34.70	0.49	0.18
4021	-15	0.30	1.29	0.75	FW	-71.47	17.13	-0.37	0.09
4021	+15	0.30	1.29	0.75		74.03	39.89	0.38	0.20
4021	-20	0.30	1.29	0.75	PV	-93.02	30.65	-0.48	0.16
4021	+20	0.30	1.29	0.75		92.14	33.30	0.47	0.17
4022	-15	0.30	1.72	1.0	FW	-103.44	23.37	-0.30	0.07
4022	+15	0.30	1.72	1.0		91.01	24.28	0.26	0.07
4022	-20	0.30	1.72	1.0	PV	-139.81	44.36	-0.40	0.13
4023	-20	0.30	1.72	1.0	FW	-138.78	43.58	-0.40	0.13
4023	+20	0.30	1.72	1.0		94.66	25.28	0.27	0.07
4024	-15	0.30	2.14	1.25	FW	-134.21	29.47	-0.25	0.05
4024	+15	0.30	2.14	1.25		106.50	26.50	0.20	0.05
4025	-20	0.30	2.14	1.25	FW	-171.98	48.32	-0.32	0.09
4025	+20	0.30	2.14	1.25		103.54	26.115	0.19	0.05
4026	-17.5	0.30	0.5	0.86	PV	-34.94	9.19	-1.19	0.31
4026	+17.5	0.30	0.5	0.86		38.11	12.26	1.29	0.42
4029	-17.5	0.30	1.29	0.75	FW	-82.00	22.96	-0.42	0.11
4029	+17.5	0.30	1.29	0.75		88.89	29.93	0.45	0.15
4030	+22.5	0.30	1.29	0.75	PV	-102.23	38.03	-0.52	0.19
4030	-22.5	0.30	1.29	0.75		109.74	46.74	0.56	0.24
4031	+22.5	0.30	1.72	1.0	PV	-144.60	48.45	-0.42	0.14
4031	-22.5	0.30	1.72	1.0		128.95	41.17	0.37	0.12
4032	-22.5	0.30	1.72	1.0	FW	-141.53	45.86	-0.41	0.13
4032	+22.5	0.30	1.72	1.0		127.96	40.88	0.37	0.12
4034	-20	0.25	1.17	0.75	PV	-60.61	22.43	-0.38	0.14
4034	+20	0.25	1.17	0.75		64.90	25.87	0.40	0.16
4034	-22.5	0.25	1.17	0.75	PV	-67.17	25.26	-0.42	0.16
4034	+22.5	0.25	1.17	0.75		72.81	31.97	0.45	0.20
4035	-20	0.25	1.57	1.0	FW	-95.32	32.28	-0.33	0.11
4035	+20	0.25	1.57	1.0		103.47	41.96	0.35	0.14
4035	-22.5	0.25	1.57	1.0	FW	-106.66	64.25	-0.37	0.22
4035	+22.5	0.25	1.57	1.0		113.56	49.99	0.39	0.17

Appendix B

Calculations from project thesis

Table B.1: Lift force on the foil at different angles of attack, α and increasing velocity, using linear foil theory. All values marked in red exceeds the maximum limitations set by the rig.

Lift force F_y [N]								
α **[deg]**		1	5	10	15	20	25	30
Fnh	V [m/s]							
0.045	0.1	0.05	0.23	0.45	0.66	0.86	1.04	1.19
0.090	0.2	0.18	0.91	1.80	2.65	3.43	4.14	4.75
0.181	0.4	0.73	3.64	7.20	10.60	13.74	16.56	19.00
0.271	0.6	1.64	8.19	16.20	23.83	30.91	37.27	42.74
0.361	0.8	2.92	14.57	28.80	42.37	54.95	66.25	75.98
0.452	1.0	4.57	22.76	45.00	66.20	85.87	103.53	118.71
0.542	1.2	6.58	32.77	64.80	95.33	123.66	149.08	170.95
0.632	1.4	8.95	44.61	88.20	129.75	168.31	202.92	232.68
0.722	1.6	11.70	58.26	115.20	169.48	219.84	265.03	310.02
0.813	1.8	14.80	73.74	145.79	214.50	278.23	335.43	384.63
0.903	2.0	18.27	91.04	180.00	264.81	343.49	414.11	474.85

Table B.2: Weber number. All values marked in red are below the limit for neglible surface tensions set by Webers number.

Fn_h	U [m/s]	We [-]
0.045	0.1	69
0.090	0.2	274
0.226	0.5	1717
0.361	0.8	4396
0.452	1.0	6868
0.587	1.3	11607
0.722	1.6	17582
0.903	2.0	27473

Table B.3: Bow wave breaking criteria ($\alpha_E \geq 25°$) and critical Froude number to generate an overturning bow wave

		Foil 1	**Foil 2**	**Unit**
Waterline entrance angle	α_E	45	15	[deg]
Critical Froude number	$Fn_{h_{crit}}$	0.89	-	[-]

Appendix C

Area of ventilated flows

Table C.1: The ventilated area for run 2190

Run 2190 - Step - wise ventilation -17.5 degrees, V_max = 1.25m/s, $Fn_{h,max}$ = 0.582				
Time [sec]	Fn_h	Velocity [m/s]	Nr. ventilated squares	Ventilated area [cm^2]
70	0.368	0.79	2.75	68.75
75	0.466	1	1.75	43.75
80	0.466	1	2	50
85	0.466	1	1.5	37.5
90	0.582	1.25	3.75	93.75
95	0.582	1.25	5.75	143.75
100	0.582	1.25	6	150
105	0.466	1	1.875	46.875
110	0.466	1	2	50
115	0.466	1	0.5	12.5
120	0.349	0.75	0.25	6.25

Table C.2: The ventilated area for run 4013

Run 4013 - Quasi-steady state -17.5 degrees, a =0.3m/s^2				
Time [sec]	Fn_h	Velocity [m/s]	Nr. ventilated squares	Ventilated area [cm^2]
9	>0.05	>0.1	1.88	46.875
14	0.391	0.84	22.5	562.5
19	0.931	2.0	25	625
24	0.931	2.0	22.625	565.625
29	0.931	2.0	24.75	618.75
34	0.931	2.0	22.375	559.375
39	0.931	2.0	25.5	637.5
44	0.931	2.0	26	650
49	0.931	2.0	22.375	559.375
54	0.931	2.0	20.125	503.125
59	0.931	2.0	22	550
63	0.927	1.99	0.375	9.375

Table C.3: The ventilated area for run 3006

Run 3006 - Quasi-steady state -17.5 degrees, a =$0.046m/s^2$				
Time [sec]	Fn_h	Velocity [m/s]	Nr. ventilated squares	Ventilated area [cm^2]
30	0.401	0.86	2.125	53.125
35	0.512	1.10	3.125	78.125
40	0.605	1.30	6.250	156.25
45	0.722	1.55	18.75	468.75
50	0.829	1.78	21.375	534.375
55	0.931	2	21.375	525
60	0.931	2	21	525
65	0.908	1.95	15.125	378.125
70	0.792	1.7	9.25	231.25
75	0.699	1.5	5.625	140.625
80	0.587	1.26	2.375	59.375
85	0.466	1.0	1.25	32.25
90	0.373	0.8	0.5	12.5

Table C.4: The ventilated area for run 4019

Run 4019 - Dynamic angles α = $-20°$ V_{max} = $0.86m/s$, Fn_{h_max} = 0.5				
Time [sec]	Fn_h	Velocity [m/s]	Nr. ventilated squares	Ventilated area [cm^2]
65	0.5	0.86	1.125	28.125
70	0.5	0.86	1	25
74	0.5	0.86	1	15.625
94	0.5	0.86	1.875	46.875
99	0.5	0.86	1	25
104	0.5	0.86	0.75	18.75

Table C.5: The ventilated area for run 4020

Run - Dynamic angles α = $-20°$ V_{max} = $0.75m/s$, Fn_{h_max} = 0.75				
Time [sec]	Fn_h	Velocity [m/s]	Nr. ventilated squares	Ventilated area [cm^2]
55	0.75	1.29	4.25	106.25
60	0.75	1.29	3.5	87.5
65	0.75	1.29	4.5	112.5

Table C.6: The ventilated area for run 4022

Run - Dynamic angles α = $-20°$ V_{max} = $1.72m/s$, Fn_{h_max} = 1.0				
Time [sec]	Fn_h	Velocity [m/s]	Nr. ventilated squares	Ventilated area [cm^2]
71	1.0	1.72	2.25	56.25

Elisa Solheim Høstmark

Experimental and numerical investigations on wave profiles and ventilation on a surface-piercing hydrofoil

NTNU
Kunnskap for en bedre verden